ON THE FORMATION OF CZTS (Cu_2ZnSnS_4) BASED FILMS FOR PHOTOVOLTAIC APPLICATIONS

YIN XUESONG

(M. E., Univ. of Electron. Sci. and Tech. of China)

A THESIS SUBMITTED

FOR THE DEGREE OF DOCTOR OF PHILOSOPHY

DEPARTMENT OF MATERIALS SCIENCE AND ENGINEERING

NATIONAL UNIVERSITY OF SINGAPORE

2014

Declaration

I hereby declare that the thesis is my original work and it has been written by me in its entirety.

I have duly acknowledged all the sources of information which have been used in the thesis.

This thesis has also not been submitted for any degree in any university previously.

YIN XUESONG
10 Aug 2014

Acknowledgements

First of all, I would like to express my sincerest gratitude to my supervisor, Professor Gong Hao, for his conscientious guidance during past four years. Academically, I have deeply inspired by his great passion, insistent dedication and insightful view in scientific research. More importantly, his responsibility, kindness and integrity have tremendous influences on my living philosophy and will benefit my whole life.

My great appreciations go to our group members and colleagues, Dr. Wang Yu, Dr. Yang Weifeng, Dr. You Guofeng, Dr. Tang Zhe, Dr. Zhang He, Dr. Sun Jian, Dr. Tang Chunhua, Mr. Huang Yanhua, Ms. Wee Ruiqi, Ms. Zhang Liuyang, Mr. Huang Tang Jiao, Mr. Chen Maohua, Mr. Zuo Lianyong and Mr. Sun Yang for their enlightening discussions and cherish friendships. In addition, I am willing to thank all the staff members in the department of materials science and engineering for their kind assistants and suggestions in my research.

I also wish to acknowledge Dr. Yu Zhigen from Institute of High Performance Computing, Dr. Li Chunxiang from Singapore Polytechnic, Ms. Shen Lu from Institute of Materials Research and Engineering, Dr. Chen Rui and Mr. Sun Linfeng form Nanyang University of Technology for their invaluable help in my research during these four years.

Last but not least, I am very grateful to my families. My grandparents and parents give me their unconditional understanding and support all the time. And my dear wife, Xie Shanshan, always keeps me accompanied with her loving care.

Table of Contents

Summary

Cu_2ZnSnS_4 (CZTS) based films have attracted increasing attention as a sunlight absorber for photovoltaic applications, because of their comparable properties with the successful $Cu(In,Ga)Se_2$ (CIGS). Furthermore, their advantage in the cost of raw materials makes them more promising when a large scale production is anticipated. Although significant progresses have been achieved in the CZTS based solar cells, there is still a big margin to catch up with their CIGS counterparts. And the phase instability issues have been demonstrated to be a severe problem that degrades the device performances. However, the comprehensive studies on these problems are yet to be well established. To obtain a deeper understanding on the mechanisms of the phase instability and prepare device quality CZTS based films, systematic experimental studies and theoretical analysis on the phase decomposition and secondary phase segregation as well as the impacts of precursor adjustments on CZTS based films formation were conducted in this thesis. In addition, efforts were also made to fabricate a CZTSSe based solar cell device.

CZTS decomposition problems were studied through carefully designed temperature dependent annealing experiments. In addition to the expected Sn loss phenomena, more theoretical insights into the Sn loss and various phase changes were revealed. By applying kinetic analysis, an equimolar-isobaric mode transition was demonstrated during the process of Sn loss. In order to

avoid the Sn loss and keep CZTS stable, a relatively high annealing pressure is required, since a correspondingly high temperature (>500 ℃) is needed to activate effective grain growth. Therefore, a two-step growth strategy for CZTS based films can be proposed, which includes a low temperature precursor deposition and a high pressure post-annealing.

By applying this film deposition strategy, the Sn loss problem was successfully overcome. However, the secondary impurity phase segregation problems arise when annealing precursors with various compositions. A temperature dependent annealing and thermodynamic analysis were applied to study related reactions, which presented convincing explanations on the film formation mechanisms. To achieve a secondary-phase-free CZTS based film, near-stoichiometric metal contents and an annealing temperature above 500 ℃ were normally required.

In addition to the metals' influences, the impacts of sulfur in precursor were also explored. Comparative studies were conducted on the CZTSe and CZTSSe films prepared by selenization of co-evaporated metallic and sulfur-contained precursors. Intense metal atom migrations, formation of big binary grains and thick $MoSe_2$ interfacial layers were observed in the CZTSe case. However, the incorporation of sulfur was found to suppress the metal migrations and the growth of $Mo(SSe)_2$ layer. Therefore, the sulfur incorporated sample possessed a much better film adhesion and comparable elastic modulus values to the theoretical simulation.

A CZTSSe based solar cell device with a power conversion efficiency of 5.2% was successfully fabricated. While its small open-circuit voltage and large series resistance were attributed to the relatively low efficiency, a better understanding on the properties of the CZTSSe layer and its contact interfaces are expected to improve the device performance in the future.

List of Tables

List of Figures

Chapter 1 Introduction

1.1 Research background of Cu_2ZnSnS_4

Energy and related environmental problems have attracted much attention of the international community in the past decades and will still stay as one of the top issues in the foreseeable future. Worldwide energy consumptions in last century and next decades are estimated and summarized in Figure 1.1. [1]

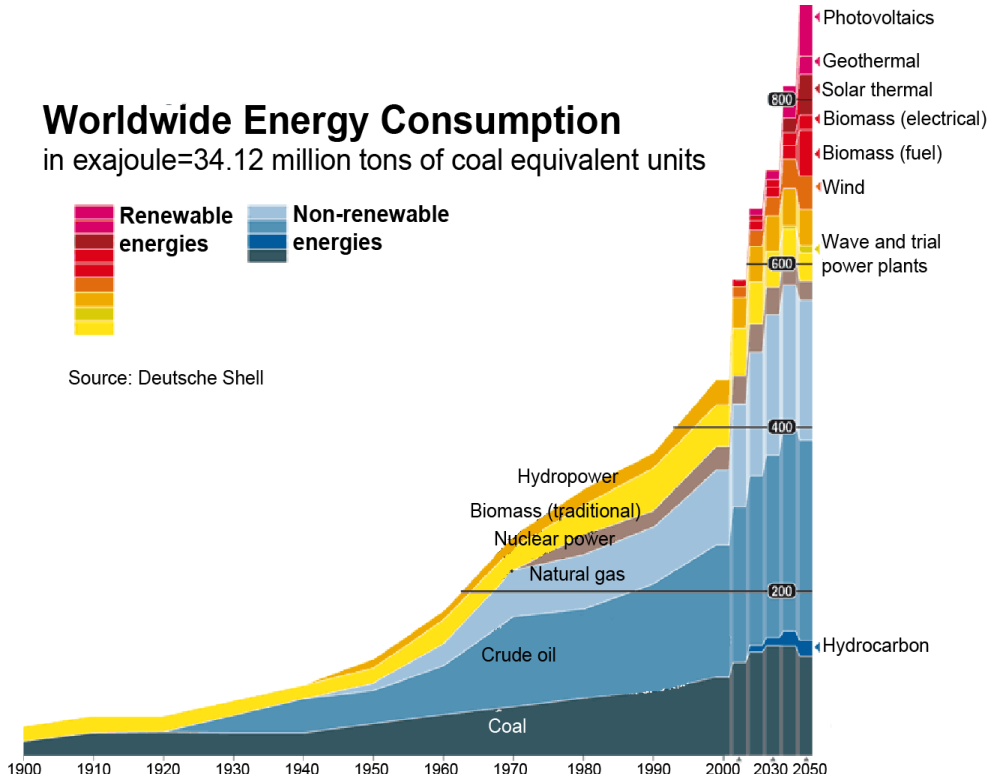

Figure 1.1 Worldwide energy consumption (Adapted from [1]).

The traditional fossil fuels, such as coal, oil, natural gas and so on, took the most part in the past and there will still be an increasing demand on these fuels. However, due to the limited resource of fossil fuels and the environmental

crisis, renewable and green energies are required to participate into the energy supply. Renewable energy provides 9% of total electricity generation worldwide. Among them, solar energy accounts for 0.1% (2011) and 0.25% (2012) in total USA energy consumption. The global photovoltaic (PV) market reached 31GW total in 2012 compared to 170 MW in 2000. While the absolute number is still small among other renewable sources, solar PV market shows a more significant increase. Nowadays, although many practical applications of solar cells have been realized and a new industry is emerging, it is still far away to fill up the daily electricity supply, because of its higher effective energy cost compared with the traditional energies.

Thin film solar cell will consume less raw materials due to its reduced thickness and various materials and technologies can be adopted to fabricate this type of solar cell, thus it is considered as the second generation of solar cells. According to the absorber materials, thin film solar cells can be mainly categorized into Si, CdTe and $Cu(In,Ga)Se_2$ (CIGS) based devices. The power conversion efficiency of a solar cell is a critical parameter that is normally used to evaluate the cell performance, and the best laboratory solar cell efficiencies obtained by different technologies are plotted in Figure 1.2. [2] It can be seen that the Si based thin film solar cell has the highest efficiency of 13.4% using amorphous Si absorber reported by LG Electronics. The highest efficiency obtained in CdTe thin film solar cell is 21% from First Solar. The CIGS based cells can achieve an efficiency of 21.7%, which is also the highest

among these thin film solar cells.

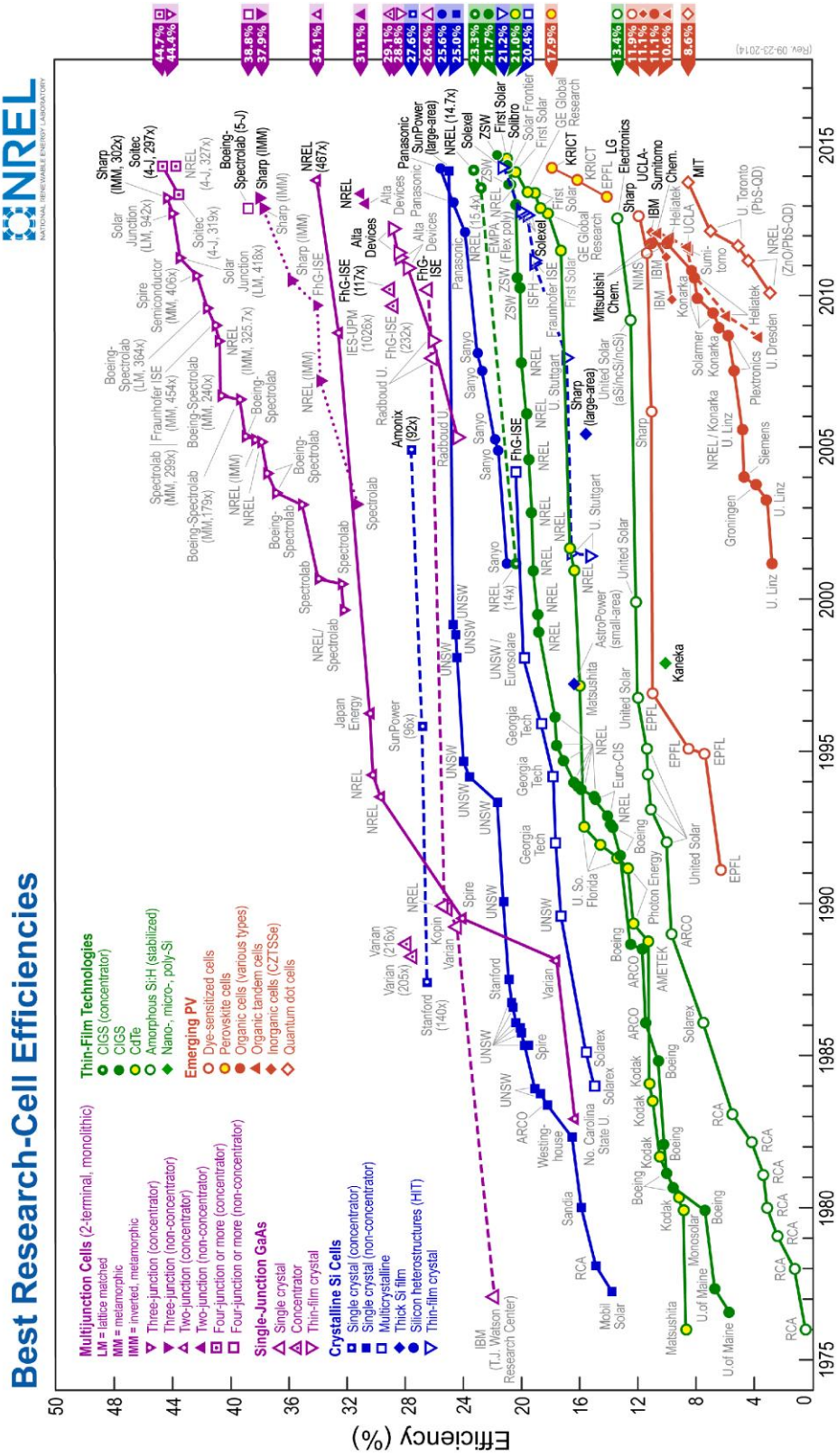

Figure 1.2 Best laboratory solar cell efficiencies. Data compiled by National Renewable Energy Laboratory (NREL) (Adapted from [2]).

However, challenges still exist in these devices. For example, the amorphous Si based devices have severe instability problems that degrade the device performances. The toxic components in CdTe based devices highly increase their safety and waste treatment costs. And the expensive elements, like In and Ga, in CIGS block its mass production in the future. Therefore, it is highly required to explore other candidates involving low cost materials to serve as solar cell absorbers.

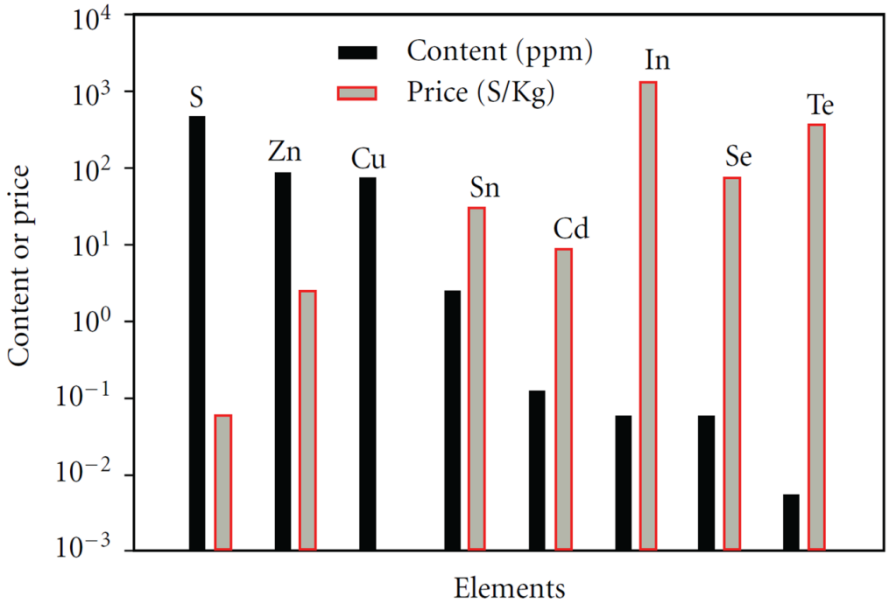

Figure 1.3 The earth crust content and the price of the elements used in CdTe, $CuInSe_2$ (CIS) and CZTS based thin film solar cells (Adapted from [3]).

The earth crust content and the trading price of the elements used in CIS and CdTe as well as CZTS light absorbers are illustrated in Figure 1.3. The abundance of Zn and Sn in earth's crust is found 1500 times and 45 times greater than that of In. And the price of In is almost two orders of magnitude higher than that of Zn and Sn. [3] If also considering the cost of toxic

controlling for Cd used in CdTe based solar cell, CZTS based materials are of great advantage in raw materials' cost. Moreover, CZTS also shares comparable physical properties with the successful CIGS system, which makes it reasonably possible to be considered as a good candidate to compete with CIGS. In fact, the development of CZTS can also be found in Figure 1.2 as one emerging PVs in recent years. Although its efficiency (~10%) is still far below CIGS, this material deserves more attention and study, when considering its short development duration and promising properties.

1.2 Basic properties of CZTS

1.2.1 Crystal structure of CZTS

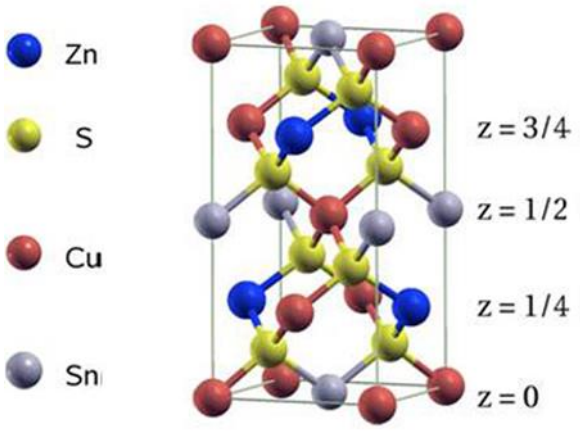

Figure 1.4 Schematic representation of the kesterite CZTS (Adapted from [4]).

Cu_2ZnSnS_4 is generally crystallized in the kesterite structure as shown in Figure 1.4. From both experimental and theoretical aspects, the kesterite structure is found the most stable phase for CZTS, which exhibits the lowest

formation energy. A tetragonal cell with a=5.427Å and c=10.871Å (PDF #26-0575) can be indexed to the kesterite CZTS. [4, 5] Its selenide counterpart, $Cu_2ZnSnSe_4$ (CZTSe), belongs to the same crystal group with lattice constants, a=5.693 Å and c=11.333 Å (PDF #52-0868). The lattice parameter values of a hybrid $Cu_2ZnSn(S_{1-x}Se_x)_4$ (CZTSSe) system is calculated and shown in Figure 1.5. [6] The CZTSSe phase is often employed to fabricate devices as well, due to its tunable properties.

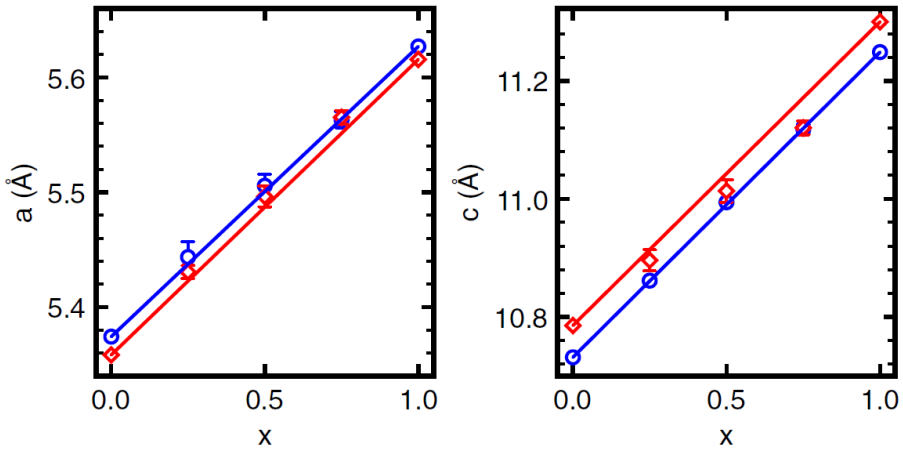

Figure 1.5 Lattice parameters a and c of $Cu_2ZnSn(S_{1-x}Se_x)_4$ as a function of Se fraction x (Adapted from [6]).

1.2.2 Electrical properties of CZTS

The resistivity of CZTSSe thin films was found to vary in a large range from $7.0\times10^{-3}\Omega$cm to $1.4\times10^{4}\Omega$cm and depend on Cu component and Se/S ratio.[7-9] Although experimental studies on the defects in CZTSSe were reported by frequency dependent electrical measurements and TEM

characterization, [10-12] the defect physics are mainly studied by simulations.[4, 13, 14] According to the calculated results in Figure 1.6, Cu_{Zn} antisite and Cu vacancy (V_{Cu}) have relatively low formation energies among all the possible intrinsic defects. Meanwhile, the transition-energy level position of Cu vacancy is calculated to be 0.02eV above the valance band maximum (VBM), which exhibits the shallowest accepter level among the low energy intrinsic defects. Therefore, the CZTSSe film has a p-type semiconductor's behavior and its resistivity is sensitive to Cu content. In practice, Cu poor conditions also give rise to better device performances. [15, 16]

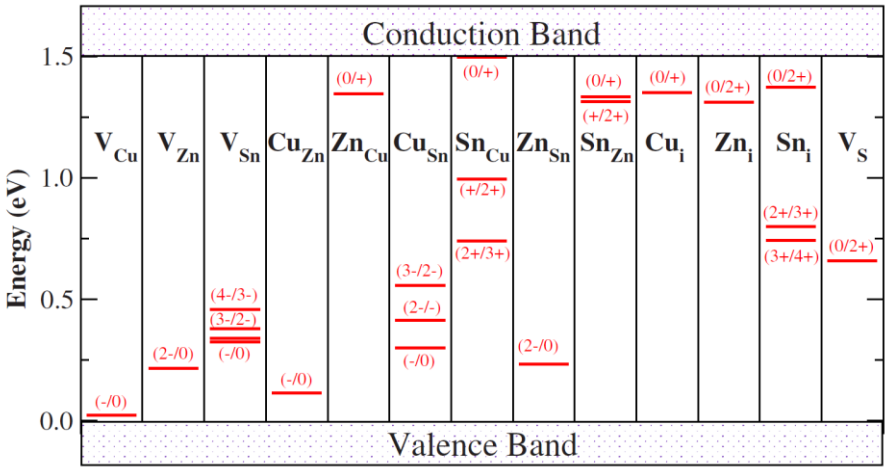

Figure 1.6 The transition-energy levels of intrinsic defects in the band gap of Cu_2ZnSnS_4 (Adapted from [13]).

In order to study the transport mechanisms in CZTSSe based films, temperature dependent resistivity measurements were carried out. [17-19] It was found that several mechanisms, including Mott variable-range hopping

(VRH), Efros–Shklovskii VRH, nearest-neighbor hopping and thermionic emission over grain boundary, may contribute to the carrier transport process.

1.2.3 Optical properties of CZTS

Cu_2ZnSnS_4 thin film has a direct band gap around 1.5eV and a high optical absorption coefficient above $10^4 cm^{-1}$ in the visible light region.[8, 20-22] In addition, it's established that the hybrid CZTSSe system exhibits a great flexibility to tune the band-gaps (1.0~1.5eV) by adjusting the ratio of sulfur over selenium. [23-25] A calculated band structure of kesterite CZTSSe and band gap variation with respect to Se/S compositions are presented in Figure 1.7. [4, 24] Experimental results were also reported, which agreed with the theoretical predictions quite well. [23, 26, 27]

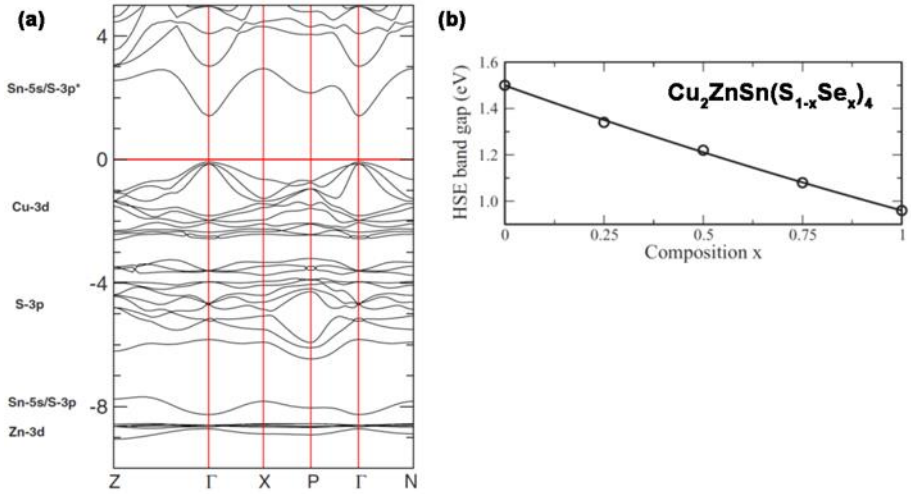

Figure 1.7 (a) The calculated band structure of kesterite CZTS and (b) the calculated band gap of $Cu_2ZnSn(S_{1-x}Se_x)_4$ at different composition Se/S compositions using Heyd-Scuseria-Ernzerhof (HSE) model (Adapted from [4, 24]).

1.3 CZTS based solar cells

1.3.1 Device structure of CZTS based solar cell

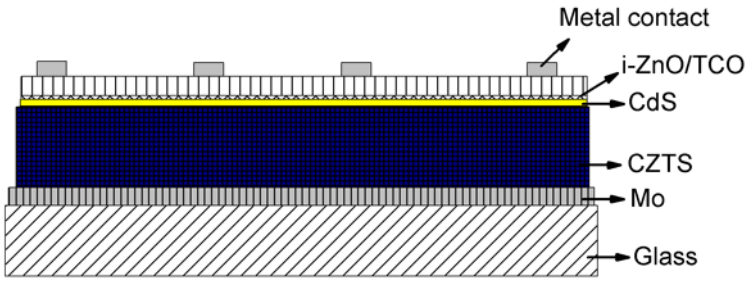

Figure 1.8 Sketch of a CZTS solar cell device structure.

Because of the similarity of CZTS and CIGS, so far, the CZTS based solar cells mainly follow the device structure of the CIGS solar cells as shown in Figure 1.8. Normally, a molybdenum (Mo) metal layer is deposited on glass substrate as the back contact. A 1~2μm thick CZTS film is then prepared as the p-type light absorber on the Mo layer. After that, a thin CdS layer with a thickness around 50nm is grown on the CZTS layer by chemical bath deposition. Then, an intrinsic ZnO buffer layer and a transparent conducting oxide are deposited on top by sputtering. Finally, patterned front metal contacts are made to complete the device. An anti-reflection layer (MgF2) can also be deposited to further improve the performance. Therefore, the CZTS and CIGS cell is just constructed as a typical p-n junction film solar cell structure. [15, 28]

1.3.2 CZTS fabrication and device performance

Two major fabrication strategies are applied to obtain a CZTS layer. One is to synthesize CZTS particles first and then transfer these particles to a substrate and form the CZTS layer through post-annealing. CZTS particles can be synthesized by many methods. Riha *et al.*, [29] Guo *et al.* [15, 22] and Haas *et al.* [30] prepared CZTS based nano-crystals by a hot injection method. Zhou *et al.* [31], Zaberca *et al.* [32] and Xu *et al.* [33] reported CZTS particle synthesis through a solvothermal method. Mechanical ball milling was used to get CZTS particles by Wibowo *et al.* [34] and Wang *et al.* [35]. Besides, other solid-state reaction method was also developed to produce CZTS powders. [36, 37] After the particle synthesis, ink precursors are generally prepared to transfer the materials to form a film. There are several technologies, such as spin coating, [38, 39] doctor blade, [15, 22] printing [40] and spray coating, [41] were reported to fulfill the purpose.

The other fabrication strategy is a direct growth of CZTS film on the substrate. Within this category, two types of methods are utilized, one is solution based and the other is vacuum based. Todorov *et al.* [25] developed a hydrazine solution route to achieve high quality CZTS based films. Besides, CZTS precursor films were also prepared from chemical solutions through electrochemical deposition, [42, 43] chemical bath deposition [44] and spray pyrolysis [45, 46]. For the vacuum based technologies, thermal evaporation, sputtering, pulsed laser deposition and chemical vapor deposition were all

applied to deposit precursor films for CZTS based solar cell application. Principally, a post-annealing or sulfurization step is always required to generate a dense CZTS layer with big grains, no matter what kind of method is used to prepare the precursor films.

Currently, the CZTS based solar cell device is still at the lab research stage. So far, the highest efficiency (12.6%) is achieved by the hydrazine solution method.[47] Besides, the ink coating with nanoparticles prepared by hot injection also achieved efficiency values around 9%. [48, 49] Over 8% efficient cells were obtained through the co-evaporation technology. [50, 51] By using electrochemical deposited alloy precursors, CZTS based devices with efficiency values around 7% were also reported.[28, 52] Even though an increasing trend of the efficiency values for the CZTS based devices can be reviewed during recent years, it is still unsatisfactory for practical application. And there is a big improvement margin to its theoretical efficiency limit (>30%). To understand the problems that limit the performance of CZTS based solar cells, a deep study on the material itself becomes quite necessary.

1.4 Problem statement and Motivation

Serious phase instability problems in a CZTS system, like Sn loss and secondary phase segregation, arise when employing vacuum deposition and high temperature annealing treatment. To achieve high quality CZTS based

films for photovoltaic applications, efforts are required to study the phase formation and segregation mechanisms during film growth.

1.4.1 Phase decomposition issue in CZTS

Because of the similarity of CZTS and CIGS, it becomes very effective to imitate the successful case of CIGS when we study CZTS based solar cells. From the very basis, the major difference between CZTS and CIGS in composition is two metal elements, i.e. Zn and Sn. Unfortunately, this difference causes serious stability problems in CZTS that didn't occur in the CIGS system. In experiments, both Zn and Sn were found easy to get lost during CZTS film deposition or post-annealing, especially in a vacuum based procedure. The observation of Zn loss was reported in a vacuum deposition or sulfurization with a relatively high temperature. [53] Severe Sn loss generally happened when depositing or annealing S or Se contained precursors. [54-56] For those Zn or Sn loss during film deposition at a high substrate temperature can be avoided by lowering temperature. However, the post-annealing is an essential step to accomplish the big grain growth and bulk film formation for the photovoltaic devices, requiring a high temperature that may result in a decomposition of CZTS. This certainly turns to be the first challenge before we can make a CZTS based solar cell device.

In literatures, a single-step decomposition reaction model was proposed to interpret the vaporization of SnS phase. [55] Later, a two-step decomposition

model was established which emphasized the solid-vapor transition of SnS where the instability of Sn^{4+} was claimed to be the driving force for the decomposition.[56] In both reaction models, Sn was the only active metal being considered and its valance alternation was assumed to be totally compensated by the corresponding valence change of sulfur. It should be noted that Cu has also multiple oxidation states, i.e. Cu^{1+} and Cu^{2+}, which should allow it to participate in the oxidizing and reducing reactions. In practice, binary copper sulfide phases (other than Cu^{1+}) were already found in some near stoichiometric Cu-contained absorbers including CZTS. [57-59] In addition, effective thermoelectric effects have been found in CZTS based materials. [60-62] Thus, a non-uniform carrier (hole in CZTS) distribution, i.e. non-uniform oxidative environment, can possibly exist under a directional heat field. Like many Cu-contained p-type materials, the dominant acceptors in CZTS are intrinsic Cu defects (Cu vacancy and Cu_{Zn} antisite) due to their small formation energies and shallow state levels to the valance band. [13, 63] Furthermore, Cu vacancies have a tendency to transfer and coalesce to large voids under a bias potential, such as an electrical field or an oxidative environment. [64-66] As a result, a directional heat field may introduce some unbalanced potentials to drive Cu vacancies or Cu ions to move and redistribute along the field direction, and it is desirable to study whether such an effect exists. After all, a careful study on the mechanism

s of phase decomposition in CZTS becomes very necessary to reveal the chemical origins for the instability issue.

1.4.2 Secondary phase segregation issues in CZTS

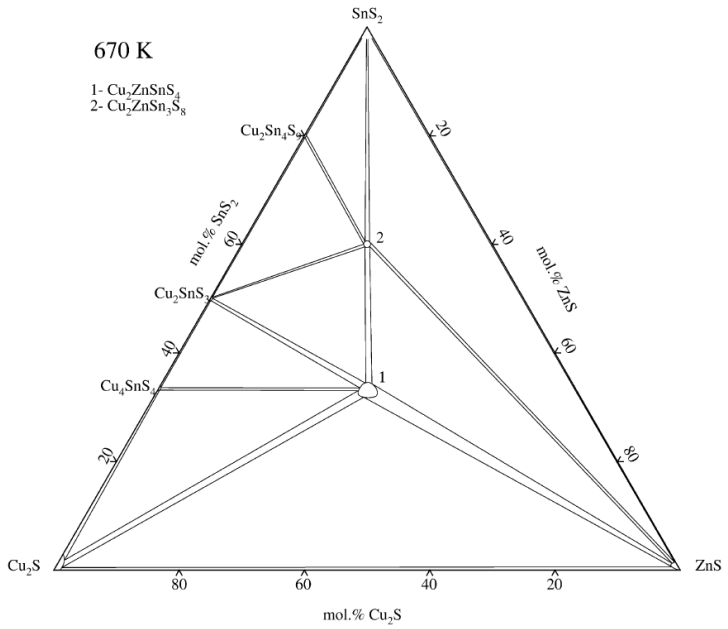

Figure 1.9 Isothermal section of the Cu_2S-SnS_2-ZnS system at 670K (Adapted from [67]).

In addition to the phase decomposition of CZTS at a high temperature, there is the other aspect of the phase instability issues, which is the secondary phase segregation during CZTS film formation. Theoretical simulations on the phase formation of CZTS revealed that small potential regions are available for this material to stay as a stable phase.[13, 14, 63] A phase diagram of CZTS at 670K was also reported as shown in Figure 1.9. [67] A very small area for

CZTS can be found in the diagram, which indicates a precise composition control is required to obtain a stable CZTS phase. Without surprise, the secondary phases are easily observed during CZTS film deposition in literatures. [57, 68-72] Meanwhile, these secondary phases are believed to have negative influences on the performance of a photovoltaic device. Thus, to avoid these secondary phase formation or eliminate them after the film growth becomes an essential requirement.

To deal with the secondary phase formation issues of CZTS(e), we need to consider at least three metal cations and one of S^{2-} and Se^{2-} anions together with binary and ternary phases being involved, which makes the analysis quite complicated. Scragg *et al.* [56, 64] studied the phase formation of CZTS films and its thermal stability. Yoo *et al.* investigated the formation reactions of CZTSe films from an intermetallic precursor. Fairbrother *et al.* [73] carried out a detailed work on the formation of Zn-rich CZTS films. As a result, some chemical insights and detailed formation processes have been obtained about the quaternary CZTS(e) systems. Moreover, the non-stoichiometric precursor composition was found to cause secondary phase precipitation. At the same time, post annealing conditions also have important influences on the phase formation. However, behind all these phenomena, there lacks a deep understanding on the reaction mechanisms, such as the movements of different metal species, reasons for the detailed reaction sequences, locations of the secondary phases and so on. Particularly, the location of the unfavorable

phases is far from understanding and worth more research, because an understanding of it can make the removal of such phases possible by methods such as chemical etching etc. [59, 74-77] The insights of such phenomena are essential for the improvement of film deposition procedures and the reduction of untreatable secondary phase segregation. Furthermore, because the S-Se coupled CZTSSe system with tunable bandgaps is more suitable for photovoltaic device fabrication than either CZTS or CZTSe, it will be of more practical value to study the secondary phase issue in CZTSSe films, although the secondary phase problem mainly concerns about the metallic elemental compositions regardless of the formation of sulfides in CZTS or selenides in CZTSe.

1.4.3 Impacts of sulfur-incorporated precursors on the CZTS based films

Sulfur incorporation into the precursor was reported to influence CZTSSe film growth during post-annealing. [9, 78] However, to the best of our knowledge, there is no report on the study of sulfur incorporated CZTS precursors to suppress the formation of $Mo(S,Se)_2$ layer and the improvement of the CZTS film adhesion and mechanical properties. It would be quite necessary and interesting to investigate the impacts of sulfur incorporation in CZTS precursors on the mechanical properties and adhesion performances of

CZTSSe films.

As a candidate for the light absorber in a thin film solar cell, in spite of the widely studied film growth, electronic and optical properties, [17, 73, 79, 80] the mechanical properties such as film adhesion, elastic modulus and hardness are also of great importance to a CZTSSe film system, but which are nevertheless rarely reported. Although the elastic modulus of a CZTSSe system has been calculated theoretically, [76, 81] an experimental measurement is unfortunately lacking. Besides, few quantitative studies on the adhesion performance of CZTSSe films can be found in literature.

In another aspect, the formation of a $Mo(S,Se)_2$ layer between the CZTSSe film and the conventional Mo substrate during post sulfurization or selenization were believed to degrade device performance. [16, 82, 83] Due to its lubricant nature, this layer should also affect the film adhesion. Even though several foreign buffers were introduced to reduce $Mo(S,Se)_2$ layers,[51, 84, 85] it is, if possible, more practically valuable and economic to suppress the $Mo(S,Se)_2$ layer through proper precursor employment in device fabrication.

1.5 Objectives and Outline of this thesis

The main objective of this work is to have a better understanding and control of the CZTS based film formation.

Referring to the problems stated above, the decomposition behavior and mechanisms of CZTS will firstly be studied. Then, a composition dependent film growth study will be conducted on a hybrid CZTSSe film on glass substrate to address the secondary phase formation issues. In this part, beside to obtain a secondary phase free CZTSSe film, the detailed reaction mechanisms will also be explored. Thirdly, CZTSSe films on Mo substrate will be studied to reveal possible influences of different sulfur contents in precursors on the interface formation. At last, some efforts will also be made to fabricate CZTS-based solar cell devices.

The whole thesis is consisted of 7 chapters. An introduction of the background and literature review is presented in Chapter 1. In Chapter 2, experimental methods to prepare CZTS based films and major characterization techniques used in this work are briefly described. Chapter 3 presents the study on the decomposition behavior and mechanisms of CZTS through a temperature dependent annealing and kinetic analysis route. A deeper understanding on the temperature-pressure related vaporization process in the CZTS decomposition is achieved, which is fundamental for the research work presented in other chapters. Chapter 4 studied the secondary phase formation in CZTSSe films grown on glass substrates by using precursors with different compositions. Temperature related selenization studies and thermodynamic analysis are conducted to reveal the phase formation details and chemical insights during film growth. Chapter 5 explores the effects of sulfur incorporation into

precursors on the film growth, interface formation and mechanical performances of CZTSSe films on Mo substrate. In Chapter 6, photovoltaic devices based on CZTSSe films prepared are fabricated, and a power conversion efficiency value of 5.2% is achieved. Finally, Chapter 7 summarizes major conclusions and proposes future works.

Chapter 2 Experimental methods

2.1 Introduction

In this chapter, two material preparation methods utilized in this thesis will be presented, which are chemical solution pyrolysis and thermal evaporation. Then, various material and device characterization techniques applied in this work will be introduced. Specific experimental details will be provided in later relevant chapters.

2.2 Material fabrication methods

2.2.1 Solution pyrolysis

Solution pyrolysis is a well-developed method to fabricate many kinds of sulfides materials, such as CuS, ZnS, SnS, Cu_2SnS_3 and so on. [86-89] It has great advantages of low cost, chemical flexibility and convenient composition control. In practice, aqueous solutions of metal salts and sulfur contained organic solutes are prepared as precursors. Then, thermal treatment is carried out to evaporate the solvent and generate concentrated products with metal-organic complex, which will decompose to the targeted materials and gaseous byproducts by further heating. A summarized chemical reaction in preparing CZTS through the pyrolysis method is written in equation (2-1), in

which metal chloride salts and thiourea, $SC(NH_2)_2$, are used as the metal and sulfur source, respectively. [45] In addition, a spray method can easily be developed based on the pyrolysis procedure to deposit thin film samples, including CZTS based films. [90, 91]

$$2CuCl + ZnCl_2 + SnCl_4 + 4SC(NH_2)_2 + 8H_2O \rightarrow Cu_2ZnSnS_4 + 8NH_4Cl + 4CO_2 \quad (2\text{-}1)$$

In this work, an aqueous solution with copper (I) chloride (CuCl, >97%), zinc (II) chloride ($ZnCl_2$, >98%), stannic chloride pentahydrate ($SnCl_4$ $5H_2O$, >98%) and thiourea ($SC(NH_2)_2$, >99%) was used to prepare CZTS with Cu:Zn:Sn =2:1:1. An excess amount of thiourea was required to prevent the precipitation of thiourea complexes of metal chlorides and compensate a possible sulfur loss in the thermal process. [45, 91] The transparent solution was slowly evaporated around 80˚C on a hot plate until the solution became a yellow gel. The gel was then transferred to a quartz boat and heated at 200˚C for 1 hour and then 300˚C for 8 hours in vacuum. Black CZTS powders were then obtained, grinded and pressed to round pellets for later decomposition studies discussed in Chapter 3.

2.2.2 Thermal evaporation and annealing

As mentioned in Chapter 1, many vacuum based technologies have been employed to prepare precursors for CZTS related films, in which thermal

evaporation is one well established method. A thermal evaporation system is introduced to prepare CZTS precursors in this work. After that, a sulfuriztion or selenization process is applied to finish formation of CZTS based films. Herein, the thermal evaporation system and annealing systems will be introduced below.

Firstly, let's go through the basic working principles of thermal evaporation. Two basic processes are involved in the thermal evaporation deposition. One is that the solid source material is heated up and transferred to a gaseous state. The other process is a re-solidification of the gaseous materials when they arrive at a substrate at relatively low temperatures. It is noted that evaporation takes place in vacuum, which provides a vacant ambiance for the evaporated particle to travel with a long mean free path. Therefore, the thermal vaporization process relies much on the environmental pressure and the nature of source materials. A saturated vapor pressure database has been generated according to experimentally measured relationship between the pressure and temperature for a given material. [92] The vapor pressure curve gives the minimum temperature needed to evaporate a material at a fixed vacuum. The evaporation rate can be adjusted by temperature control. Therefore, we need to find out the vapor pressure data of relevant elements involved in this work, including Cu, Sn, Zn, S and Se. In Figure 2.1, their vapor pressure curves are plotted according to reported reference. [93]

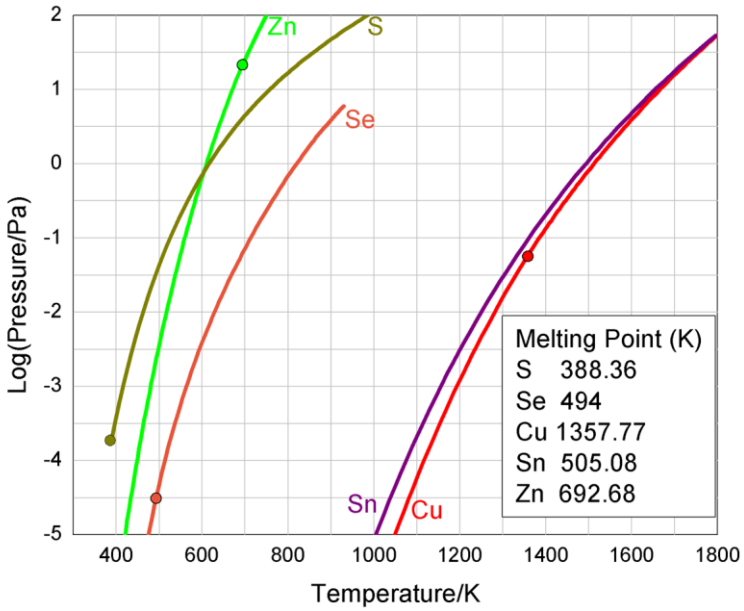

Figure 2.1 Saturated vapor pressure curves for Cu, Sn, Zn, S and Se, respectively (Adapted from [93]).

When the source material is vaporized, the gaseous matter with extra kinetic energy will travel in a vacuum chamber following the cosine distribution. For an ideal small source and planar receiving surface, the incident flux can be written as [94, 95]

$$J = \frac{z\delta A(\cos\theta)^4}{\pi h^2} \tag{2-2}$$

in which δA, h and θ represent the area of source, distance between source and substrate and incident angle. And z is the impingement rate expressed as [95]

$$z = \frac{P}{\sqrt{2\pi mkT}} \tag{2-3}$$

where P, m, T and k are the pressure, mass of particles, temperature and Boltzmann's constant, respectively. Thus, we can find that the evaporation rate is a temperature and pressure dependent parameter.

At last, the vapor arrives and condenses at a substrate. During this process, various energies exchanged between the gaseous material and substrate and transferred in re-solidification and crystal growth of condensed material also play an important role to the deposition rate. [95] In addition to the intrinsic properties of the source material and substrate, the temperature of substrate influences film formation quite a lot, especially in the case consists of several different species, like CZTS.

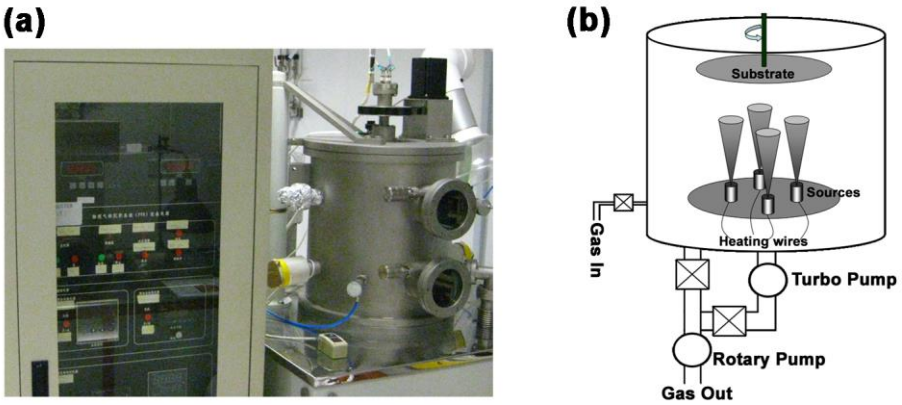

Figure 2.2 (a) The photo and (b) schematic diagram of the four-source thermal evaporation system applied in this work.

A thermal evaporation system is used in this work to fulfill precursor deposition for CZTS based films. The picture and schematic diagram of the system is shown in Figure 2.2. In Figure 2.2(b), four effusion sources are placed in the vacuum chamber, whose temperatures can be individually controlled by tuning their electrical power supply. The temperature can be elevated up to 1500 ℃ with an accuracy of 1 ℃. A substrate holder hangs on top of the sources, which is rotated with a speed of 3rpm during film

deposition. The substrate is not purposely heated in this work, since a high substrate temperature can cause re-evaporation of some volatile components in CZTS. The vacuum of the system can be pumped to 5×10^{-5}Pa within 8 hours. In the present study, this system can realize a co-evaporation of three or four source simultaneously. The substrates used in this work are commercial glass and Mo-coated glass. A standard substrate cleaning is always applied before deposition that employs ultrasonic bath wash in Micro 90 solution, acetone and ethanol for 15min in turn.

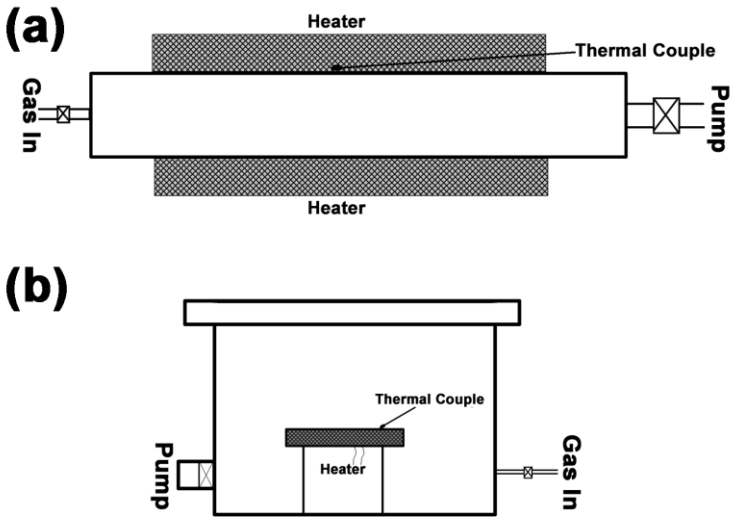

Figure 2.3 Schematic diagrams of the annealing systems used in this work: (a) tube furnace and (b) hot plate.

After the precursor deposition, a post annealing step is proceeded to allow further sulfurization or selenization to finish film growth incorporating sufficient sulfur or selenium content as the targeted CZTS based films needed. Besides, relatively large crystal grains preferred in a thin film solar cell device

are also achieved in this post-annealing. In addition to a high temperature, an inert environment is required during post-annealing, because oxidation should be avoided when generating a sulfide or selenide film. Thus, a pump system and an inert gas supply are also essential in the annealing equipment.

In this work, a tube furnace system with a turbo pump station and Ar gas supplying is utilized to anneal thin film samples. Its schematic diagram is shown in Figure 2.3(a). A high temperature above 1100 ℃ can be reached that is sufficient for the targeted temperature in this case (<700 ℃). In the experiments, the precursor samples and S/Se sources are placed into a carbon box with screw-tight cap, which is used as a secondary container in the quartz tube. The other annealing system with a plate heating element in Figure 2.3(b) is also applied to create a different heat field from the tube furnace. Equivalent pumping and gas supplying are equipped in this system, and it is used to study decomposition phenomena of CZTS in Chapter 3.

2.3 Material characterization methods

2.3.1 X-ray diffraction (XRD) and Raman spectroscopy

X-ray diffraction (XRD) is a widely used technology to determine crystal structures by indexing the diffracted intensity and angles of an X-ray beam interacted with a material to certain recorded standard patterns in the database. However, because of similar lattice parameters of certain secondary phases

(ZnS and Cu_2SnS_3) with CZTS, the information obtained from XRD will not be sufficient to distinguish the phases. Then, Raman spectroscopy is employed to help phase determination.

Raman spectroscopy is a commonly used spectroscopic technique to observe vibration or rotation modes in a material by working with a monochromatic light, usually from a laser source. The energy of the laser photons can be shifted through interactions with molecular excitations, such as vibrations, rotations and phonons, in the material system. The recorded Raman scattering intensity and shifts provide information about the vibrational modes in the tested material. By comparing measured Raman spectra with standard data from well crystallized samples or simulated results, phase identifications can be realized.

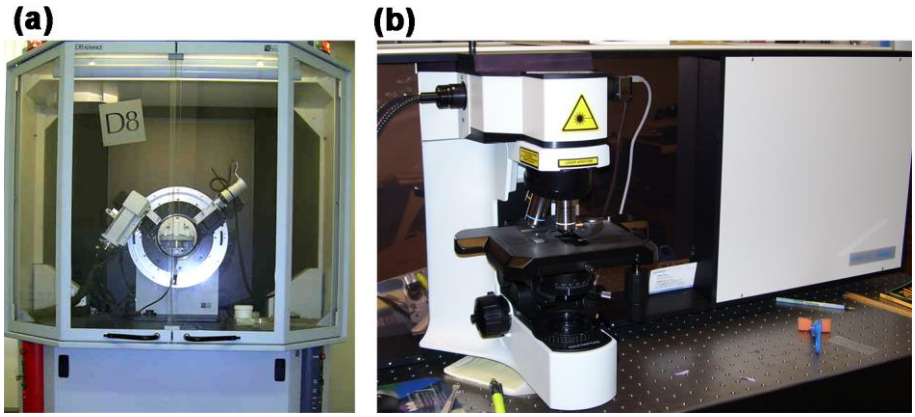

Figure 2.4 Pictures of (a) the XRD and (b) Raman systems used in this work.

In this work, a XRD system (BRUKER D8 ADVANCE) operated with CuK_α radiation (λ= 0.154060nm) at 40 mA and 40 kV is applied to collect the diffraction patterns. And the standard Powder Diffraction File (PDF) from

the International Centre for Diffraction Data (ICDD) is used to conduct the phase indexing. The Raman spectroscopy system (LabRam HR800) with a 532nm laser source is utilized to measure the Raman shift profiles. The XRD and Raman systems used in this work are presented in Figure 2.4. The powder sample is pressed to a pellet for XRD and Raman tests, and the thin film sample is characterized as prepared.

2.3.2 Scanning electron microscopy (SEM) and transmission electron microscopy (TEM)

Scanning electron microscopy (SEM) is one kind of electron microscope that can provide surface topography images of a sample. The sample surface interacts with accelerated electrons from an electron gun and sends out various signals that can be recorded by different detectors. Normally the signal from the secondary or backscattered electrons is detected to generate a magnified scanning image of electron intensities in the measured area. A field-emission cathode source generally provides a better image resolution than conventional SEM with thermally excited electron beam.

Transmission electron microscopy (TEM) is another kind of electron microscope that can provide images and electron diffraction patterns of a sample. In this technique, high energy electrons transmit through an ultra-thin specimen to get scattered or diffracted. The transmitted or diffracted electron

beams can be recorded to reveal micro-morphologies or crystal structures of the tested sample. An atomic scale resolution image can be achieved by TEM due to the small de Broglie wavelength of a high energy electron. Thus, a high-resolution TEM (HRTEM) image can provide lattice information, which makes it possible to visualize crystal phases or defects directly. In addition, selected-area electron diffraction patterns can also give information on crystal orientation and lattice spacing, serving as an alternative to XRD or Raman to analyze structural properties of a material, especially in a very small scale.

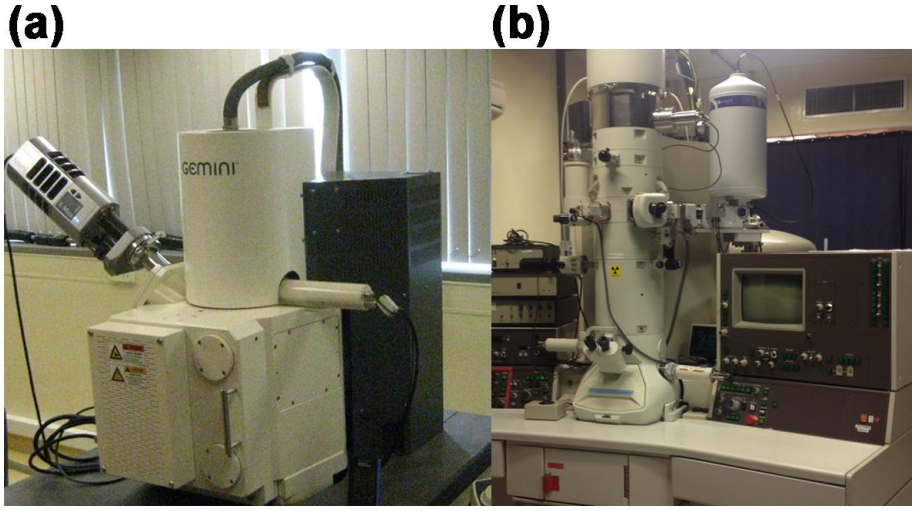

Figure 2.5 Pictures of (a) the SEM and (b) TEM systems used in this work.

In this work, an FE-SEM with multiple accelerating voltages and detectors (Zeiss Supra 40) is used to characterize the surface and cross-section morphologies. Normally the as prepared sample surface and fresh broken cross-section area are applied in the test without gold sputtering. An accelerating voltage of 5keV and alternative detectors, like secondary

electrons (SE), in-lens SE and back scattered electrons (BSE), are properly selected to collect the SEM images under an atmosphere pressure less than 5×10^{-5} mbar. A TEM system (JEOL 100CX 2010F) with accelerating voltage of 200 kV is utilized to capture TEM and HR-TEM images and diffraction patterns of the CZTS related samples. The pictures of the SEM and TEM systems used in this work are presented in Figure 2.5. For the powder sample, it is transferred to a copper grid sample holder by dropping ethanol solution that contains sample powder onto the holy carbon coated grid. For a thin film sample, a focused ion beam (FIB) method is performed to prepare cross-section TEM sample.

2.3.3 Energy dispersive X-ray spectroscopy (EDX), X-ray photoelectron spectroscopy (XPS) and Secondary ion mass spectrometry (SIMS)

Energy-dispersive X-ray spectroscopy (EDX) is a convenient analytical technique for elemental analysis. The fundamental principle of this technique relies on the specific atomic structure of each element, which can be demonstrated as characteristic X-ray spectra. Normally, an electron beam with elevated energies, i.e. accelerated by a relatively high voltage, interacts with a sample to stimulate characteristic X-rays emission. During this process, electrons in an inner shell are excited by the incident beam and get ejected out,

leaving electron vacancies. Then, electrons from a higher energy shell will fill the vacancy and release the extra energy as a form of X-ray. Unique allowing states of each element give rise to specific X-ray energies, which can be detected. In this way, the elemental information inside a specimen can be obtained. EDX accessories are often together with a SEM or TEM system, which allows elemental characterization in a selected area.

X-ray photoelectron spectroscopy (XPS) is another composition analysis technique, which not only gives elemental identifications but also reveals chemical or electronic states of the elements in the tested sample. Principally, a X-ray beam is used to irradiate at a sample, while the kinetic energy and number of electrons escaped from the surface are measured and recorded. The number of electrons detected is then plotted versus binding energy in a typical XPS spectrum. Each element can produce characteristic peaks at certain binding energies that allow direct identification of elements contained in the analyzed material. Besides, these characteristic peaks also demonstrate the details of electron configurations within an atom, e.g., 1s, 2s, 2p, 3s, etc. Furthermore, atomic percentage values inside the tested sample are able to be normalized and analyzed, because the number of detected electrons in each of the characteristic peaks is directly related to the amount of element within the XPS sampling volume. It should be noted that unlike the penetration depth of around 1 μm in EDX measurement, the characterized depth in XPS is only around 10nm, so XPS is a surface-sensitive technique.

Secondary ion mass spectrometry (SIMS) is a technique to analyze the composition of a specimen by sputtering the surface with a focused primary ion beam and collecting and analyzing ejected secondary ions. A time-of-flight (TOF) spectrometer is widely used to analyze the secondary ions, which separates the ions in a field-free drift path according to their velocity. It is able to detect all generated secondary ions simultaneously. SIMS is also the most sensitive surface analysis technique, with elemental detection limits ranging from parts per million to parts per billion. However, due to the large variation in ionization probabilities among different materials, SIMS is generally considered to be a qualitative technique.

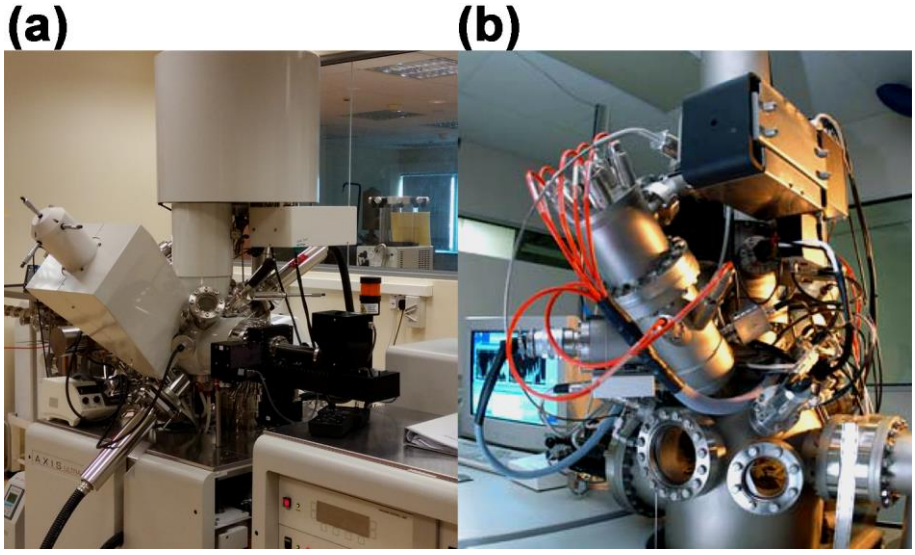

Figure 2.6 The Pictures of the (a) XPS system and (b) SIMS system used in this work.

In this work, an X-ray Energy dispersive spectroscopy (EDX, INCA, Oxford Instruments, Oxfordshire, UK) is used to determine elemental composition. An

accelerating voltage of 15keV is chosen to run the EDX measurement, making sure all the relevant elements inside the sample can be excited. Except for elemental analysis on selected spots or areas, elemental distributions over certain space can also be achieved by a combined elemental mapping function in the same machine. Both top view surface and cross section view of film samples are measured without gold sputtering. A Kratos Axis Ultra DLD X-ray photoelectron spectroscopy (XPS) spectrometer with monochromatic AlK_α (1486.69 eV) is operated to analyze the existence and chemical states of the elements in the prepared CZTS based samples. The High resolution XPS (HR-XPS) spectra are collected in a concentric hemispherical analyzer in a constant energy mode with pass energy of 20 eV and a step of 0.05 eV for narrow scan. The picture of the XPS system used in this work is shown in Figure 2.6. A TOF-SIMS system (TOF SIMS IV) with dual beam technique is applied in this work to perform elemental distribution profile analysis across the depth of film samples. A low energy sputter gun (Ar^+) with energy of 3 keV and current of 42 nA is raster over an area of 200μmx200μm for sample erosion and create the crater. High energy Bismuth ion (Bi^+) gun with energy of 25 keV and current of 0.4 pA is used for the analysis over an area of 100μmx100μm at the center of the crater created by the Ar^+ beam. The charging of the sample was neutralized by using a pulsed electron flood gun.

2.3.4 Nano-scratch and indentation

Film adhesion refers to the interfacial bond strength between coating and substrate, which is an important factor to evaluate film quality. [96-98] Experimentally, numerous techniques being developed to measure film adhesions according to different sample geometries, including simple scotch tape test, pull-off method, shock wave loading, indentation and scratch test.[97, 98] Among them the scratch test is widely used to measure adhesion/cohesion strength of thin films on micro- and nano-scales, which was firstly proposed by Heavens. [99] It is a simple method in which a stylus is drawn across the film under ramp loading (increasing load) until a film failure occurs at a critical load as shown in Figure 2.7. The critical loads, normal load ($F_{\perp}$) and lateral load ($F_{//}$), and failure modes reveal the adhesion performance and interfacial characteristics. [100-103]

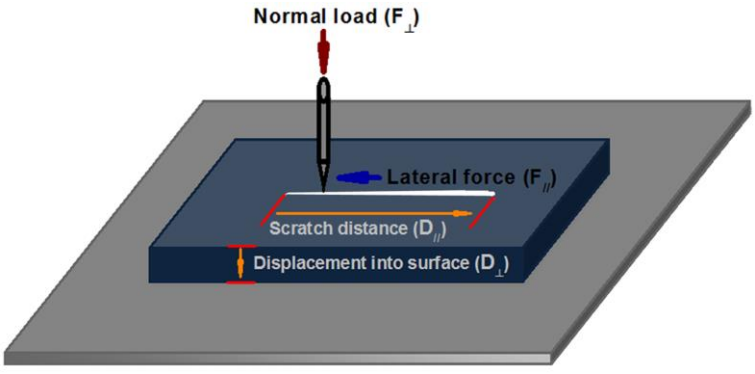

Figure 2.7 Schematic diagram of the nano-scratch measurement.

Nanoindentation testing is a powerful technique for mechanical characterization of thin films, such as elastic modulus and hardness. [104]

This technique measures the mechanical properties of a film through penetrating its surface with an indenter whose properties are already known. By continuously monitoring the load on the indenter and its depth into the sample, a displacement-load curve, consisting a loading and an unloading curves, can be obtained as plotted in Figure 2.8(a). Oliver and Pharr [105] have developed an analytical method to determine the mechanical properties directly from this displacement-load curve, in which the maximum load (P_{max}), the maximum displacement (h_{max}) and contact stiffness ($S=dP/dh$) at initial stage in the unloading curve are essentially required. The reduced modulus (E_r) and hardness (H) can be represented as

$$E_r = \frac{S}{2\beta}\sqrt{\frac{\pi}{A}} \tag{2-4}$$

$$H = \frac{P_{\max}}{A_{\max}} \tag{2-5}$$

where A and β are the projected area of indenter-sample contact and correction coefficient and P_{max} and A_{max} gives the maximum load and projected area of indenter-sample contact at the maximum load. In another aspect, the reduced modulus (E_r) can also be expressed as

$$\frac{1}{E_r} = \frac{1-\nu_S^{\,2}}{E_S} + \frac{1-\nu_I^{\,2}}{E_I} \tag{2-6}$$

with E_S, E_I, ν_S and ν_I representing the modulus and poisson ratio of the tested sample and indenter, respectively. Considering equations (2-4), (2-5) and (2-6), the modules and hardness of the measured film can be determined from the displacement-load curve, if the geometry and mechanical parameters of the

indenter are known. [105, 106]

In practice, the contact stiffness (S) can be measured by a continuous Stiffness measurement (CSM) method, which adds a harmonic force with a relatively high frequency to the increasing load (P) during test. [104-107] According to the indenting depth in the loading curve and parameters of the applied force, stiffness and hardness can be worked out. [107] It can provide continuous mechanical property variations with respect to penetration depth solely based on the loading curve. In this work, this method is also employed to measure the mechanical properties of the CZTS based films.

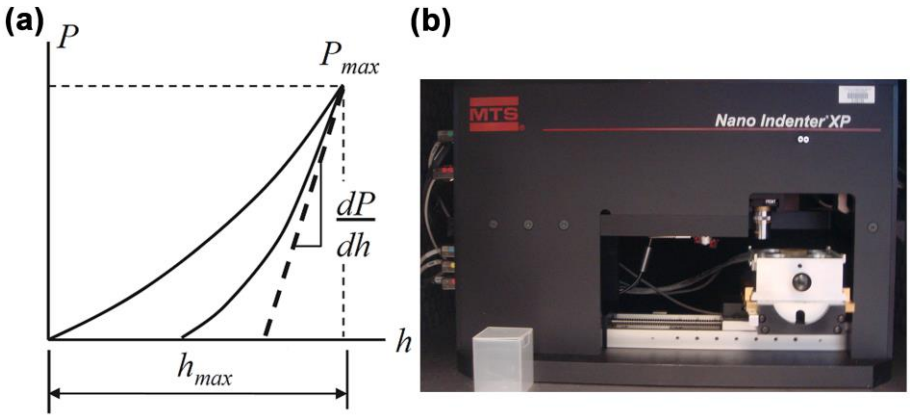

Figure 2.8 (a) Typical load-displacement curve of nanoindentation experiment and (b) the picture of the Nano Indenter® XP system.

In this work, a nano-indentation system (Nano Indenter® XP, MTS Corp. USA) is used to perform the scratch and indentation measurement as shown in Figure 2.8(b). A spherical sapphire indenter with radius of 1μm is applied for both tests. The modulus and Poissons ratio of the indenter are 400GPa and 0.25. In the scratch, a scratch length of 400μm, a maximum load of 50mN, a

scratch velocity of 2μm/s and a loading speed of 0.25mN/s are selected as the testing parameters. The indentation test is carried out at the continuous stiffness measurement mode with harmonic displacement of 2nm and frequency of 45Hz, and an indentation depth limit of 1000μm is applied. The loading and unloading curves together with elastic modulus and hardness changes versus the displacement into surface are automatically generated by the testing software.

2.4 Solar cell device characterization

The most fundamental solar cell characterization is to measure its efficiency and some other parameters. A current density *(I*) versus voltage (*V*) curve under a standardized sun light illumination gives critical parameters for a solar cell as depicted in Figure 2.9. [108] The relationships of the parameters, including short circuit current (I_{sc}), open circuit voltage (V_{oc}), fill factor (*FF*), maximum current (I_m), maximum voltage (V_m), maximum power (P_m), incident power (P_i) and conversion efficiency (η), are presented in equations (2-7) and (2-8). [108-110]

$$\eta = \frac{I_{sc} V_{oc} FF}{P_i} \tag{2-7}$$

$$FF = \frac{I_m V_m}{I_{sc} V_{oc}} \tag{2-8}$$

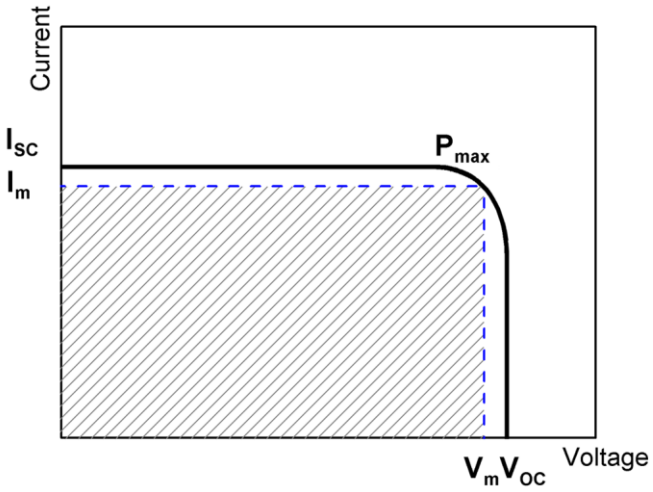

Figure 2.9 Typical I-V curve of a solar cell performance measurement.

In this work, the Newport's new Oriel *I-V* test station with Keithly 2420 serves as the electronic tester and light path controller. And one-sun of illumination (1 kW/m^2) is provided as the light source in the photoconduction measurement generated by the Newport 1000W Oriel® Solar Simulator.

Chapter 3 Study on the mechanism of CZTS phase decomposition

3.1 Introduction

In this chapter, thermal decomposition of CZTS is studied by comparative annealing under various temperatures and heat field directions. Phase transformations and elemental distributions in the annealed samples are measured. Kinetic analysis is carried out on individual metal elements (Sn and Cu) to give activation parameters in this complicated degradation process and further understandings on the basic decomposition mechanisms in CZTS are also obtained.

The following will be found from the research work in this chapter. During the Sn losses, we observe an unexpected two-mode vaporization process (equimolar and isobaric modes) on the front surface of the annealed samples, indicating different values of the molar enthalpy change in different temperature ranges under a given total pressure. In addition, studies on the back surface of the hot plate annealed samples reveal that a constant SnS loss would trigger the decomposition of CZTS system. Meanwhile, the recondensation of SnS at the back sides under a self-generated atmosphere indicates possible negative side-effects of annealing CZTS in a SnS rich ambiance, which is often adopted to compensate the Sn loss during heat

treatment.

Interestingly, besides the change from S^{2-} to S^{0}, an oxidation of Cu^{1+} to Cu^{2+} is also discovered. This provides another oxidizing process which could balance the reduction of Sn^{4+} to Sn^{2+} and possible non-uniform oxidative environments generated at elevated temperatures. During these transformations, a Cu-Zn separation along the heat field (Cu accumulated at the hot part and Zn at the cold part) is present in different annealing conditions.

3.2 Experimental details

CZTS powder samples were prepared through a chemical solution pyrolysis method discussed in Chapter 2. Then, the powder was pressed to round pellets with a diameter of 1cm for further experiments.

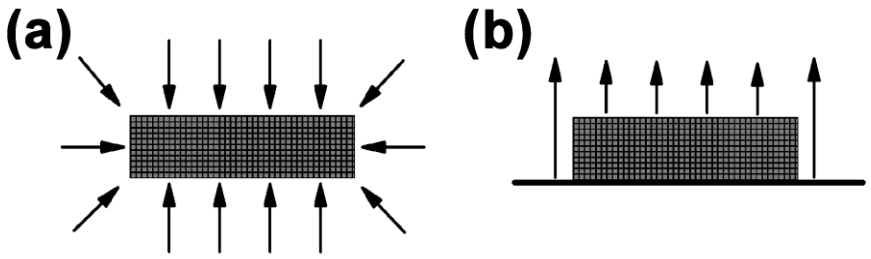

Figure 3.1 Schematic representation of the annealing environments for (a) tube furnace (TF) and (b) hot plate (HP).

In order to introduce different heat fields, a tube furnace and a specially designed hot plate were used to anneal the pellet samples at different temperatures (623K, 673K, 723K, 773K, 823K and 873K) for 1 hour. The

furnace tube and the hot plate were pumped by a turbo pump (Pfeiffer) with the pressure monitored by a vacuum gauge (Edwards).

In the tube furnace, an isotropic surrounded heat field was applied to the pellet (see Figure 3.1a). On the hot plate, a unidirectional field was applied to the pellet with the back surface contacting the plate (see Figure 3.1b). The temperatures of the heating sources, the ceramic tube surface of the furnace and the surface of the hot plate, were measured by standard k-type thermal couples. In both cases, the annealing ambient pressure was controlled to be around 10^{-1}Pa, which was similar to the equilibrium vapor pressure of SnS around 800K. No additional S or SnS vapor was added into the annealing chambers.

3.3 Results and discussion

3.3.1. Characterization of as-prepared CZTS powders

Before the annealing experiments, the as-prepared samples were characterized to confirm the single CZTS phase. The XRD pattern is presented in Figure 3.2(a). The diffraction peaks agree well with the kesterite CZTS (JCPDS #00-026-0575). As the tetragonal Cu_2SnS_3 and cubic ZnS share similar XRD pattern with CZTS, a Raman spectrum was used to exclude these phases as shown in Figure 3.2(b). The peak located at 334cm^{-1} belongs to CZTS phase [111-114] and no ZnS or Cu_2SnS_3 peaks appear.

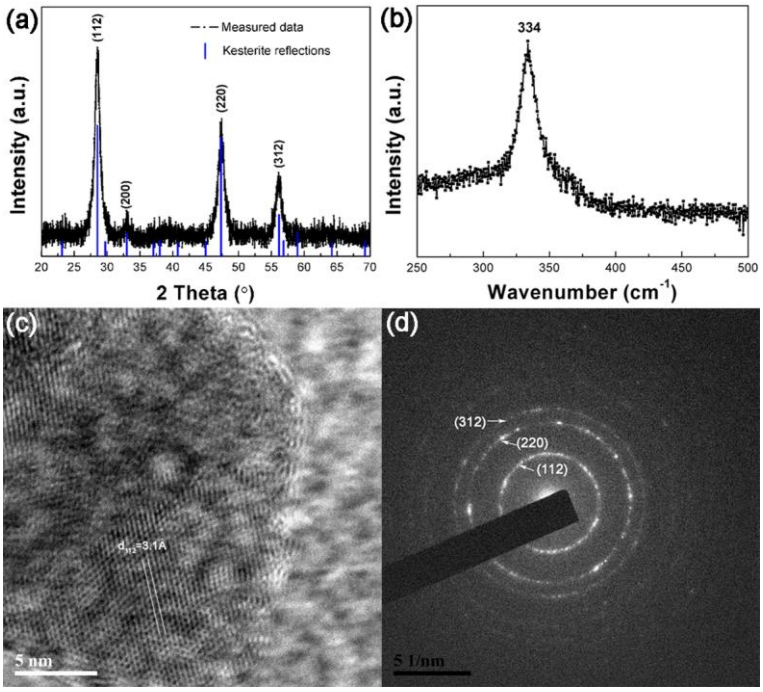

Figure 3.2 (a) XRD pattern; (b) Raman spectrum; (c) HR-TEM image and (d) Electron diffraction pattern of as-prepared CZTS sample.

The HR-TEM image and electron diffraction pattern of the CZTS powder are shown in Figure 3.2(c) and (d). The rings in the diffraction patterns can be assigned as the (112), (220), (312) planes of CZTS, which reveals a polycrystalline nature of the material. In addition, a clear lattice fringe with interplanar spacing of 3.1Å resolved as (112) lattice fringe was observed in Figure 3.2(c). These results are also consistent with the XRD patterns. Besides, the elemental ratios of Cu/(Zn+Sn), Zn/Sn and S/(Cu+Zn+Sn) determined by EDX were 1.02, 1.09 and 0.97, which were close to the expected stoichiometric ratio in CZTS.

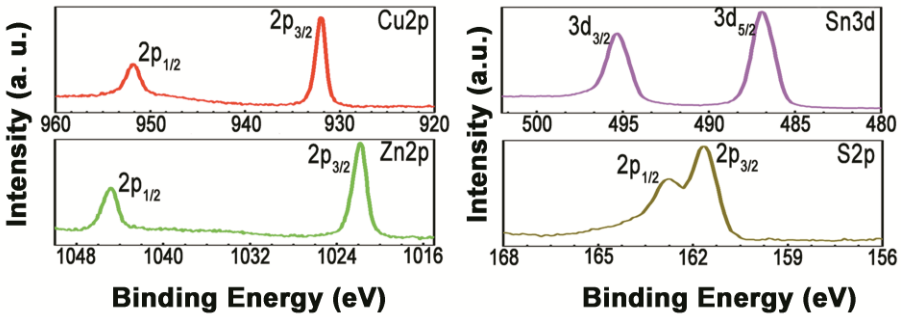

Figure 3.3 High-resolution XPS spectra of the CZTS sample.

Besides, the expected oxidation states of the elements in the Cu_2ZnSnS_4 sample are confirmed by high-resolution XPS analysis in Figure 3.3. The XPS data are just as measured. No fitting or smoothing is applied. The copper 2p spectrum shows two narrow and symmetric peaks at 932 and 951.8 eV, indicative of Cu(I) with a peak splitting of 19.8 eV. The zinc 2p peaks located at 1021.8 and 1044.8 eV show a peak separation of 23 eV, consistent with the standard splitting of 22.97 eV, suggesting Zn(II). The tin $3d_{5/2}$ peaks located at 486.9 and 495.4 eV, and a peak splitting of 8.5 eV indicates Sn(IV). The sulfur $2p_{3/2}$ and $2p_{1/2}$ peaks in the spectra are located at 161.7 and 162.8 eV, which are consistent with the 160-164 eV range expected for S in sulfide phases. The results are consistent with literature. [29, 112]

3.3.2. Annealing under isotropic surrounded heat fields

The pellet samples were annealed at 623K, 673K, 723K, 773K, 823K, and 873K with an isotropic surrounded heat field in the tube furnace. The XRD patterns of the samples at 723K, 773K and 823K are shown in Figure 3.4(a).

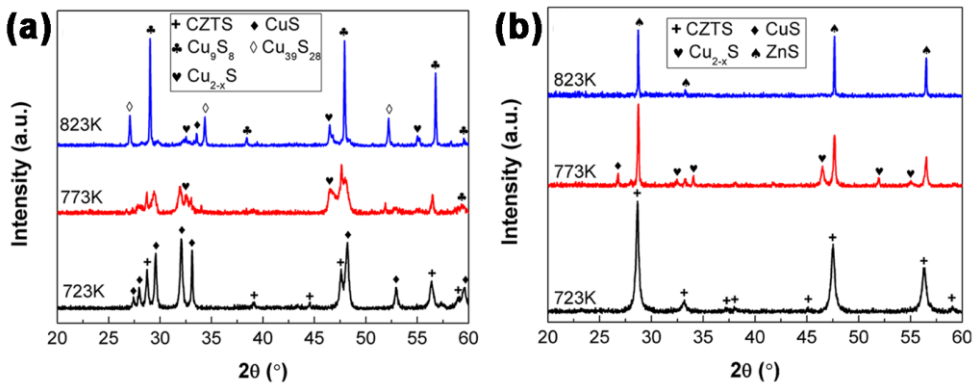

Figure 3.4 XRD patterns of (a) as-annealed and (b) TF-sanded samples at 723K, 773K and 823K, respectively.

The EDX measurement was performed to assist the identification of different phases. The samples only containing Zn and S are marked as ZnS phase, while those containing Cu, Zn, Sn and S are marked as CZTS phase regardless of any possible elemental ratio deviation. At 723K, other than the CZTS phase (PDF 26-0675), a CuS phase (PDF 65-3561) was formed which changed to sulfur deficient phases, such as Cu_9S_8 (PDF 36-0379), $Cu_{39}S_{28}$ (36-0380) and $Cu_{2-x}S$ (PDF 02-1292), at higher temperatures of 773K and 823K. The observation of copper sulfides is not new as surface Cu-S phase precipitations were often reported in the near stoichiometric CZTS. [57-59] Nevertheless, its separation mechanism was not well understood before, and in this chapter it will be discussed by our decomposition model later. By gently wiping the sample surface using a very fine sand paper (P320A), the upper blue CuS_x layer was removed easily. After removing the top layers, the samples (denoted as TF-sanded) were again characterized by XRD as shown in Figure 3.4(b). The detected phases were a pure CZTS phase at 723K, a mixture of

CZTS/ZnS and Cu-S phases at 773K and finally a pure ZnS phase at 823K. The Sn loss is accomplished through vaporization of SnS during annealing in vacuum.

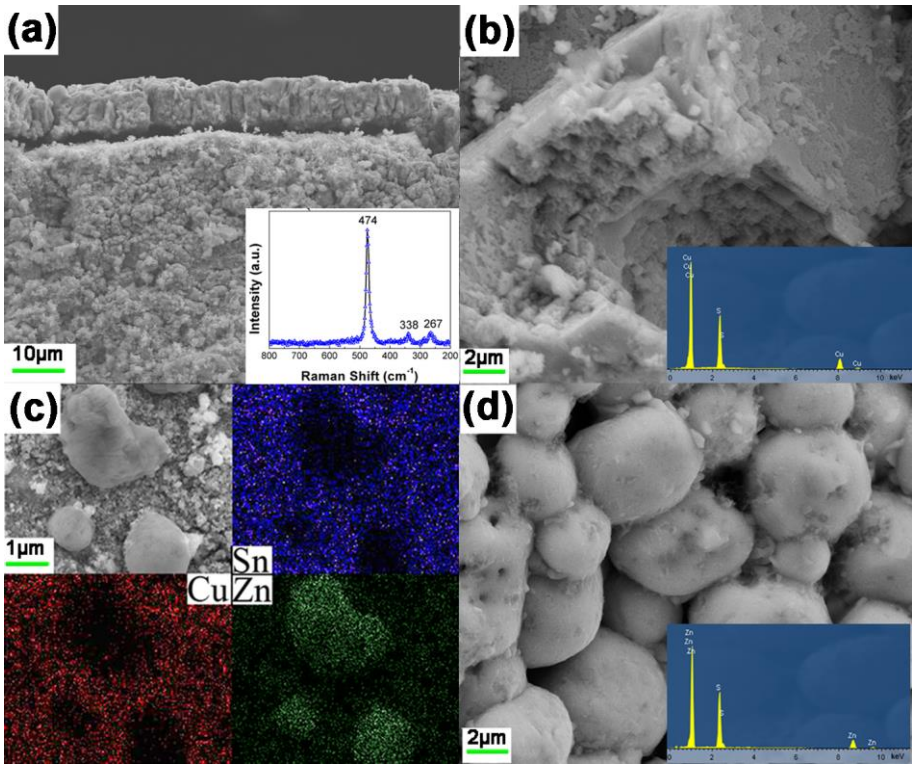

Figure 3.5 SEM images of (a) cross-section of as-annealed pellet and (c) surface sanded pellet with EDX-mapping on elements Sn, Cu and Zn at 723K, (b) as-annealed and (d) sanded surfaces with EDX patterns as inserts at 873K, respectively.

The SEM images of the cross section and the plan-view of the surface removed sample for the 723K annealed CZTS pellet were presented in Figure 3.5(a) and (c). Consistent with the XRD analysis, the pellet was found to be covered by a dense CuS layer (see Figure 3.5a). After removing the CuS layer, some big grains were observed to be embedded in the bulk CZTS layer (see Figure 3.5c), which were Cu and Sn deficient by EDX mapping analysis. The

SEM images of the surface and inner part of the sample annealed at 873K were shown in Figure 3.5(b) and (d). The surface was found to be a bulk Cu-S layer and the inside part was consist of pure ZnS grains, which were confirmed by EDX measurement as shown in the inserts of Figure 3.5(b) and (d).

3.3.3. Decomposition model

Considering the experimental observations discussed above, we would like to propose a reaction model to describe the basic decomposition mechanisms of CZTS material under a directional heat field. The decomposition of CZTS compound could be divided into several independent reactions distinguished by different metal species and reaction natures so that we can separate one complex transformation to several manageable processes. First, the decomposition should be originated near the surface and metal species need to dissociate from CZTS matrix and move to the reactive area. Although metal vacancies are expected to be formed at their original sites, we do not take account of these vacancies until the elements leave the material system as gas phases, because the transfer of later dissociated species would make these vacancies effectively occupied. No change in valance state of each metal is considered here. This is denoted as reaction type I in reaction 1-3, as seen below. We also focus on one metal species in each reaction and the rest is

summarized as δ. The oxidizing and reducing reactions made possible changes to the oxidation states for Sn and Cu, which is set as reaction type II in reactions 4 and 5. Holes and electrons are used as positive and negative charge units here. Another reaction concerning Cu vacancy or Cu_{Zn} antisite and free hole is also categorized as type II in reaction 6. This could be the major hole generating process in our material, since they are considered as the dominant acceptor defects in our materials. [13, 63] Lastly, the transition of SnS between solid and vapor phases (reaction 7) is given as reaction type III. The reactions involving each metal-species would occur successively. To complete the reaction series, the changes of oxidation and state of sulfur are combined in one reaction (reaction 8). Zn is known as the least active metal in these material reactions, and therefore we use Zn as the reference to normalize other metal species, 2Cu/Zn and Sn/Zn.

$$Cu_2ZnSn^{4+}S_4 \xrightarrow{\Delta G_{Sn}{}^1} Sn^{4+} + \delta_1 \quad \text{(reaction 1)}$$

$$Cu^{1+}{}_2ZnSnS_4 \xrightarrow{\Delta G_{Cu}{}^1} 2Cu^{1+} + \delta_2 \quad \text{(reaction 2)}$$

$$Cu_2Zn^{2+}SnS_4 \xrightarrow{\Delta G_{Zn}{}^1} Zn^{2+} + \delta_3 \quad \text{(reaction 3)}$$

$$Sn^{4+} \xrightarrow{\Delta G_{Sn}{}^2} Sn^{2+} + 2h^{1+} \quad \text{(reaction 4)}$$

$$Cu^{1+} + h^{1+} \xrightarrow{\Delta G_{Cu}{}^2} Cu^{2+} \quad \text{(reaction 5)}$$

$$V_{Cu}{}^{1+} / Cn_{Zn}{}^{1+} \xrightarrow{\Delta G_h} V_{Cu} / Cu_{Zn} + h^{1+} \quad \text{(reaction 6)}$$

$$Sn^{2+}(s) \xrightarrow{\Delta G_{Sn}{}^3} Sn^{2+}(g) + V_{Sn} \quad \text{(reaction 7)}$$

$$Cu_2ZnSnS^{2-}{}_4 \xrightarrow{\Delta G_S} 2S^0{}_2(g) + 4V_S + 8e^{1-} + \delta_4 \quad \text{(reaction 8)}$$

According to kinetic theory, the rate of any transformation reaction, *k*, can be

formulated by the generalized Arrhenius equation [115]

$$k = CT^n \exp(-\frac{\Delta G^*}{RT}) \tag{3-1}$$

where *R*, *T*, *ΔG** and *C* are the ideal gas constant, absolute temperature, standard Gibbs free energy of activation and a constant, respectively. The value of exponent *n* is dependent on the particular nature of a reaction. Type I (reaction 1-3) and type II (reaction 4-6) reactions could be governed by activated complex theory (*n*=1) and fast reaction theory (*n*=0), respectively.[116, 117] And type III reaction (7) follows Hertz-Langmuir vaporization theory with *n*=-1/2. [118]

Introducing thermodynamic term of Gibbs free energy change in equation 3-1 gives

$$k = CT^n \exp(-\frac{\Delta H^* - T\Delta S^*}{RT}) \tag{3-2}$$

in which *ΔH** and *ΔS** are molar enthalpy and entropy of activation, respectively.

From the reactions (1, 4 and 7) and the equations (3-1 and 3-2), the decomposition rate for Sn species can be written as

$$\begin{aligned} k_{Sn}{}^{\Pi} &= k_{Sn}{}^{1} \cdot k_{Sn}{}^{2} \cdot k_{Sn}{}^{3} \\ &= C_{Sn}{}^{1} T \cdot C_{Sn}{}^{2} \cdot C_{Sn}{}^{3} T^{-1/2} \cdot \exp(-\frac{\Delta G_{Sn}{}^{1} + \Delta G_{Sn}{}^{2} + \Delta G_{Sn}{}^{3}}{RT}) \\ &\propto T^{1/2} \exp(-\frac{\Delta H_{Sn}{}^{1} + \Delta H_{Sn}{}^{2} + \Delta H_{Sn}{}^{3}}{RT}) \end{aligned} \tag{3-3}$$

and for Cu species as

$$k_{\mathrm{Cu}}{}^{\Pi} = k_{Cu}{}^{1} \cdot k_{Cu}{}^{2}$$
$$= C_{Cu}{}^{1}T \cdot C_{Cu}{}^{2} \cdot \exp(-\frac{\Delta G_{Cu}{}^{1} + \Delta G_{Cu}{}^{2}}{RT}) \quad (3\text{-}4)$$
$$\propto T \exp(-\frac{\Delta H_{Cu}{}^{1} + \Delta H_{Cu}{}^{2}}{RT})$$

Thus the amount of metal species (α) moving out from the surface during a given time (t) could be expressed by

$$\alpha = k \cdot t \quad (3\text{-}5)$$

That leaves the residual amount of metal species (β) expressed as

$$\alpha = 1 - \beta \quad (3\text{-}6)$$

Substituting equation 3-5 in 3-6 and taking the natural logarithm, we obtain

$$\ln(1-\beta) = \ln\alpha = \ln(k \cdot t) \quad (3\text{-}7)$$

Substituting equations 3-3 and 3-4 into 3-7 gives

$$\ln(1-\beta_{Sn}) \propto -\Delta H_{Sn}{}^{\Sigma} / RT + \frac{1}{2}\ln T \quad (3\text{-}8)$$

for Sn-species with $\Delta H_{Sn}{}^{\Sigma} = \Delta H_{Sn}{}^{1} + \Delta H_{Sn}{}^{2} + \Delta H_{Sn}{}^{3}$ and

$$\ln(1-\beta_{Cu}) \propto -\Delta H_{Cu}{}^{\Sigma} / RT + \ln T \quad (3\text{-}9)$$

for Cu-species with $\Delta H_{Cu}{}^{\Sigma} = \Delta H_{Cu}{}^{1} + \Delta H_{Cu}{}^{2}$.

The elemental ratios of 2Cu/Zn (β_{Cu}) and Sn/Zn (β_{Sn}) on the samples after surface removal (TF-sanded) were listed in Table 3.1. It was found that the surface beneath the Cu-S layer was Cu and Sn deficient. β_{Cu} and β_{Sn} decreased with temperature increasing, and finally became a pure ZnS phase. By utilizing the basic discussion and kinetic derivation (equations 3-8 and 3-9), we obtain plots of ln(1-β_{Sn})-1/2ln(T) and ln(1-β_{Cu})-ln(T) with respect to 1/T in Figure 3.6(a) and (b).

Table 3.1 Normalized elemental ratio of Sn/Zn (β_{Sn}) and 2Cu/Zn (β_{Cu}) of the samples annealed in tube furnace after surface removement (TF-sanded) and the front (HP-front) and back (HP-back) surfaces of the samples annealed in hot plate at different temperatures (K). The surfaces of the HP-back samples below 823K are uniform, while three regions with various elemental ratios would appear at 823K and 873K.

Temperature/K		623	673	723	773	823	873
Sn/Zn (β_{Sn})	TF-sanded	0.95	0.85	0.54	0.09	0.02	0
	HP-front	0.99	0.97	0.89	0.46	0.19	0.06
	HP-back	1.01	1.32	3.18	4.79	0.02	0
						0.82	0
						0.05	0
2Cu/Zn (β_{Cu})	TF-sanded	0.89	0.74	0.57	0.43	0.14	0
	HP-front	0.87	0.85	0.52	0.24	0.05	0.025
	HP-back	1.03	1.12	1.16	1.16	0.18	0
						0.97	9.70
						3.34	50.25

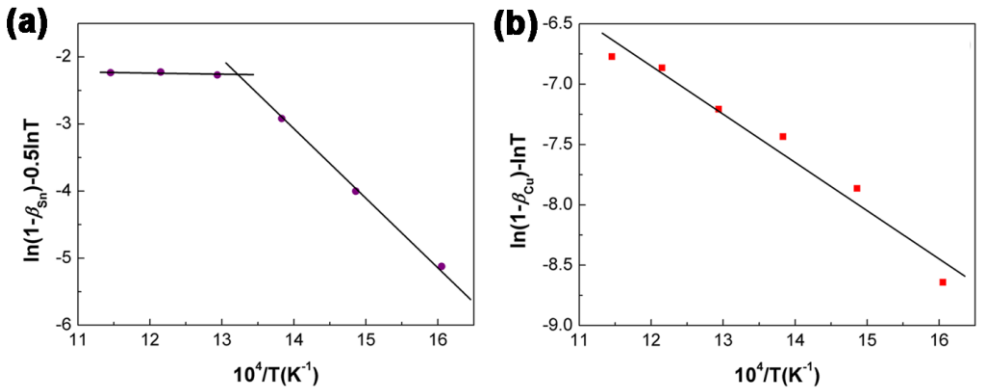

Figure 3.6 Arrhenius plots for (a) Sn loss and (b) Cu loss from the surface of TF-sanded samples.

For the Sn loss through the vaporization of SnS, the plot could be well fitted by two linear equations, which indicates a co-occurrence of two vaporization modes (equimolar and isobaric modes) in this process. These two modes could be distinguished by the relationship between the external pressure (P_{ext}) and the equilibrium value (P_{eqp}) of gas product, $P_{ext} < P_{eqp}$ for equimolar mode and

P_{ext} >> P_{eqp} for isobaric mode. [119-121] P_{ext} in this work is 10^{-1}Pa, and the ideal temperature (T_0) that keeps the P_{eqp} of SnS equivalent to P_{ext} (10^{-1}Pa) is about 800K (1/T =12.5×10^{-4}). [122] The mode transition temperature (T_{tra}) could be obtained by the intersection of these two lines. The product -$R\times\lambda$, where λ is the slope of the fitted line, gives molar enthalpy change (ΔH_{Sn}^{Σ}) values, with λ_L and ΔH_{SnL}^{Σ} for the low temperature region and λ_H and ΔH_{SnH}^{Σ} for the high temperature region. For the Cu species, the data could be fitted by a linear equation (see Figure 3.6b). The values of T_{tra}-T_0, ΔH_{SnL}^{Σ}, ΔH_{SnH}^{Σ} and ΔH_{Cu}^{Σ} are presented in Table 3.2 for further discussion.

With a uniformly surrounded heat field directed towards the sample surface (see Figure 3.1a) in the tube furnace, we could clearly see a Sn loss trough a two-mode process. A Cu-Zn separation with the Cu-S phases on the pellet surface and ZnS grains in the cold part inside the pellet was also observed.

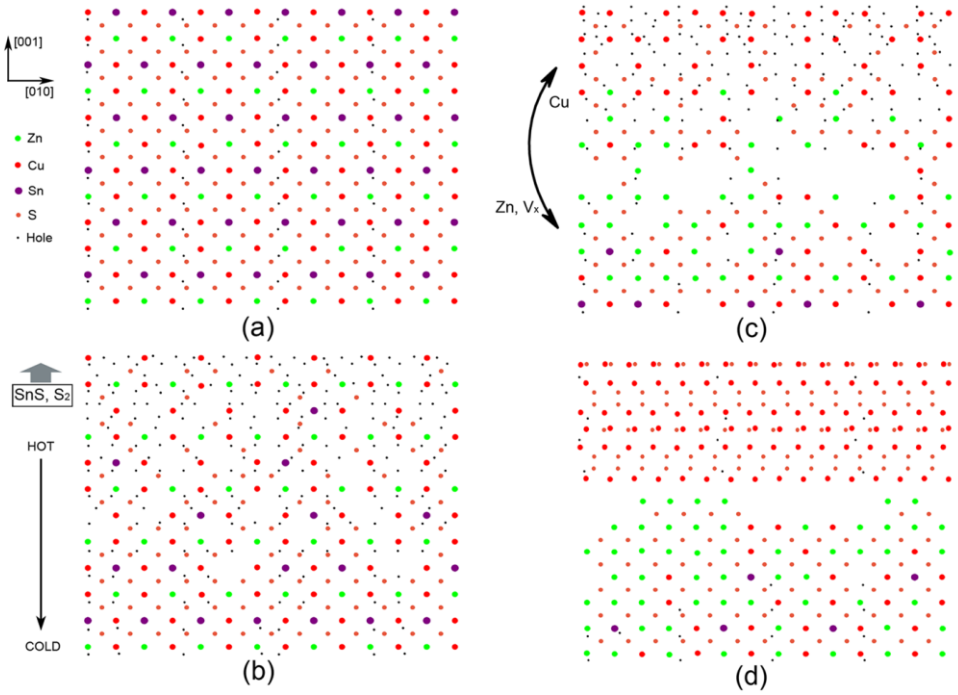

Figure 3.7 Schematic demonstration of the decomposition process of CZTS in vacuum (a) Original composition of CZTS, (b) Sn and S loss under a downward directed heat field, (c) migrations of ions and vacancies in the decomposed material and (d) phase segregation of Cu rich and Zn rich species.

In order to demonstrate the process of CZTS decomposition under a directional heat field, the projection of keterite CZTS lattice on (100) plane is plotted in Figure 3.7(a) and considered as the start of the decomposition. Volatile SnS and S_2 will be vaporized and result in many vacancies near the hot top surface area when a downward directed heat field is applied (see Figure 3.7b), which can be described by reaction 1, 4 and 8. Meanwhile, the hole concentration at the hot area should be higher than the cold part. The reaction described by reaction 6 could be considered as the major hole generating process. Therefore, the hot surface turns to be a more oxidative area with many vacancies that could create easy paths for Cu transfer.

It was reported that the activation energy for the position exchange of Cu and

Zn is very small (50meV) in CZTS. [4] Thus, it is reasonable for Cu^{1+} (low oxidation state) ions to move from the interior cold area to the hot surface part through Cu-Zn and Cu-Vacancy exchanges. Then, they are oxidized to Cu^{2+} by further sulfurization of a continuous sulfur flow decomposed from the beneath layer and consume extra holes. During these transformations, the top surface will become Cu rich leaving a beneath Zn rich surface with void space in between (see Figure 3.7c). Finally, the re-crystallizations occur in both Cu rich and Zn rich regions to reduce the total system energy, resulting in the Cu-Zn phase separation (see Figure 3.7d).

3.3.4. Annealing under a unidirectional heat field

In order to check the model proposed above, we introduced a unidirectional heat field by a hot plate placed in a vacuum sealed chamber (see Figure 3.1b) to anneal the CZTS pellet samples. In addition to the SnS loss, the model also predicts a Zn rich front surface and a Cu rich back surface under an upward directed heat field in this case.

The EDX analysis results of metal elemental ratios on both the sides of the hot plate annealed sample (HP-front and HP-back) were listed in Table 3.1. For the cold front surface, β_{Sn} and β_{Cu} decreased with temperature increasing from 623K to 873K, which agrees with the prediction of the model. The XRD patterns of the front surfaces of the samples annealed at 723K and 873K were

presented in Figure 3.8(a). The CZTS (PDF 26-0675) and ZnS (PDF 39-1363) phases were measured on the front surface of 723K and 873K annealed samples, which is also consistent with the elemental ratios characterized by EDX (see Table 3.1).

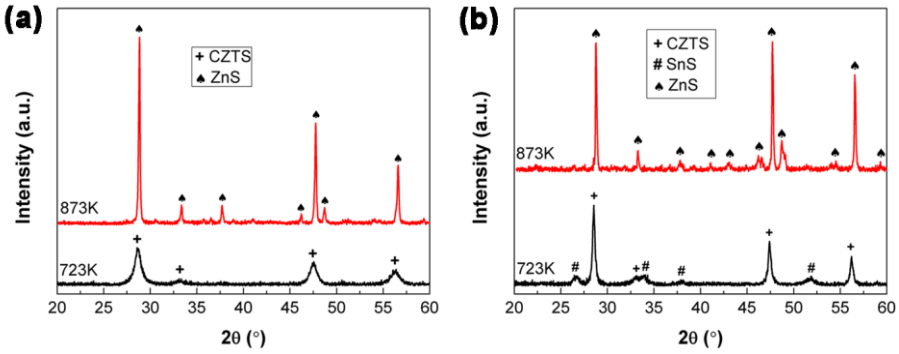

Figure 3.8 XRD patterns of (a) HP-front and (b) HP-back surfaces of the samples annealed at 723K and 873K, respectively.

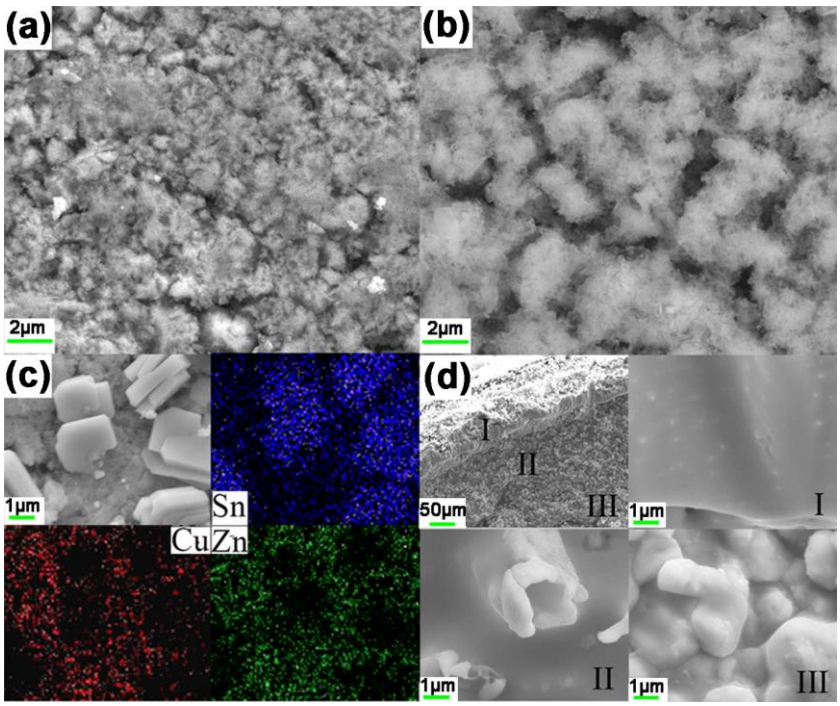

Figure 3.9 SEM images of front surfaces at (a) 723K and (b) 873K and back surfaces at (c) 723K and (d) 873K of the samples annealed in hot plate. EDX elemental mapping of (c) and magnified SEM images of different areas in (d) were also presented.

The SEM images of these two sample surfaces were shown in Figure 3.9(a) and (b). The surface particle size and porosity of the sample annealed at 873K are larger than the one annealed at 723K. The porosity could be resulted from the vaporization of SnS and S_2 and the movement of Cu species as indicated in the model. The residual Zn rich phase will grow bigger, which can be confirmed by the decreased peak full width at half maximum (see Figure 3.8a).

Plots of $\ln(1-\beta_{Sn})-1/2\ln(T)$ and $\ln(1-\beta_{Cu})-\ln(T)$ with respect to 1/T for the HP-front surface were presented in Figure 3.10. Similar to the TF-sanded sample, the Sn loss on the surface of the HP-front sample undergoes a two-mode transition and the transition temperature difference (T_{tra}-T_0) and molar enthalpy changes (ΔH_{SnL}^{Σ} and ΔH_{SnH}^{Σ}) extracted from the slopes of the fitted lines were shown in Table 3.2. A linear fitting was also obtained for the Cu-species and its molar enthalpy changes (ΔH_{Cu}^{Σ}) was listed in Table 3.2, too.

Table 3.2 Fitted values of (T_{tra}-T_0), ΔH_{SnL}^{Σ}, ΔH_{SnH}^{Σ} and ΔH_{Cu}^{Σ} for the surface of TF-sanded and HP-front samples, respectively.

Fitted value	$(T_{tra}-T_0)$/K	ΔH_{SnL}^{Σ}/Jmol^{-1}	ΔH_{SnH}^{Σ}/Jmol^{-1}	ΔH_{Cu}^{Σ}/Jmol^{-1}
TF-sanded	−43	79907.298	1276.416	33224.211
HP-front	−11	82204.182	9121.887	36636.297

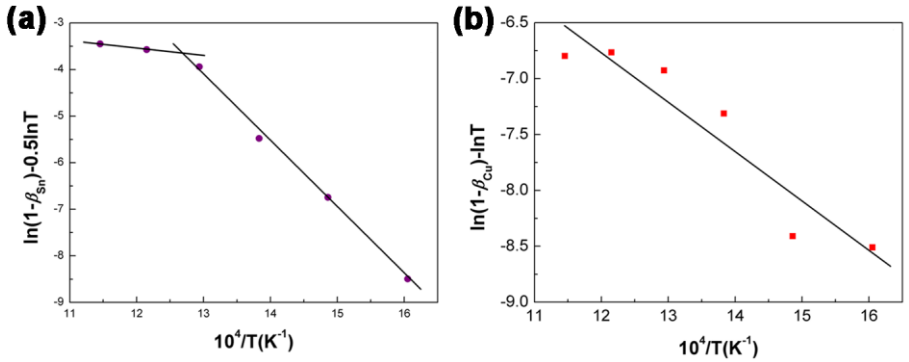

Figure 3.10 Arrhenius plots for (a) Sn loss and (b) Cu loss from front surface of the samples annealed in hot plate (HP-front).

The experimentally determined mode-transition temperatures (T_{tra}) in both cases are smaller than the ideal one (T_0) in Table 3.2. The external pressure (P_{ext}) in the experiment is the total pressure of the gas products and background atmosphere, thus the partial pressure of the gaseous products (SnS or S_2) should be smaller than P_{ext}. A shift of the ideal transition temperature (T_0) to a lower temperature should be considered, when we make use of the equilibrium vapour pressure of SnS (P_{eqp}). It is reasonable to obtain smaller mode-transition temperatures in this work and the exact T_{tra} value may vary in different conditions (such as the existence of the surface CuS layers). In both cases, the total molar enthalpy changes at a low temperature region (ΔH_{SnL}^{Σ}) are similar but much larger than their counterparts at a high temperature region (ΔH_{SnH}^{Σ}), which indicates a significant decomposition energy barrier decrease when the temperature increased above T_0. At a high temperature region, the ΔH_{SnH}^{Σ} value of the TF-sanded sample is smaller than the HP-front one, which may be resulted from the interaction of the Sn loss with the Cu movement. For the TF-sanded one, the Cu moves towards outside.It shares the

same transfer direction with the Sn species and could create more vacancies to assist Sn transport. While for the HP-front one, Cu needs to move downward, which has an opposite direction with the Sn species and may block the Sn movement. Due to the same reason, the total molar enthalpy change of Cu-species (ΔH_{Cu}^{Σ}) for HP-front sample should be bigger than the TF-sanded case.

For the back surface, an upward bending of the samples occurred at elevated temperature that left the round edge contacted with the plate, generating a dome-like space between the back surface and the plate. This deformation is unexpected, though it fortunately provides more decent insights to the decomposition mechanisms.

From the XRD patterns shown in Figure 3.8(b), instead of the Cu-S phases appeared on the hot surface of the TF-annealed sample, the Sn-S and CZTS phases were found on the HP-back sample at 723K. Correspondingly, square shaped crystallites were observed on the back surface of the sample (see Figure 3.9c), which were confirmed to be SnS by EDX elemental mapping. This SnS phase did not appear on the sample annealed at 873K, while a Zn-S and Cu-S phase segregation upon the radial direction was observed (see Figure 3.9d). A dense Cu-S phase at the edge area (I), a Zn-S phase at the central area (III) and a mixed Cu-Zn-S phase at the area (II) near the edge of the pellet were analyzed by SEM and EDX. In this case, the edge is the hot end due to its direct contact with the plate and the heat field here is from the edge to the

central part. Applying the decomposition model proposed above, the hot edge should have Cu rich phases and the centre should have Zn rich phases. There is still a good match between the experimental phenomena and the model. There is only ZnS phase (PDF 39-1363) detected in the XRD pattern (see Figure 3.8b), because the effective measured area was the central part (III).

In Table 3.1, the β_{Cu} values of the HP-back samples from 623K to 773K were just around 1. But at 823K and 873K, the β_{Cu} can be divided to several values in different areas. The β_{Sn} value increased above 1 from 623K to 773K, and then dropped sharply when the temperature exceeded 773K.

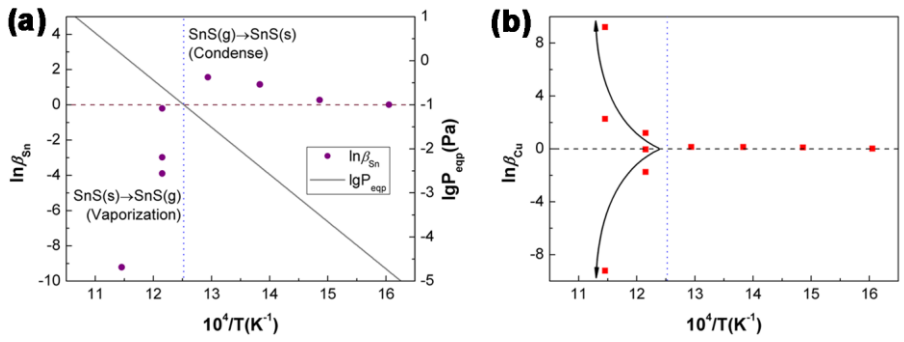

Figure 3.11 Plots of lnβ with respect to 10^4/T for (a) Sn and (b) Cu on back surface of the samples annealed in hot plate.

To illustrate the above change, plots of lnβ_{Sn} and lnβ_{Cu} with respect to 1/T were presented in Figure 3.11(a) and (b), respectively. The vapor pressure curve of SnS and $10^4/T_0$ (vertical dot line) were also plotted in Figure 3.11(a). The lnβ_{Sn} data were divided into two regions by T_0, lnβ_{Sn}>0 when T<T_0 and lnβ_{Sn}<0 when T>T_0. When T<T_0, the total pressure near the back surface is much higher than P_{eqp} and certain vaporized SnS was expected to be enclosed

within the self-generated space, so the SnS vapor could condense back onto the pellet surface. When $T>T_0$, the total pressure becomes smaller than P_{eqp}, so the SnS will be vaporized and eliminated from the sample. This process agrees well with the established congruent dissociative vaporization (CDV) decomposition mechanism. [120]

The $\ln\beta_{Cu}$ data were also divided into two parts by T_0, $\ln\beta_{Cu}\approx0$ when $T<T_0$ and a segregation to Cu-poor and Cu-rich regions when $T>T_0$. Before a severe vaporization loss of SnS, the $\ln\beta_{Cu}$ did not change significantly and the whole CZTS system was relatively stable. It is the effective SnS loss that triggers and exaggerates the decomposition of CZTS. Therefore, it is important to include some SnS vapor in the annealing environment. These conclusions are also consistent with others' experimental observations. [55, 56]

3.4 Conclusion

Heat field stimulated decomposition reactions in CZTS were studied through a systematic annealing experiment in this chapter. Isotropic surrounded and unidirectional heat fields were realized by using a tube furnace and a specially designed hot plate, respectively. The decomposition kinetic analysis demonstrated an equimolar-isobaric mode transition during the process of Sn loss. A self-generated SnS contained atmosphere was found to be helpful to stabilize the CZTS system, but the re-solidification of SnS on the HP-back

samples indicated possible negative influences of an over saturated SnS ambiance. Thus, a relatively high total pressure and carefully controlled SnS concentration are required to keep CZTS stable and avoid possible SnS condensation in any post-annealing treatment. Besides, a Cu-Zn separation was observed along the applied heat field with Cu-S phases appeared near the hot area and Zn-S phases near the cold area. In this transformation, the oxidation of Cu^{1+} to Cu^{2+} was believed to be another mechanism other than the change of S^{2-} to S^{0} that would compensate the reduction variations, like the valance alternation of Sn^{4+} to Sn^{2+} and the unbalanced carrier generation.

A decomposition reaction model of CZTS under the directional heat field was also proposed in this work. The degradation process initiated from Sn-S loss and non-uniform carrier redistribution under an elevated temperature gradient. Cu^{1+} ions were found transferring to the hot end of the sample through exchanging with Zn and vacancies. They can be oxidized to Cu^{2+} by the sulfurization of later decomposed sulfur and balance the carrier concentration and other oxidation state changes. Further losses of SnS and S_2 would exaggerate these transformations and finally realize a Cu-Zn separation.

Finally, according to these understandings of the decomposition mechanisms in CZTS, a film deposition method is proposed, which includes a low temperature precursor preparation in vacuum and a high pressure selenization/sulfurization.

Chapter 4 Study on the mechanism of secondary phase formation in CZTSSe films

4.1 Introduction

Principally, a dense CZTS film is required for a solar cell fabrication. However, the CZTS material synthesized by the chemical route used in this work is hard to form a high quality film to prepare a solar cell. Therefore, the vacuum deposition is introduced in this Chapter and later to prepare CZTS based films. Following the film deposition strategy obtained from the studies in Chapter 3, the phase formation issues in Cu-Zn-Sn-S-Se system are explored in this chapter by using low temperature co-evaporated precursors with relatively high pressure annealing treatments. Different binary secondary phases are unsurprisingly detected when the precursors are prepared with different metal ratios. However, the preferred aggregation locations of different impurities turn to be unexpected and interesting, Cu_xSe and SnSe on the top surface and ZnS at the bottom of the film. Then, a temperature dependent annealing study is conducted to reveal the formation processes. After that, an optimum CZTSSe film growing pathway can be obtained after careful identifications and study of morphologies and phases in different temperature annealed samples. A deeper understanding on the reaction principles is obtained through systematic

thermodynamic calculations that provide convincing explanations for the experimental phenomena including secondary phase formation, phase reaction sequences and impurity segregations. The knowledge achieved can help us understand this CZTSSe system better for improving film deposition designs to control and minimize secondary phases, which are very important in achieving promising film structures for CZTSSe solar cells.

4.2 Experimental details

$Cu_2ZnSn(S,Se)_4$ films were deposited through a co-evaporated Cu-Zn-Sn-S precursor with post selenization route. Three effusion cell sources of Cu(99.9999%, Alfa Aesar), Sn(99.999%, Maylontech) and ZnS(99.995%, Alfa Aesar) were simultaneously evaporated with a temperature accuracy of 1℃. The elemental ratios were adjusted by individual temperature controls. The substrate is bare glasses without Mo-coating in this chapter to avoid the confusion from possible decomposition reactions of CZTS(e) with Mo, because Mo was proposed to be the cause of phase segregation at bottom of CZTSSe film. [123] The glasses were cleaned in an ultrasonic bath with Micro 90 solution (Sigma-Aldrich), acetone, ethanol and DI water and then dried by blowing N_2 gas before loading into the vacuum chamber. The substrate was not deliberately heated during deposition and the temperature was around 40-60℃, due to the source radiation and energy transferred from the

evaporated atoms. The background pressure of the chamber was $<5\times10^{-5}$Pa and the working pressure was around 1×10^{-3}Pa. Four types of precursors were prepared, which are Sn rich, Sn poor, Zn rich and ratio right according to their compositions.

The post-selenization was carried out in a tube furnace equipped with a vacuum pump and Ar gas flow. The tube was firstly pumped for 30 minutes and filled with Ar gas, and then pumped again for 30 minutes to purge air. The Cu-Zn-Sn-S precursors were sealed in a graphite box together with Se powder (99.999%, Aldrich). The four precursors were annealed at 520 ℃ for 10 min in Ar gas with a pressure around 1×10^{5}Pa. In order to reduce artificial disturbance to the precursors, no extra SnS(e) was introduced and the elimination of the SnS(e) loss is achieved by relatively high pressure and short time annealing based on the discussions presented in Chapter 3. The right ratio sample underwent an additional annealing at 280 ℃, 340 ℃, 400 ℃, 460 ℃ and 520 ℃ for 10 min. The heating rate was 20 ℃/min and the samples were cooled down naturally.

4.3 Results and discussion

4.3.1 Characterization of Cu-Zn-Sn-S precursors

Cu-Zn-Sn-S precursor films were prepared with different elemental ratios by controlling evaporation temperatures of Cu, Sn and ZnS sources. The relative

elemental ratios of four precursors are listed in Table 4.1. According to their compositions, they are named as ratio right, Sn rich, Sn poor and Zn rich, respectively. The ratio right sample is presented as the representative of these precursors and characterized as shown in Figure 4.1.

Table 4.1 Elemental ratios of ratio right, Sn rich, Sn poor and Zn rich precursors (Pre-Se) and selenized samples (Aft-Se) determined by top view EDX measurements.

	ratio right		Sn rich		Sn poor		Zn rich	
	Pre−Se	Aft−Se	Pre−Se	Aft−Se	Pre−Se	Aft−Se	Pre−Se	Aft−Se
Cu/(Zn + Sn)	0.95	0.96	0.75	0.89	0.94	1.26	0.87	0.97
Cu/Sn	1.87	1.88	1.14	1.47	2.64	2.51	1.97	1.91
Zn/Sn	0.97	0.97	0.53	0.65	1.82	1.00	1.26	0.98
(S + Se)/(Cu + Sn + Zn)	0.26	1.02	0.19	1.06	0.34	1.05	0.29	1.02
Se/(S + Se)	0	0.75	0	0.87	0	0.74	0	0.78

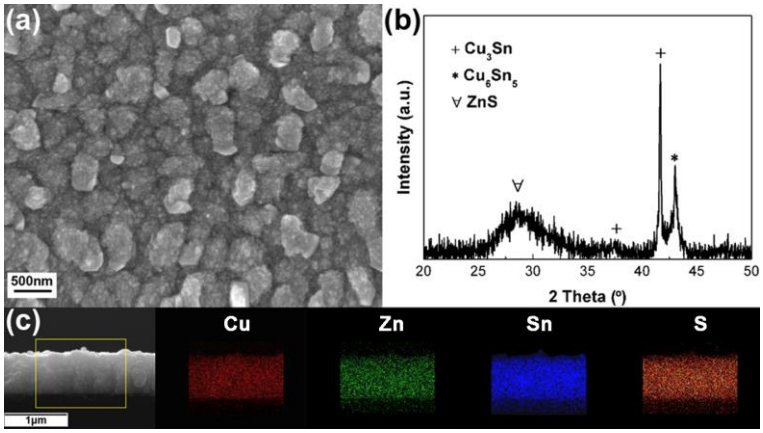

Figure 4.1 (a) Top-view SEM, (b) XRD pattern and (c) Cross-section view SEM and EDX elemental mapping of the as-deposited ratio right precursor sample.

Figure 4.1(a) and (c) show the surface and cross-section morphologies and elemental EDX mappings of the as-deposited ratio right sample, which reveals a dense film of about 650nm thick with a uniform distribution of Cu, Sn, Zn and S. The XRD diffraction peaks at 37.7 °, 41.7 ° and 43.3 ° in Figure 4.1(b)

can be indexed as Cu_3Sn (PDF #01-1240) and Cu_6Sn_5 (PDF #45-1488) alloy phases. Another wide peak at around 28.6 ° is correlated to ZnS phase (PDF #65-0309).

Thermodynamic analysis can generally determine phase stability and preference of particular reactions. Ideal theoretical thermodynamic simulations on the phase and defects formation of CZTS(e) have been conducted to provide much information on their properties. [13, 124-126] Otherwise, calculations based on experimental thermodynamic parameters can also give practical judgments of certain reactions to understand existing phenomena and guide further adjustment. [127, 128] To clarify the calculation, one example reaction is proposed by equation (4-1):

$$A + B \leftrightarrow C + D \tag{4-1}$$

in which *A* and *B* are reactants and *C* and *D* are products. If the standard molar enthalpy ($H_{298}{}^0$), standard molar entropy ($S_{298}{}^0$), phase transition temperature (T_{tr}) and transition enthalpy change (ΔH_{tr}) for all reactants and products are known, we can calculate the relationship of the Gibbs free energy change of this reaction ($\Delta G_T{}^0$) with temperature as follows, [129]

$$\Delta G_T^0 = (\Delta H_{298}^0 \pm \sum \Delta H_{tr}) - T(\Delta S_{298}^0 \pm \sum \frac{\Delta H_{tr}}{T_{tr}}) \tag{4-2}$$

in which

$$\Delta H_{298}^0 = (H_{298,C}^0 + H_{298,D}^0) - (H_{298,A}^0 + H_{298,B}^0)$$

$$\Delta S_{298}^0 = (S_{298,C}^0 + S_{298,D}^0) - (S_{298,A}^0 + S_{298,B}^0)$$

$\Delta H_{298}{}^0$ and $\Delta S_{298}{}^0$ are standard reaction enthalpy and entropy change. $\Sigma \Delta H_{tr}$

represents the total phase transition enthalpy change. When it is product, + is applied and when it is reactant, - is applied. It should be noted that the first approach calculation of Gibbs-Helmholtz equation is used here, which assumes no specific reaction heat change at a constant pressure. Theoretically, the accuracy of this approach is acceptable to analyze reactions. [127, 129]

For the reaction that involves one vapor phase reactant (product), the equilibrium reaction pressure of the vapor P is given by, [127, 128, 130]

$$\lg(P) = \frac{-\Delta G_T^0}{2.303RT} \tag{4-3}$$

in which R is the ideal gas constant. In our cases, the phase formation reactions generally involve one vapor item during post sulfurization (S) or selenization (Se). Therefore, a temperature dependent equilibrium S(e) vapor pressure ($P_{S(e)}$) curve can be deduced by combining equations (4-2) and (4-3), that will provide straight forward connections to the experimental conditions.

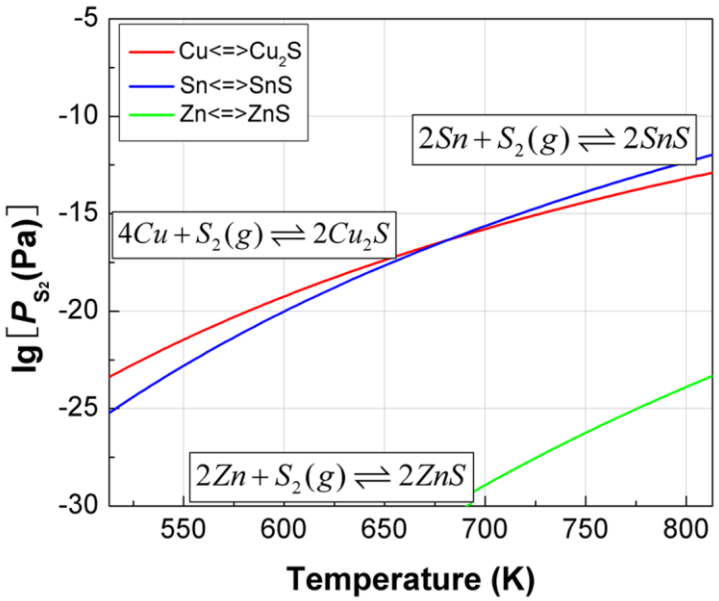

Figure 4.2 Calculated equilibrium S_2 vapor pressure versus temperature for the sulfurization reactions of Cu, Sn and Zn.

To understand the formation of the phases of Cu-Sn alloys and ZnS in the as-grown precursor film, let us analyze these three metal sulfurization reactions. The reactions are presented as R1-3 in Table 4.2, and the reaction Gibbs free energy change (ΔG) is also calculated using corresponding thermodynamic data according to equation (4-2). Furthermore, temperature dependent curves of S_2 pressure over sulfide products are plotted in Figure 4.2 based on equation (4-3). The equilibrium S_2 pressure over ZnS is far lower than those over Cu_2S and SnS, indicating that Zn is much easier to be sulfurized than Cu and Sn under the same S_2 pressure. This can interpret why only Zn becomes a sulfide phase in our S deficient Cu-Zn-Sn-S precursors, and the other two metals exist as alloy forms.

Table 4.2 Related Sulfurization and selenization reactions and their Gibbs free energy change within the temperature range of 513~813K. Data used to calculate are from the literatures. [126, 131-135]

reaction	ΔG_r(J·mol^{-1})	T (513–813 K)
R1: $2Zn + S_2(g) \rightleftharpoons 2ZnS$	$\Delta G_{Zn-S} = -531996 + 195.8T$	(T < 693 K)
	$\Delta G_{Zn-S} = -539318 + 216.9T$	(T > 693 K)
R2: $2Sn + S_2(g) \rightleftharpoons 2SnS$	$\Delta G_{Sn-S} = -352419 + 204.3T$	
R3: $4Cu + S_2(g) \rightleftharpoons 2Cu_2S$	$\Delta G_{Cu-S} = -279952 + 98.2T$	(T < 623 K)
	$\Delta G_{Cu-S} = -278278 + 95.5T$	(T > 623 K)
R4: $2Zn + Se_2(g) \rightleftharpoons 2ZnSe$	$\Delta G_{Zn-Se} = -456169 + 189.5T$	
R5: $2Zn + Se_2(g) \rightleftharpoons 2SnSe$	$\Delta G_{Sn-Se} = -327301 + 153.0T$	
R6: $4Cu + Se_2(g) \rightleftharpoons 2Cu_2Se$	$\Delta G_{Cu-Se} = -256759 + 79.5T$	
R7: $^4/_3Cu_3Sn + Se_2(g) \rightleftharpoons 2Cu_2Se + {}^4/_3\ Sn$	$\Delta G_{Cu_3Sn-Se} = -259582-85.9T$	
R8: $^2/_3Cu_6Sn_5 + Se_2(g) \rightleftharpoons 2Cu_2Se + {}^{10}/_3\ Sn$	$\Delta G_{Cu_6Sn_5-Se} = -265999-188.6T$	
R9: $2ZnS + Se_2(g) \rightleftharpoons 2ZnSe + S_2$	$\Delta G_{ZnS-Se} = -75827 + 6.3T$	
R10: $2Cu_2Se + 2SnSe + Se_2(g) \rightleftharpoons 2Cu_2SnSe_3$	$\Delta G_{Cu_2SnSe_3} = -232055 + 220.4T$	
R11: $2SnSe + Se_2(g) \rightleftharpoons 2SnSe_2$	$\Delta G_{SnSe-Se} = -198435 + 207.1T$	
R12: $Cu_2Se + SnSe_2 + ZnSe \rightleftharpoons Cu_2ZnSnSe_4$	$\Delta G_{CZTSe} = -37582 + 1.4T$	
R13: $2Cu_2Se + 2SnSe + 2ZnSe + Se_2(g) \rightleftharpoons 2Cu_2ZnSnSe_4$	$\Delta G_{CZTSe-Se} = -273599 + 209.9T$	
R14: $2SnS + S_2(g) \rightleftharpoons 2SnS_2$	$\Delta G_{SnS-S} = -219032 + 207.1T$	
R15: $Cu_2S + SnS_2 + ZnS \rightleftharpoons Cu_2ZnSnS_4$	$\Delta G_{CZTS} = -101667 + 6.7T$	(T < 623 K)
	$\Delta G_{CZTS} = -102504 + 8.0T$	(T > 623 K)
R16: $2Cu_2S + 2SnS + 2ZnS + S_2(g) \rightleftharpoons 2Cu_2ZnSnS_4$	$\Delta G_{CZTS-S} = -422366 + 220.5T$	(T < 623 K)
	$\Delta G_{CZTS-S} = -424040 + 223.1T$	(T > 623 K)

4.3.2 Analysis of the selenized samples with different compositions

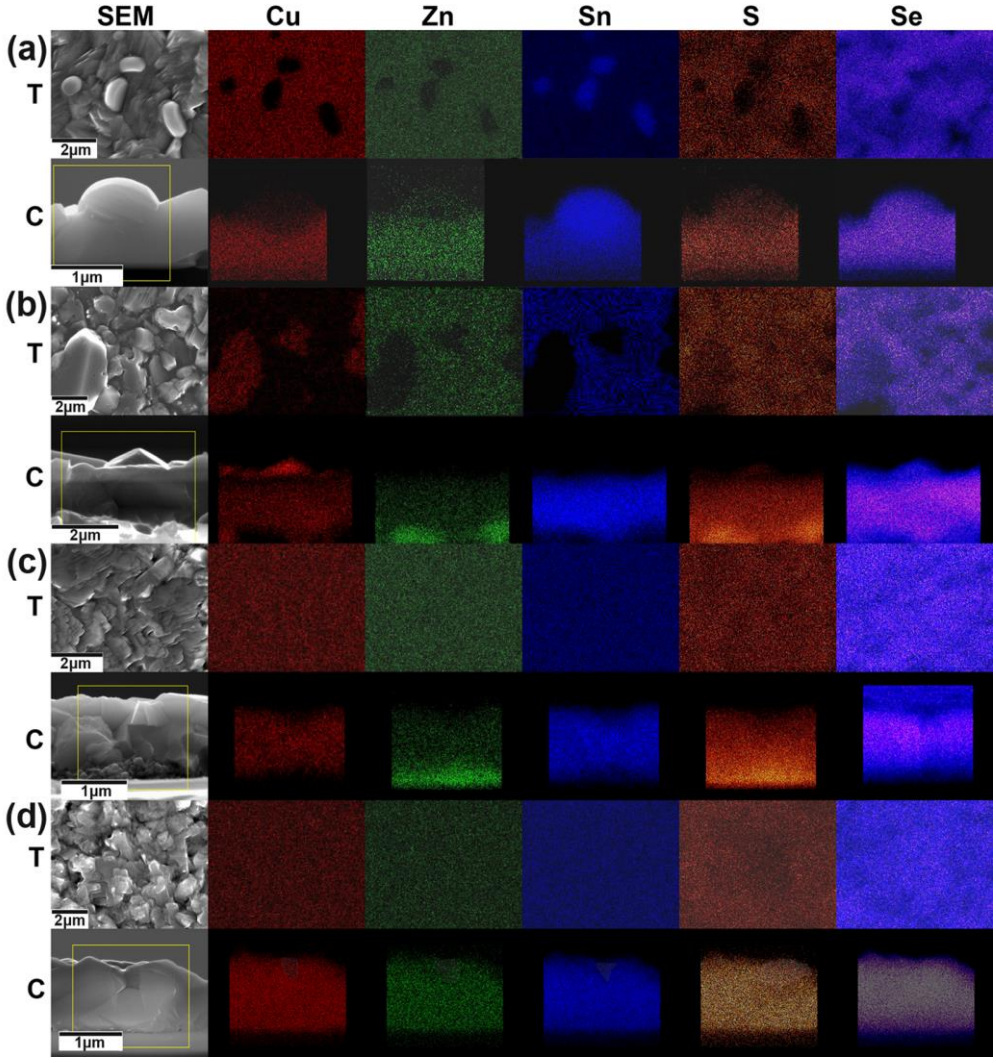

Figure 4.3 Top view and cross-section view SEM images and EDX mappings of the selenized samples, (a) Sn rich, (b) Sn poor, (c) Zn rich and (d) ratio right.

Figure 4.3 shows SEM images and elemental mappings of the (a) Sn rich, (b) Sn poor, (c) Zn rich and (d) ratio right product samples after selenization at 520℃, in which T and C represent top view and cross-section view. The thickness of these samples is controlled around 1.5~2.0μm. XRD and Raman patterns of these four samples are plotted in Figures 4.4 and 4.5, respectively.

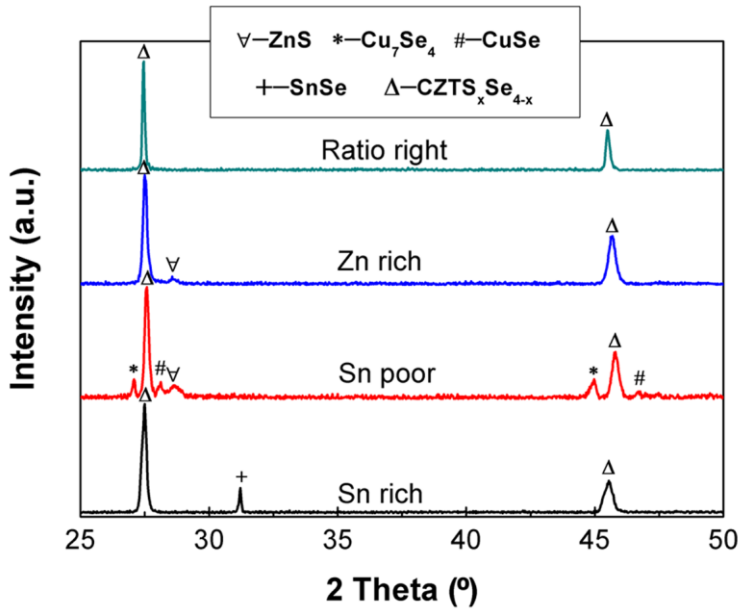

Figure 4.4 XRD patterns of Sn rich, Sn poor, Zn rich and ratio right samples.

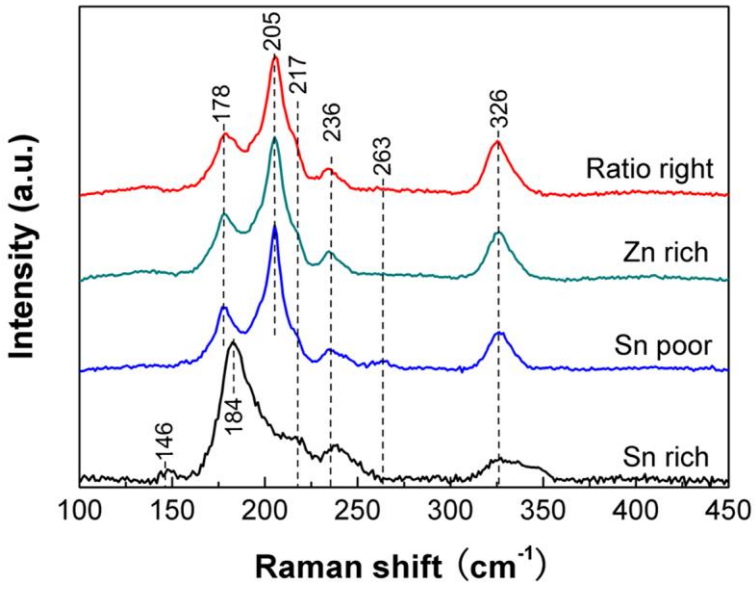

Figure 4.5 Raman patterns of the Sn rich, Sn poor, Zn rich and ratio right samples.

For Sn rich sample, some particles can be found on the surface and the EDX mappings reveal that they are Sn rich in Figure 4.3(a). In the XRD pattern of this sample, a peak belonging to SnSe phase (PDF #53-0527) at 31.2 ° can be found in Figure 4.4. Correspondingly, there is a Raman shift at about 146cm^{-1}

confirming the SnSe phase. [136, 137] Cu, Zn and Sn are evenly distributed in the film (see Figure 4.3a). Its XRD pattern shows diffractions peaks at 27.5 ° and 45.5 °, which are in between the pure CZTS (28.5 ° and 47.3 °) and CZTSe (27.1 ° and 45.0 °) phases. Its Raman shifts located at 217cm^{-1}, 236cm^{-1} and 326cm^{-1} match the reported CZTSSe phase. [138, 139] The peak at 184cm^{-1} is between the major peaks of Cu_2SnSe_3 (178cm^{-1}) and CZTSSe (206cm^{-1}).[138-140] After the analysis of EDX (see Table 4.1), XRD and Raman results, the Sn rich sample appears consisting of a major Zn poor CZTSSe phase and SnSe surface precipitations. The appearance of a solid SnSe secondary phase on the surface also indicates that the selenization conditions can effectively suppress Sn loss during annealing, because Sn loss has been known in the form of SnSe vaporization.

For the Sn poor sample, faceted Cu rich crystals are observed at the surface from both the top view and cross-section view of SEM images and EDX mappings as seen in Figure 4.3(b). Besides, Zn and S rich areas are also formed near the bottom. Its XRD curve has peaks belonging to CuSe (PDF #65-3562), Cu_7Se_4 (PDF #26-0557) and ZnS (PDF #65-0309) phases. The main part of the film is still CZTSSe phase with diffraction peaks at 27.6 ° and 45.8 °. The Raman result confirms the CZTSSe phase with peaks at 178cm^{-1}, 206 cm^{-1}, 217 cm^{-1}, 236cm^{-1} and 326cm^{-1} and the surface Cu_xSe phase with peaks around 263cm^{-1}. [137, 141] The absence of ZnS phase in Raman pattern may be resulted from the reduced focus area in the measurement or the

blocking of signals by the upper layers. Therefore, the Sn poor sample has a bulk CZTSSe layer but with Cu_xSe impurities at the top surface and ZnS phase at the bottom interface.

For the Zn rich sample, the top surface has a uniform elemental distribution without any secondary phase segregation as shown in Figure 4.3(c) top view. However, the cross-section view demonstrates a Zn and S rich area near the bottom, similar to the Sn poor sample. At the same time, the XRD and Raman results consistently support the SEM and EDX characterization by exhibiting a CZTSSe plus ZnS phase in Figures 4.4 and 4.5. It is also noted that the ZnS phase is not detected in Raman spectrum, and the reason is referred to the discussion for the Sn poor sample. The Zn rich film is made up of a dense CZTSSe layer with ZnS segregations at the bottom.

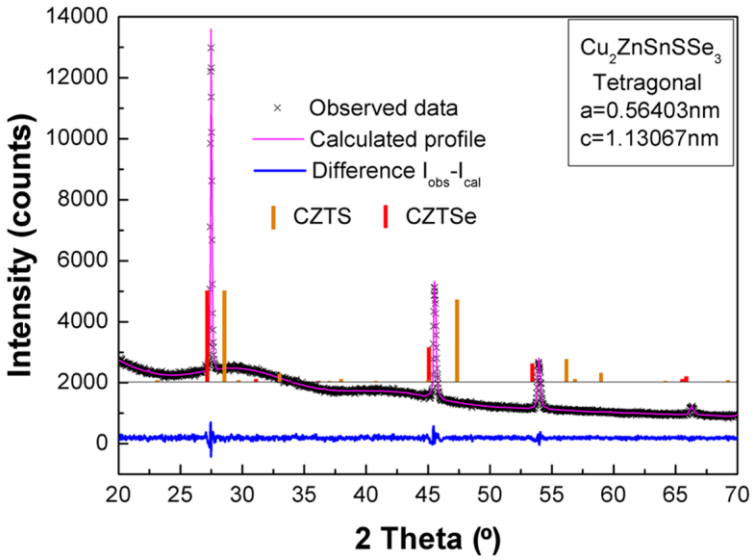

Figure 4.6 The Rietveld-refinement for the XRD pattern of the ratio right sample.

For the ratio right (near stoichiometric) sample, its relative metal ratios in Table 4.1 have little change before and after selenization, which once more indicates a negligible metal loss during annealing. No matter on the surface or along the depth, the film has uniform elemental distributions and clean front and back surfaces without any impurity phases (see Figure 4.3d). Its XRD and Raman patterns both reveal a pure CZTSSe phase in this sample. Besides, the Rietveld-refinement is applied to simulate the XRD data to check the quantitative elemental analysis by EDX as shown in Figure 4.6. [142] The diffraction data obtained from the ratio right sample is well fitted by the structure of CZTSe with 1/4 Se replaced by S, which agrees with the measured elemental ratios in Table 4.1. A tetragonal structure with lattice parameters a=0.5640nm and c=1.137nm that is just between the values of pure CZTSe (PDF #52-0868) and CZTS (PDF #26-0575) crystal lattices is also revealed by the refinement results.

Figure 4.7 shows cross-section TEM images of (a) ratio right and (b) Sn poor samples. In addition, the elemental distributions along the depth are measured by energy dispersive X-ray spectroscopy with a scanning transmission electron microscopy (STEM) mode. In Figure 4.7(a), all the elements are evenly distributed through the whole thickness with a Cu:Zn:Sn:S:Se ratio of about 2:1:1:1:3, which is consistent with the XRD refinement results in Figure 4.6. Besides, the single crystal diffraction patterns in Figure 4.7(a1) and (a2) reveal grains with different orientations of the same kesterite CZTS (PDF

#26-0575) and CZTSe (PDF #52-0868) structures. The HR-TEM images in Figure 4.7(a1h) and (a2h) show clear lattice fringes at areas I and II in the ratio right sample, and the lattice fringe values of 0.3247 and 0.5663nm correspond to (112) and (001) planes of the $CZTSSe_3$ crystal, in good agreement with the refined data of the XRD profile (see Figure 4.6). In Figure 4.7(b), the elemental analysis shows a Zn and S rich phase near the bottom (left side) of the Sn poor sample. Both the electron diffraction pattern and the lattice fringes in HR-TEM image together with relative plane indexes and spacing (see Figure 4.7b1 and b1h) demonstrate a cubic ZnS phase (PDF #65-0309). In the central part of the Sn poor sample, all the elements distribute uniformly with the ratio of Cu:Zn:Sn:S:Se around 2:1:1:1:3. Within this region, the electron diffraction pattern and HR-TEM image (see Figure 4.7b2 and b2h) of the selected area II also indicate a similar $CZTSSe_3$ structure. The increased Cu and Se signals (at the right side) in the EDX profile in Figure 4.7(b) suggests a Cu and Se rich phase formation near the top surface of the Sn poor sample. The electron diffraction pattern of area III in this region shows a CuSe phase (PDF #65-3562) with corresponding plane indexes in Figure 4.7(b3). In summary, from the detailed phase and elemental analysis on the ratio right and the Sn poor samples through electron diffraction, HR-TEM and EDX with STEM, we confirm the observations and results obtained from the SEM, XRD and Raman characterization in Figures 4.3-4.6.

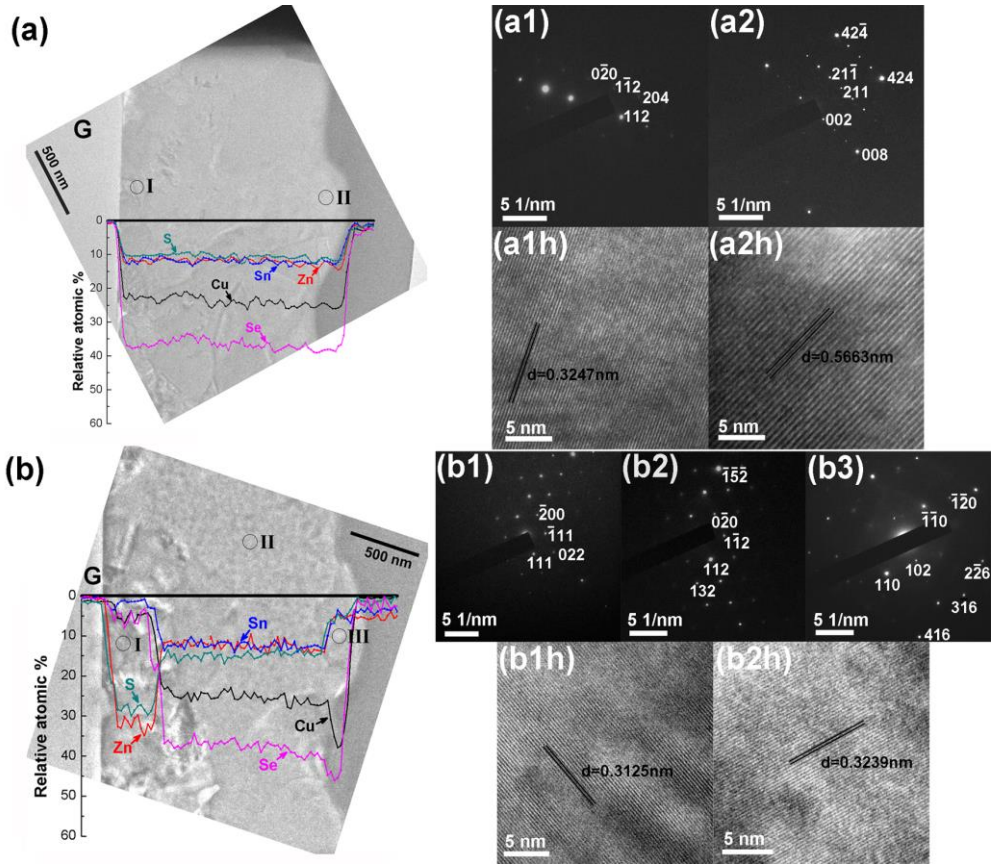

Figure 4.7 Cross-sectional TEM images (with the glass (G) substrate on the left side) and EDX elemental scans of (a) the ratio right and (b) the Sn poor samples. Electron diffraction patterns of (a1) selected area I and (a2) II in ratio right sample and (b1) I, (b2) II and (b3) III in Sn poor sample. High resolution (HR)-TEM images of area (a1h) I and (a2h) II in ratio right sample and (b1h) I and (b2h) II in Sn poor sample.

From the above results through comparing the metal ratios in the precursors (pre-Se) and the annealed samples (aft-Se) in Table 4.1, it is clear that secondary phases are easily formed during selenization if the ratio is deviated from stoichiometric in a precursor film. Once there is a secondary phase, the Cu and Sn rich phases are tend to accumulate at the front surface, but the Zn rich phases lay down at the back surface. These findings are significant in guiding the improvement of CZTSSe solar cells, as a knowledge of the locations of the secondary phases will lead to different considerations of their

removal approaches. For those top surface secondary phases, it is easier to find some chemical etching processes to remove them. [59, 143-146] For the back interface impurity, like ZnS in this case, it may be more difficult. Unfortunately, Zn rich conditions are preferred to achieve high efficient cells for the CZTS(e) system. In addition, the similarity of the phase character and some uncertainties of the quantitative elemental measurement and phase identification will make the problem even worse. To address this issue, we need to explore the phase formation mechanisms of CZTSSe, from which we may find out ways to control the secondary phases.

4.3.3 Analysis of the temperature dependent selenized near-stoichiometric samples

To find out the reaction mechanism, the selenization process of the ratio right precursor is performed at different temperatures (280 ℃, 340 ℃, 400 ℃, 460 ℃ and 520 ℃), while the annealing pressure and time remain the same for all the samples.

For the 280 ℃ annealed sample, some big particles are found embedding in a continuous layer in shown Figure 4.8(a). The particles are identified to be Cu and Se rich, and Zn and S have almost full coverage in the beneath layer. Besides, Sn is also dispersed in this continuous layer.

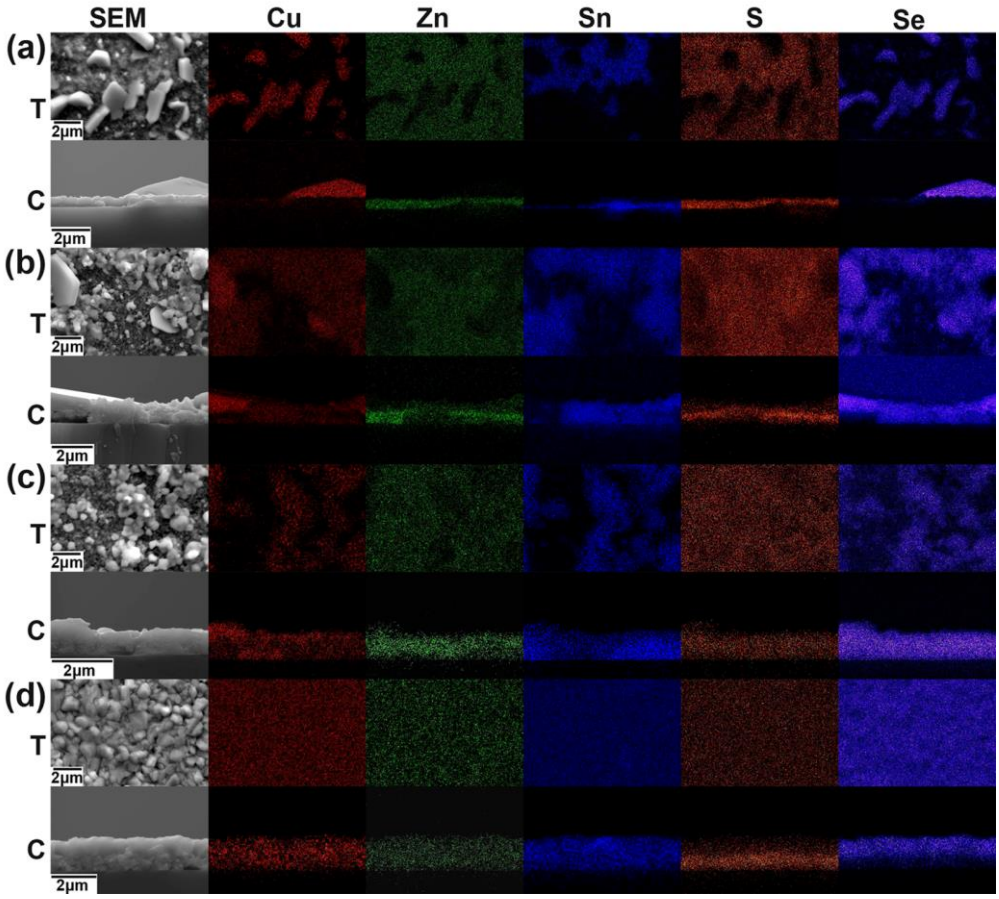

Figure 4.8 Top view and cross-section view SEM and EDX mapping of the selenized ratio right film at different temperatures of (a) 280 ℃, (b) 340 ℃, (c) 400 ℃ and (d) 460 ℃.

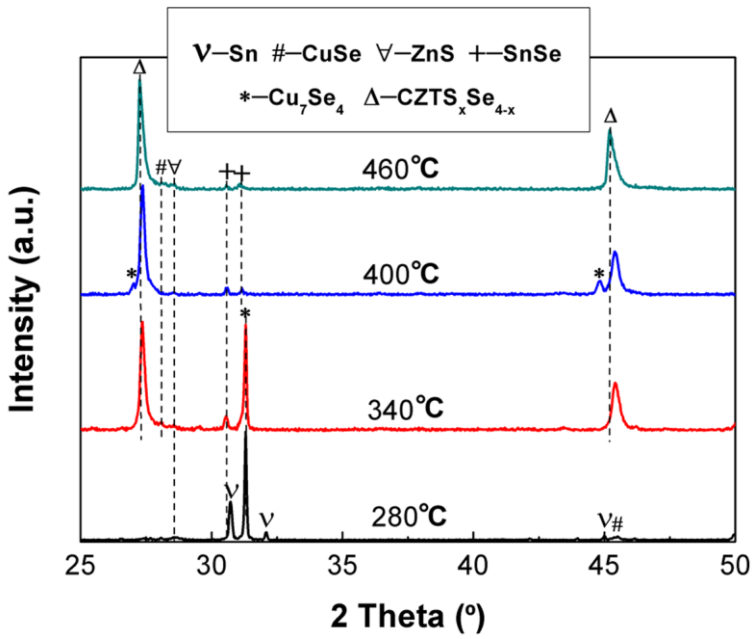

Figure 4.9 XRD patterns of the selenized ratio right film annealed at 280 ℃, 340 ℃, 400 ℃ and 460 ℃.

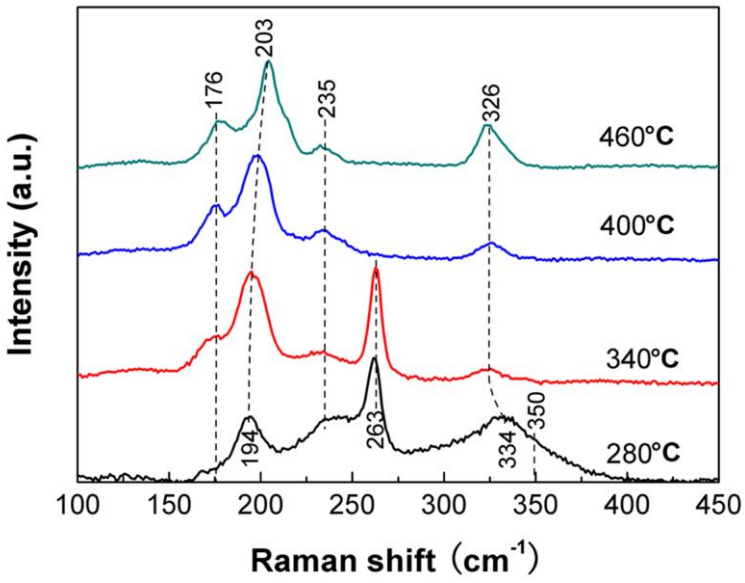

Figure 4.10 Raman spectra of the selenized ratio right precursor annealed at 280 ℃, 340 ℃, 400 ℃ and 460 ℃.

In Figure 4.9, the XRD pattern of this sample shows a strong peak at 31.3 °, which can be indexed as Cu_7Se_4 phase (PDF #26-0557). There are several peaks belonging to Sn metal phase (PDF #65-0296). Small peaks corresponding to the ZnS and CuSe phases are also observed. The phases detected match the elemental analysis quite well. Besides, its Raman spectrum (see Figure 4.10) reveals the existence of Cu_xSe phase by a strong peak located around 263cm^{-1}. And the peaks at 194cm^{-1}, 235cm^{-1} and 334cm^{-1} are hardly indexed to a specific phase, but it will be seen later that their changing trends in higher temperature samples indicate that those peaks come from the initial state of the formation of selenide/sulfide CZTSSe compound. However, these phases were not well crystallized, since it shows no clear peaks in the XRD pattern. It is also possible to have a ZnS phase peak at 350cm^{-1} in the

hump of the Raman curve. Therefore, the 280 ℃ annealed sample contains big Cu_xSe grains, certain less crystallized CZTSSe compounds and a ZnS continuous layer mixed with Sn metal phase.

For the 340 ℃ annealed sample, big Cu_xSe grains and continuous ZnS layer still appear in the sample as shown in Figure 4.8(b). Some areas covered with small grains are formed in this sample instead of a much smoother beneath layer in the 280 ℃ sample (see Figure 4.8a and b). The EDX mapping pattern of Sn remains similar to the 280 ℃ sample, but the signal for Se comes out from the same areas, demonstrating that Sn also gets selenized. And the continuous beneath layer becomes more dominant rather than a thin layer in the 280 ℃ sample in the cross-section view and there are regions containing all the Cu, Zn, Sn, S and Se signals, indicating the existence of CZTSSe phases. Unsurprisingly, its XRD pattern exhibits the peaks for CZTSSe, Cu_7Se_4, CuSe, SnSe and ZnS phases but the metal Sn phase disappears. The Raman spectrum also shows dominant peaks of the CuSe and CZTSSe phases, and the main peak for CZTSSe in this sample ($200cm^{-1}$) has a higher wavenumber than that in the 280 ℃ sample ($194cm^{-1}$). This trend will be seen to go on in the next samples till an ideal value around $205cm^{-1}$ is reached in the 520 ℃ sample (see Figure 4.5). The shift can be attributed to the increased crystal growth of CZTSSe grains and the gradual elemental adjustment during the annealing. [138, 139]

For the 400 ℃ annealed sample, the faceted big surface grains almost

disappear, but the small grains become more as shown in Figure 4.8(c) T-view. And these areas are Cu, Sn and Se rich and Zn poor, revealing Cu and Sn species are mixed together with deficient Zn species to form Zn poor CZTSSe phases near the surface. From the cross-section view, the film becomes more uniform than the lower temperature treated samples. Although the unbalanced metal elemental distributions are all through the film, much less big binary grains can be found in this sample. In the XRD pattern, the strong peak at 31.3 ℉or Cu_7Se_4 phase is not observed. Except for the dominant CZTSSe diffraction peaks, small peaks for SnSe, Cu_xSe and ZnS phases also contribute to the XRD pattern in Figure 4.9. Meanwhile, almost all the Raman shifts can be assigned to the CZTSSe phase, which suggests a limited detectable secondary phases in a reduced area. After all, the 400 ℃ sample is composed of mainly CZTSSe with certain sparsely distributed secondary phases.

For the 460 ℃ annealed sample, the film turns to be more uniform with closely packed grains around 1μm at the surface shown in Figure 4.8(d). In the cross-section view, a more uniform film can be observed, although a bulk layer near the surface and a less dense layer with smaller grains near the bottom are also detected. Similar bi-layered CZTS(e) films were also observed in some reports. [147-149] When checking the elemental mappings, the metal elements generally spread evenly in the film. However, S and Se have a layered structure that matches the SEM cross-section image. It implies that the Se rich upper layer tends to form denser and bigger grains than the beneath S

rich layer. The diffraction peaks for the CZTSSe phase in Figure 4.9 show asymmetric shapes that represent lattice derivation within the film due to the layered S and Se concentrations. Little secondary phases' peaks are detected in the XRD pattern. The Raman peaks can also be assigned to the CZTSSe phase, and the main peak at 203cm^{-1} becomes narrower and sharper suggesting an increased crystallization of the film. Thus, a bulk CZTSSe film with a thickness around 1.6μm is formed but with a clear layered S and Se dispersion in the 460 ℃ annealed sample.

The 520 ℃ annealed sample has already been discussed as the ratio right sample. A pure CZTSSe bulk film was characterized in Figures 4.3(d), 4.4 and 4.5. When tracing back the temperature dependent series, the peaks corresponding to the CZTSSe peaks in the XRD pattern move to smaller angles with a higher temperature, which is caused by the increased Se incorporation during temperature increasing. The main CZTSSe Raman peak around 200cm^{-1} undergoes a shift towards larger wavenumbers with a higher temperature, which indicates an increased S(e) incorporation into the CZTSSe system with temperature increasing. Both characterizations indicate the same phase coalescence process from two different directions as demonstrated in Figure 4.8. Han *et al.* [150] reported the crystallization behavior of CZTS samples, showing detailed phase formation procedure, i.e. starting from binary or ternary phases at lower temperature and growing to CZTS phase at a high temperature. Big CZTS crystal grains tend to firstly form near the top surface

and develop downward to the bottom, similar to our CZTSSe system. A critical temperature about 500 ℃ is needed to eliminate bi-layers and form bulk CZTS films, similar to our CZTSSe system.

4.3.4 Reaction thermodynamics analysis

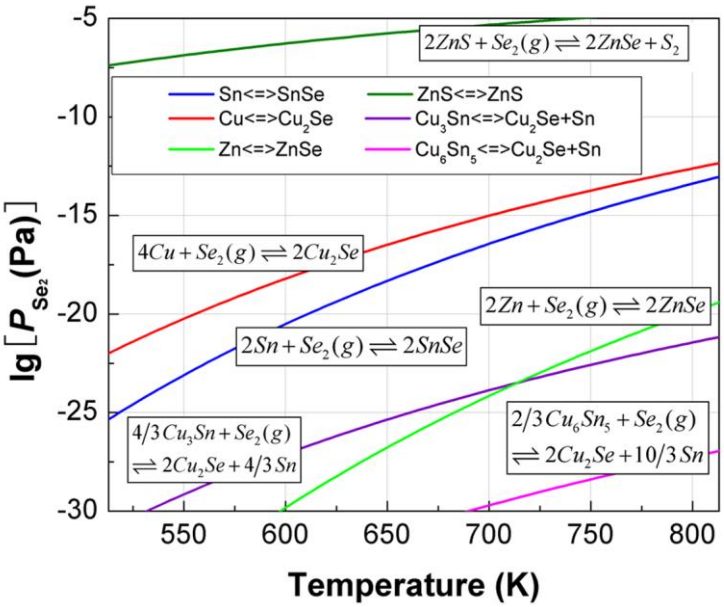

Figure 4.11 Calculated equilibrium Se_2 vapor pressure versus temperature for the selenization reactions of Cu, Sn, Zn, Cu_3Sn, Cu_6Sn_5 and ZnS.

To clarify the mechanisms behind the experimental phenomena discussed above, detailed reaction thermodynamic analysis is carried out. The equilibrium Se_2 vapor pressures during selenization reactions of Cu, Sn, Zn, Cu_3Sn, Cu_6Sn_5 and ZnS are plotted in Figure 4.11 referring to the reactions (R4-9) and corresponding Gibbs free energy changes are also listed in Table 4.2. Although the pressure-temperature curve for selenization of Zn is the lowest, the ZnSe curve that represents the substitution of S by Se in ZnS is at

the highest pressure position meaning this reaction is the most difficult one (see Figure 4.11). The experimental results also support this prediction that ZnS phase (instead of ZnSe) is always detected no matter in the lower temperature annealed ratio right sample or Zn rich samples, because Zn is already sulfurized in the precursors (see Figure 4.1b). It is also noted that Sn has a lower pressure curve than Cu, suggesting the elemental Sn should be easier to be selenized than Cu. However, Sn metal phase and Cu_xSe phases are found in the 280℃ annealed sample and SnSe phase shows up in higher temperature samples, which contradicts the thermodynamic prediction. When we check the as deposited precursor film, Cu and Sn are in the alloy forms (Cu_3Sn and Cu_6Sn_5) instead of elemental metals in Figure 4.1(b). Thus, the curves for selenization of Cu_3Sn and Cu_6Sn_5 are also represented in Figure 4.11. They lie much lower than the curves of element Cu and Sn, so it becomes reasonable to find Cu_xSe phases prior to SnSe phase in the experiments (see Figures 4.8-4.10).

In order to study the formation of phases, the equilibrium pressure curves for $SnSe_2$, Cu_2SnSe_3, CZTS and CZTSe are plotted together with Cu_2Se and ZnSe in Figure 4.12 according to the reactions R10-16 and thermodynamic calculations in Table 4.2. It should be pointed out that the experimental thermodynamic parameters for CZTS and CZTSe have not been available so far, so the calculation is based on the computer simulated values in literatures. [125, 126] Considering the possible difference of the simulated results with

the real experimental values, the curves for CZTS and CZTSe are extended to two bands, which are also calibrated by reported experimental results. [127]

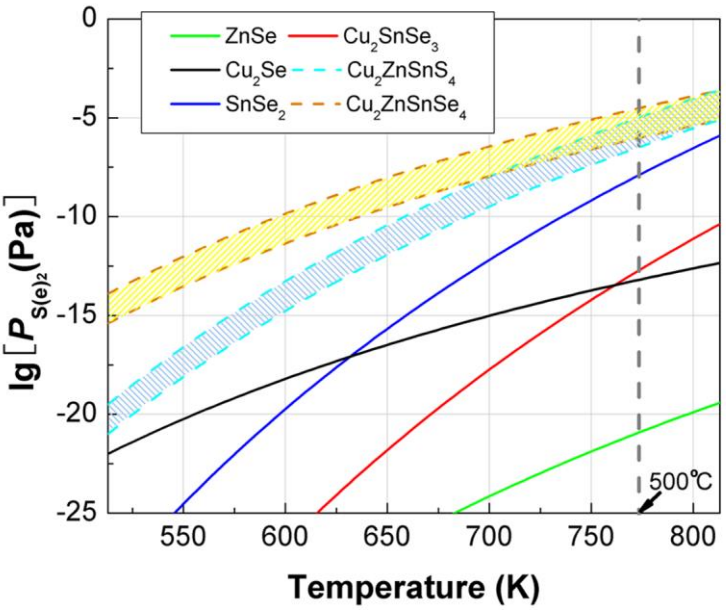

Figure 4.12 Calculated equilibrium S(e)2 vapor pressure versus temperature for the formation reactions of Cu_2Se, $SnSe_2$, ZnSe, Cu_2SnSe_3, CZTS and CZTSe.

Normally, the pressure curves for CZTS(e) are above relevant binary or ternary selenides, but these curves will approach each other with temperature increasing. At relatively lower temperatures, a mix of binary selenides could have lower total energy. With temperature increasing, they are going to combine and form CZTS(e). The temperature dependent annealing experimental results are in good agreement with this thermodynamic indication. For CZTS and CZTSe, there is a bigger difference in the equilibrium pressure at a lower temperature, and they get closer and overlap at a relatively high temperature, which can be the reason for the formation of a layered film at a relatively low temperature and a uniform film at a high

temperature. From the experimental aspect, the annealing temperature should be above 500 ℃ to achieve good quality CZTS(e) films, [123, 151, 152] which is also confirmed by the results and thermodynamic analysis in this chapter.

4.4 Conclusion

CZTSSe films with various compositions have been prepared through a co-evaporated Cu-Sn-Zn-S precursor and post selenization route, which successfully solved the Sn loss problem. Different secondary phases were detected at different locations, i.e. Cu_xSe and SnSe on the top surface and ZnS at the bottom interface. In order to explore the formation mechanism of CZTSSe film, a temperature dependent annealing study was performed on a near-stoichiometric precursor, which provides experimental observation on the phase formation procedure of CZTSSe phase. The crystal growth starts from binary metal selenides/sulfides formation, and then these grains coalesce with each other to form multi-component phases. During this process, the temperature is found playing an important role to drive the element distributions and crystal growth and an elevated temperature (normally above 500 ℃) is required to obtain a high quality CZTS(e) film. Besides, thermodynamic analysis is applied to related sulfurization and selenization reactions, which not only supports the experimental results but also leads to a better understanding of the reaction mechanisms of impurity segregation.

Chapter 5 Study on the impacts of sulfur incorporation in precursor on CZTSSe films

5.1 Introduction

In the previous chapter, the influences of metal ratios in precursor films on the film growth, especially secondary phase segregation, were studied. In this chapter, the effects of sulfur incorporation into the precursor films on the CZTSSe films will be explored. Growth models are proposed to demonstrate the film formation mechanisms based on the temperature dependent selenization studies of the sulfur free and sulfur contained precursors. In contrast to the sulfur free precursor, the sulfur incorporated precursor is surprisingly found to result in a significantly thinner $Mo(S,Se)_2$ layer and an improved interface between the CZTSSe layer and Mo substrate. Experimental evidences on film adhesion and mechanical properties of CZTSSe films are also provided. A dramatically enhanced film adhesion and elastic modulus values close to the simulation results from the literature are achieved in the sulfur incorporated sample. The relationships between the precursor adjustments, interfacial structures and mechanical performances of the CZTSSe films are also revealed in this chapter.

5.2 Experimental details

$Cu_2ZnSnSe_4$ (CZTSe) and $Cu_2ZnSn(S,Se)_4$ films were prepared on Mo-coated glasses through a thermal co-evaporation and post-selenization route. Although different preparation conditions of the Mo substrate can affect the absorber layers and their interfaces, it is still the most widely used substrate in the CIGS and CZTS based solar cells. In addition, studies of the CZTS based absorber layers are emphasized in this work and in order to eliminate the possible impacts of the substrates and to make the experimental conditions for the CZTS based layers comparable, the commercial Mo coated glass was selected as the substrate. Two precursor films with different sulfur contents were obtained by using two different sets of sources, i.e. Cu+Sn+Zn and Cu+Sn+ZnS. For each precursor film, stoichiometric ratios of metallic elements were obtained by controlling the temperature of each source. These two precursors were selenized in one container at different annealing temperatures of 280 ℃, 340 ℃, 460 ℃, 520 ℃, 580 ℃, 630 ℃ and 680 ℃. Besides, considering the possible variations of the properties of absorber layers and their interfaces with the Mo substrates resulted from different Se amounts in the annealing atmosphere, the same amount of Se (8mg) was used in each annealing batch. Further studies on the 580 ℃ selenized sulfur free (S_0) and sulfur contained (S_1) samples were carried out to reveal their interfacial differences and mechanical performances.

5.3 Results and discussion

5.3.1 Characterization of the precursor films

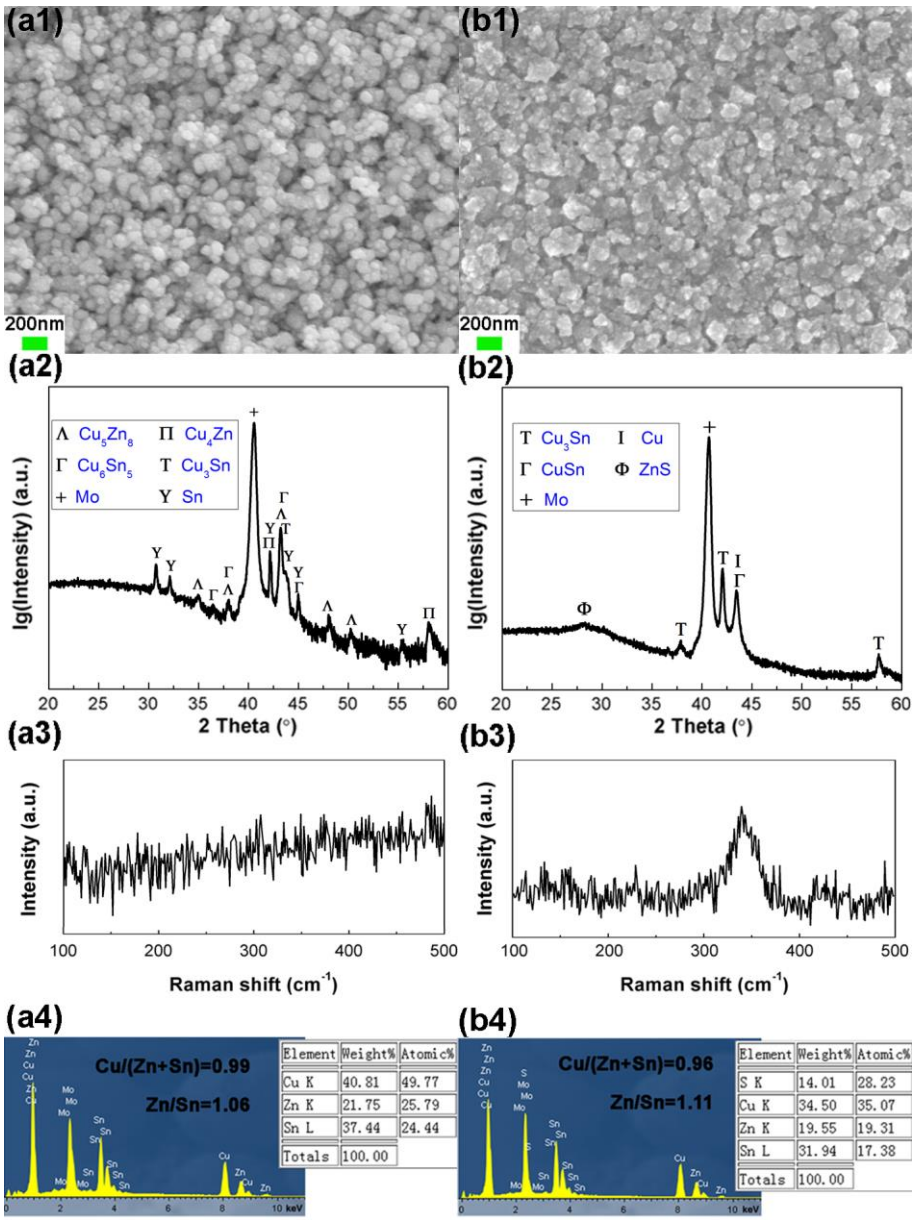

Figure 5.1 (a1) and (b1) SEM images, (a2) and (b2) XRD patterns, (a3) and (b3) Raman patterns and (a4) and (b4) EDX analysis of the sulfur free and sulfur contained precursor films, respectively.

The surface morphologies of the sulfur free and sulfur contained precursor films are presented in Figure 5.1(a1) and (b1). A uniform surface consisting of

distinct sphere-like particles is characterized for the sulfur free precursor film. While the sulfur contained precursor exhibits a more compact surface constructed by agglomerated particles, which might be due to the reduced crystallinity resulted from sulfur incorporation.

The XRD patterns of these two precursors are shown in Figure 5.1(a2) and (b2). In addition to the peak belonging to the Mo substrate, metallic peaks refer to the phases of Cu_3Sn (PDF #01-1240), Cu_6Sn_5 (PDF #45-1488), Cu_5Zn_8 (PDF #25-1228 and 41-1435) and Sn (PDF #65-7657 and 65-2631) are detected in the sulfur free precursor film in Figure 5.1(a2). For the sulfur contained precursor, diffraction peaks from the metallic Cu_3Sn (PDF #01-1240 and 65-4653), CuSn (PDF #06-0621 and 44-1477) and Cu (PDF #65-9743) phases and a broad hump representing a possible ZnS phase (PDF #65-1691) are observed in Figure 5.1(b2). In Figure 5.1(a3), there is no characteristic Raman shift peak in the sulfur free precursor. But a broad peak at about 340cm^{-1} is detected in Figure 5.1(b3) indicating the existence of certain sulfide compound in the sulfur contained precursor. The elemental compositions of these two precursors are analyzed by EDX in Figure 5.1(a4) and (b4). The relevant metal ratios of Cu/(Zn+Sn) and Zn/Sn are 0.99 and 1.06 in the sulfur free precursor and 0.96 and 1.11 in sulfur contained precursor, which are near the stoichiometry for the CZTS(e) phase.

5.3.2 Temperature dependent selenization of the sulfur free precursor

The top view SEM images, XRD patterns, Raman patterns and cross-section view SEM images with EDX elemental mappings of the selenized samples at annealing temperatures of 280 ℃, 340 ℃, 460 ℃, 520 ℃, 580 ℃ and 630 ℃ for the sulfur free precursors are presented in Figures 5.2-5.4, respectively.

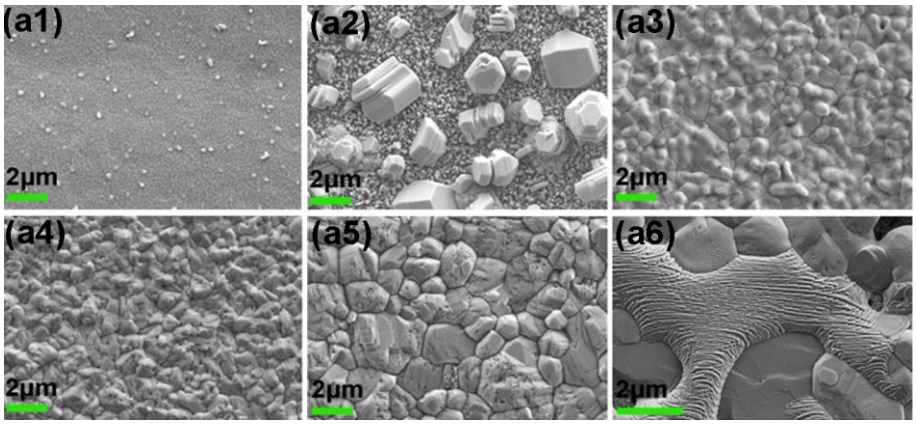

Figure 5.2 Top-view SEM images of annealed samples after selenization at (a1) 280 ℃, (a2) 340 ℃, (a3) 460 ℃, (a4) 520 ℃, (a5) 580 ℃ and (a6) 630 ℃ for the sulfur free precursor, respectively.

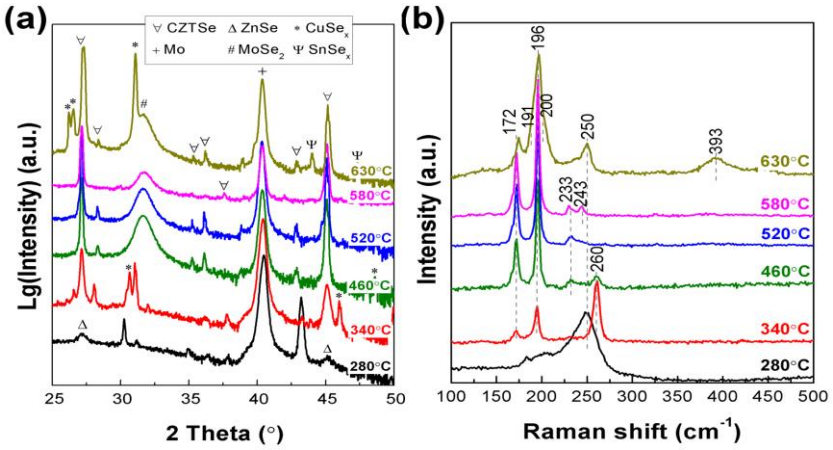

Figure 5.3 (a) XRD and (b) Raman patterns of the annealed sulfur free sample at 280 ℃, 340 ℃, 460 ℃, 520 ℃, 580 ℃ and 630 ℃.

For the sample annealed at 280 ℃, some randomly distributed grains are found on the surface in Figure 5.2(a1). In Figure 5.3(a), in addition to the diffraction peaks referring to the metallic phases in its precursor and Mo substrate, the peak around 27.1 ° indicates a CZTSe, Cu_2SnSe_3 or ZnSe phase. Furthermore, its Raman shift peak at 250cm^{-1} suggests a ZnSe phase in Figure 5.3(b). [153] Accordingly, the elemental mappings in Figure 5.4(a) also reveal a Zn and Se rich region in the top layer, which, together with the XRD and Raman results, confirms that Zn is selenized to form a ZnSe layer near the surface at 280 ℃.

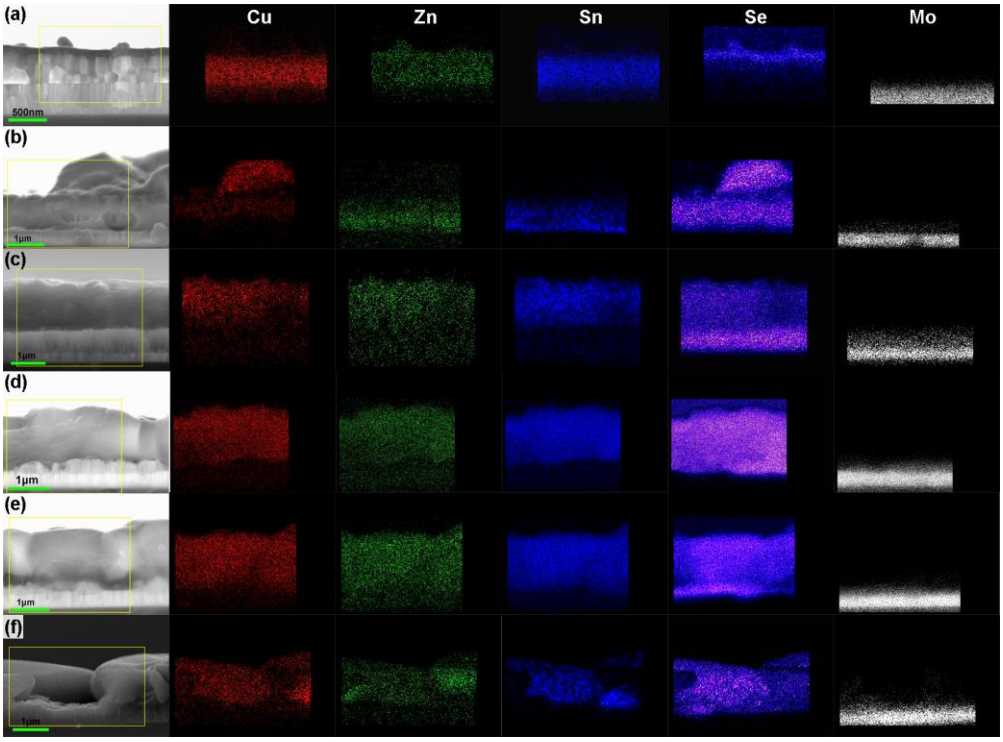

Figure 5.4 Cross-section view SEM images and EDX mappings of the annealed sulfur free samples at (a) 280 ℃, (b) 340 ℃, (c) 460 ℃, (d) 520 ℃, (e) 580 ℃ and (f) 630 ℃.

For the sample annealed at 340 ℃, big faceted grains with size over several micrometers appear on the surface in Figure 5.2(a2). In Figure 5.3(a), the

diffraction peaks around 26.6 °, 30.6 °, 31.1 ° and 46.0 ° can be indexed to the $CuSe_x$ phases (PDF #06-0680, 20-1020 and 27-0184) and the peaks at 27.1 °, 28.1 ° and 45.1 ° belong to a possible CZTSe, Cu_2SnS_3 or ZnSe phase. In addition, other small peaks from the metallic precursor still remain in this sample. The existence of the $CuSe_x$ phases is also indicated by its Raman shift peak at 260cm^{-1} in Figure 5.3(b). [154, 155] Besides, the extra peaks at 172cm^{-1} and 196cm^{-1} demonstrate a CZTSe phase. [156] By viewing the elemental mappings across the depth of the sample in Figure 5.4(b), it is found that the big gains are Cu and Se rich. There are also areas consist of Cu, Zn Sn and Se, indicating the CZTSe phase as suggested by the XRD and Raman analysis, even though the metal elements are not very uniformly distributed. Therefore, together with those unselenized metallic phases, big $CuSe_x$ grains are formed on the surface and the CZTSe phase also starts to appear in the sample annealed at 340 ℃.

For the sample annealed at 460 ℃, a much more uniform surface without big $CuSe_x$ grains is observed in Figure 5.2(a3). Besides the minor XRD peaks at 48.6 ° representing the $CuSe_x$ phase in Figure 5.3(a), the peaks at 27.1 °, 28.1 ° 35.3 °, 36.2 °, 42.8 ° and 45.1 ° belongs to the CZTSe phase. In addition, a broad peak around 31.7 ° reveals a $MoSe_2$ phase (PDF #20-0705). Accordingly, Raman shift peaks for the CZTSe phase at 172cm^{-1}, 196cm^{-1} and 233cm^{-1} are detected in Figure 5.3(b). The peak at 260 cm^{-1} is much reduced in contrast to the sample annealed at 340 ℃, which comes to the same conclusion that the

$CuSe_x$ phase is much reduced as the XRD and SEM suggested. In Figure 5.4(c), a bulk film with EXD mapping signals of Cu, Zn, Sn and Se is detected, which indicates the formation of CZTSe phase. At the same time, a Se and Mo rich layer is formed between the CZTSe layer and the Mo substrate, representing the $MoSe_2$ phase revealed by XRD in Figure 5.3(a). Combining all these analysis, we can conclude that the CZTSe phase becomes dominant in the sample annealed at 460 ℃, and an additional $MoSe_2$ layer is formed at the back contact interface.

For the sample annealed at 520 ℃, a uniform surface without secondary phase grains is shown in Figure 5.2(a4). Its XRD pattern shows a combination of CZTSe, $MoSe_2$ and Mo phases in Figure 5.3(a). In Figure 5.3(b), a CZTSe phase is also detected by Raman. The cross-section view SEM and elemental mappings in Figure 5.4(d) just support the results obtained by XRD and Raman. It is noted that there is no detectable secondary phases in this sample compared with the sample annealed at 460 ℃.

For the sample annealed at 580 ℃, the SEM image in Figure 5.2(a5) shows bigger CZTSe grains than the sample annealed at 520 ℃. The XRD, Raman, and cross-section view SEM and EDX mappings (see Figures 5.3 and 5.4e) give similar phase identification with the sample annealed at 520 ℃. Meanwhile, the degenerated $MoSe_2$ layer and voids make the back interface even more blurred.

For the sample annealed at 630 ℃, a decomposed surface with different

characteristic phases is observed in Figure 5.2(a6). Meanwhile, the diffraction peaks representing the $CuSe_x$ phases at 26.3°, 26.6° and 31.1°, the CZTSe, Cu_2SnSe_3 or ZnSe phase around 27.2°, 28.1° and 45.2°and the $SnSe_x$ phases (PDF #23-0602) around 44.1° and 47.5°can be addressed in Figure 5.3(a). A broad peak around 31.7° for $MoSe_2$ and the peak at 40.5° for Mo are also detected. In Figure 5.3(b), the Raman shift peaks at 174cm^{-1} and 196cm^{-1} are from the CZTSe phase. The broad peak at about 200cm^{-1} can be attributed from $CuSe_x$ phases. [157] And the peaks around 191cm^{-1} and 250cm^{-1} are from $SnSe_x$ and ZnSe phases, respectively. [158] The peak appears around 393cm^{-1} is resulted from the $MoSe_2$ phase. [159] Moreover, the elemental mappings in Figure 5.4(f) reveal different areas in the film containing Cu, Sn or Zn rich compositions, which are consistent with the XRD and Raman results.

5.3.3 Temperature dependent selenization of the sulfur contained precursor

The top view SEM images, XRD patterns, Raman patterns and cross-section view SEM images with EDX elemental mappings of the selenized samples at annealing temperatures of 280℃, 340℃, 460℃, 520℃, 580℃, 630℃ and 680℃ for the sulfur contained precursors are presented in Figures 5.5-5.7, respectively.

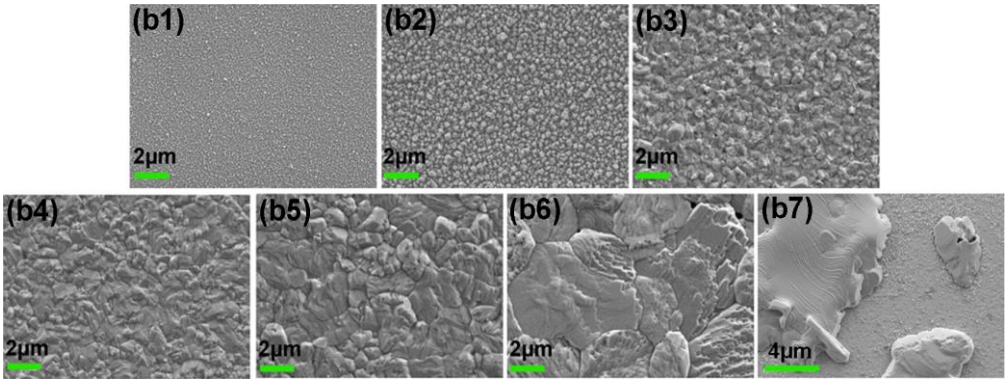

Figure 5.5 Top-view SEM images of annealed samples after selenization at (b1) 280 ℃, (b2) 340 ℃, (b3) 460 ℃, (b4) 520 ℃, (b5) 580 ℃ and (b6) 630 ℃ and (b7) 680 ℃ for the sulfur contained precursor, respectively.

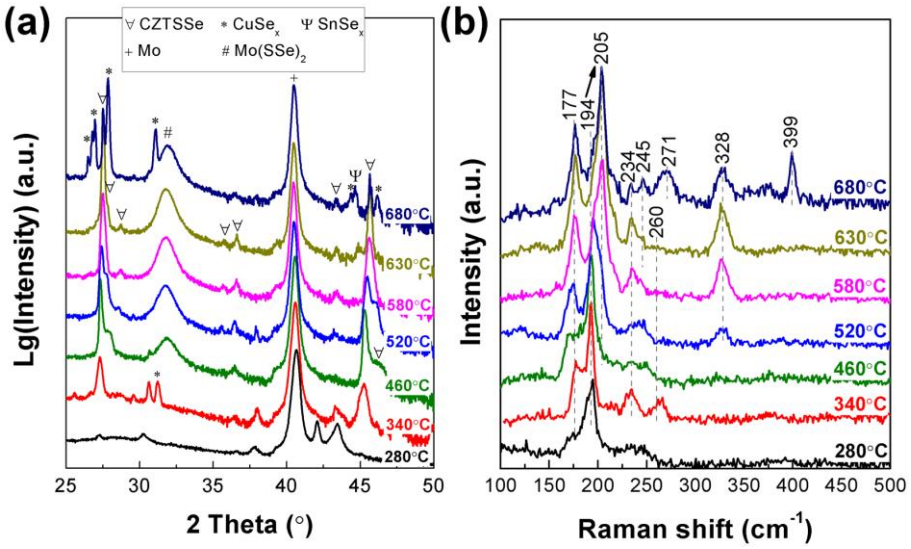

Figure 5.6 (a) XRD and (b) Raman patterns of the annealed sulfur contained sample at 280 ℃, 340 ℃, 460 ℃, 520 ℃, 580 ℃, 630 ℃ and 680 ℃.

For the sample annealed at 280 ℃, the XRD pattern in Figure 5.6(a) shows similar peaks as in its precursor, except for a small peak around 27.2 ° representing a selenized phase. The Raman shift with peaks at 194 cm^{-1} and 245cm^{-1} in Figure 5.6(b) and a thin Se rich layer revealed by the EDX mappings in Figure 5.7(a) also suggest a selenide top layer formation. [27] It

should be pointed out that the energy positions for the element S and Mo are very close in EDX analysis, so there are always similar EDX mapping singles for these two elements. To address this issue, secondary ion mass spectroscopy (SIMS) will be introduced later to distinguish S and Mo.

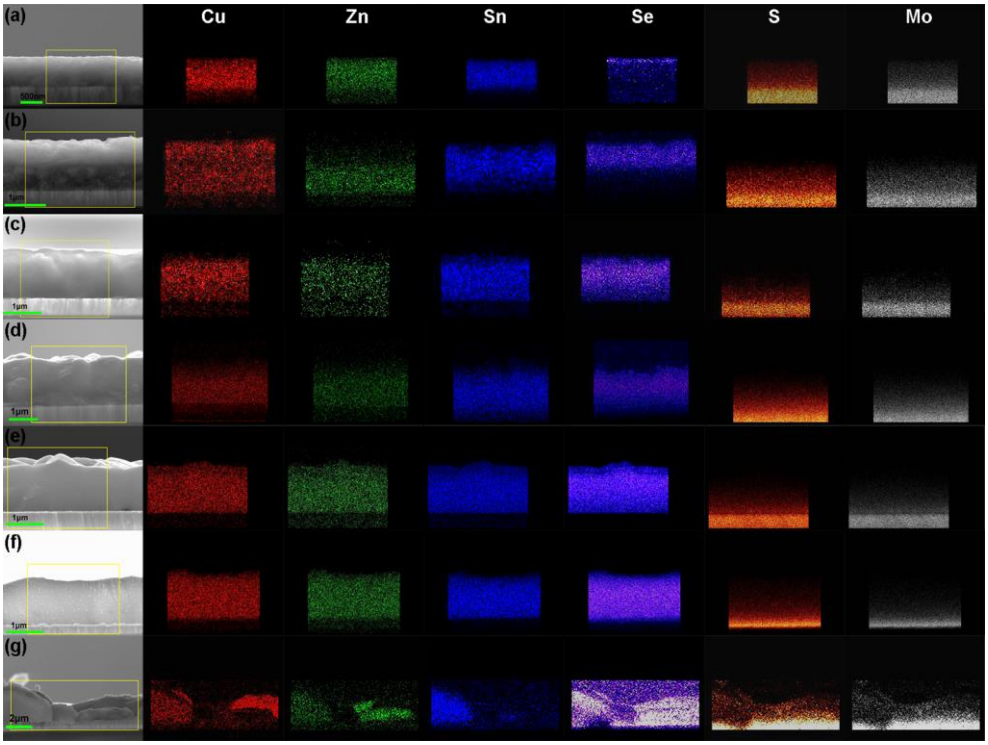

Figure 5.7 Cross-section view SEM images and EDX mappings of the annealed sulfur free samples at (a) 280 ℃, (b) 340 ℃, (c) 460 ℃, (d) 520 ℃, (e) 580 ℃, (f) 630 ℃ and (g) 680 ℃.

For the sample annealed at 340 ℃, the surface grains in Figure 5.5(b2) grow bigger than the sample annealed at 280 ℃ in Figure 5.5(b1). Dramatically increased signals for the CZTSSe phase are detected by XRD with diffraction peaks at 27.3 ° and 45.3 ° and Raman with peaks at 177cm^{-1}, 194cm^{-1} and 234cm^{-1} in Figure 5.6. In the XRD pattern, there is also a hump around 28.5 ° indicating an S rich phase. In addition, small XRD peaks at 30.5 °, 31.2 ° and

47.5° and a Raman shift peak around 260cm^{-1} suggest the existence of $CuSe_x$ phases. In Figure 5.7(b), a layered structure with a Cu, Sn and Se rich top layer and a Zn and S rich beneath layer is characterized by the cross-section view SEM images and EDX elemental mappings.

For the sample annealed at 460℃, the surface grain size further increases as shown in Figure 5.5(b3). In Figure 5.6(a), the XRD peaks around 27.3° and 45.3° referring to the Se rich CZTSSe phase and the humps around 28.0° and 46.4° referring to the S rich CZTSSe phase approach each other, demonstrating a coalescent occurred between these two layers. And the XRD peak for the phase of $Mo(SSe)_2$ around 31.8° is also detected. In Figure 5.7(c), the distributions of metal elements in the film become more uniform and the Se rich region goes deeper into the surface when comparing with the 340℃ annealed sample.

For the sample annealed at 520℃, the grain growth and recombination of Se and S rich layers continue. The XRD and Raman peak positions corresponding to the Se rich phases move towards larger values, which indicate more sulfur incorporation into the Se rich layers. In Figure 5.7(e), the metal elements are uniformly distributed through the film and the Se also penetrates deeper into the surface in contrast to the lower temperature annealed samples.

For the samples annealed at 580℃ and 630℃, much bigger grains are observed in Figure 5.5(b5) and (b6). In the XRD patterns of Figure 5.6(a), the Se rich and S rich peaks combine together to form single peaks at 27.5° and

45.7°, which can be indexed to the $Cu_2ZnSn(S_xSe_{1-x})_4$ phase with $x \approx 0.25$ according to literature. [27] Furthermore, the Raman shift peaks at 177cm^{-1}, 204cm^{-1}, 234cm^{-1}, 245cm^{-1} and 328cm^{-1} in Figure 5.6(b) also belong to the CZTSSe phase, in good agreement with the XRD results. In Figure 5.7(e) and (f), bulk CZTSSe layers with uniform elemental distributions are also characterized.

For the sample annealed at 680℃, a decomposed film is observed in Figure 5.5(b7). And its XRD and Raman results also reveal degraded secondary selenide and sulfide phases as shown in Figures 5.6. In addition, different metal element rich areas are found over its cross-section, confirming the film degradation as characterized by XRD and Raman.

5.3.4 Interfacial characterization of the annealed samples from different precursors

From above analysis, the samples annealed at 580℃ from both sulfur free (S_0) and sulfur contained (S_I) precursors exhibit bulk CZTSe and CZTSSe layers with good phase consistence and elemental uniformity, so they are chosen to perform more detailed characterizations to explore the influences of the sulfur incorporation in precursor on the interface and mechanical properties.

TEM and SAED analysis are carried out on the interfaces of S_0 and S_I as shown in Figure 5.8. The TEM images in Figure 5.8(a_L) and (b_L) manifest

interface characteristics consistent with the SEM images in Figure 5.4(e) and Figure 5.7(e). In Figure 5.8(a_H), clear lattice fringes with a spacing value of 0.509nm are observed near the bottom of the figure, which corresponds to the (101) plane of the CZTSe phase (PDF #52-0868). The fringes near the top area in Figure 5.8(a_H) have a spacing value of 0.647nm, corresponding to the (002) plane of a hexagonal $MoSe_2$ phase (PDF #77-1715). Taking SAED of the circled region in Figure 5.8(a_L), the diffraction rings as shown in Figure 5.8(a_D) can be indexed to the (002), (100) and (103) planes of the same $MoSe_2$ phase, demonstrating that this $MoSe_2$ layer is polycrystalline in nature.

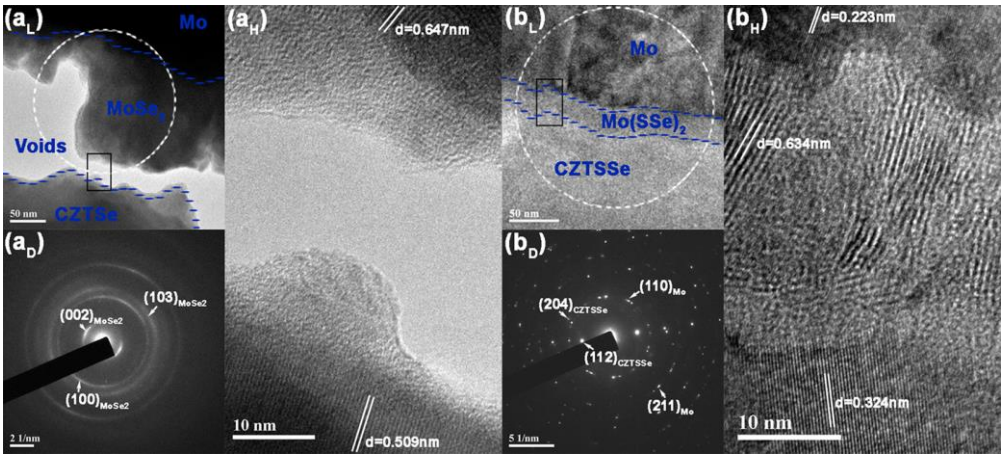

Figure 5.8 Low magnification TEM images of the back contact interface of (a_L) S_0 and (b_L) S_I, SAED patterns of (a_D) S_0 and (b_D) S_I from the circled areas in (a_L) and (b_L) and HR-TEM images of the areas in (a_H) S_0 and (b_H) S_I selected rectangle regions in (a_L) and (b_L), respectively. Areas representing Mo, CZTSe/CZTSSe and their interfaces are also indicated in (a_L) and (b_L).

In Figure 5.8(b_H), the lattice fringes near the top can be matched to Mo (PDF #89-5156) with a (110) plane spacing of 0.223nm. In the middle, a spacing value of 0.634nm is detected. This value lies in between the (002) plane

spacing values of the $MoSe_2$ phase (0.646nm) and the MoS_2 phase (0.615nm, PDF #77-1716), suggesting a sulfur incorporated $MoSe_2$ phase within this layer. Similarly, a smaller fringe spacing value (0.324nm) near the bottom of the image compared to the (112) plane spacing (0.328nm) of the CZTSe phase indicates a hybrid CZTSSe phase due to sulfur incorporation. The SAED pattern of the circled region in Figure 5.8(b_L) contains single crystal diffraction dots of the CZTSSe phase and polycrystalline diffraction rings for the Mo substrate as shown in Figure 5.8(b_D). Due to the much smaller amount and poorer crystal quality of the $Mo(S,Se)_2$ layer compared to the CZTSSe and Mo layers in the selected area, no obvious diffraction signals for the $Mo(S,Se)_2$ phase were detected. In summary, the formation of a loose interface with a large void area and relatively thick $MoSe_2$ layer (around 200nm) in S_0 and a compact interface with a much thinner $Mo(S,Se)_2$ layer (around 25nm) in S_I can be confirmed.

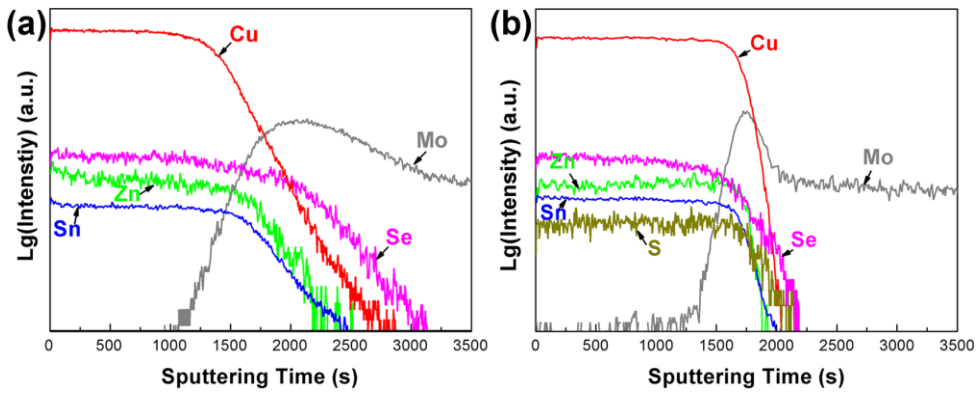

Figure 5.9 SIMS elemental profiles of (a) S_0 and (b) S_I.

The distribution of each element with respect to the sputtering time for S_0 and

S_I are characterized by SIMS and shown in Figure 5.9(a) and (b). Flat elemental profiles are observed across the CZTSe and CZTSSe layers for S_0 and S_I accordingly. However, near the back contact interfaces, the curves for the elements of CZTSe in S_0 show relatively gradual decrease in Figure 5.9(a), in contrast to much sharper drops in Figure 5.9(b) for S_I, which are plausible when considering the interfacial characteristics revealed by SEM and TEM. In addition, a simultaneous change of S with other elements in the CZTSSe phase is detected. Meanwhile, an increased profiling signal for Mo starting from the back interface in Figure 5.9(b) just distinguishes Mo and S, which are mixed together in the EDX mappings.

5.3.5 Selenization models of the CZTSSe films from different precursors

According to the temperature dependent analysis on the phase and elemental distribution changes during the film formation from the sulfur free and sulfur contained precursors, growth models are proposed to demonstrate major steps in the film formation procedure for both cases in Figure 5.10. In Figure 5.10(a1) and (b1), two different precursors are placed in a Se contained atmosphere. At lower annealing temperature, Zn element moves upward to form a ZnSe layer on the top of the sulfur free sample (see Figure 5.10a2). The smaller Se vapor pressure for the selenization of Zn in contrast to other

metallic or alloy species drives this reaction, which is discussed in Chapter 4. Meanwhile, for the sulfur contained precursor in Figure 5.10(b2), a Se rich CZTSSe layer is formed and the metal ions migration across the film is much suppressed, since they are already bonded with sulfur in the original precursor.

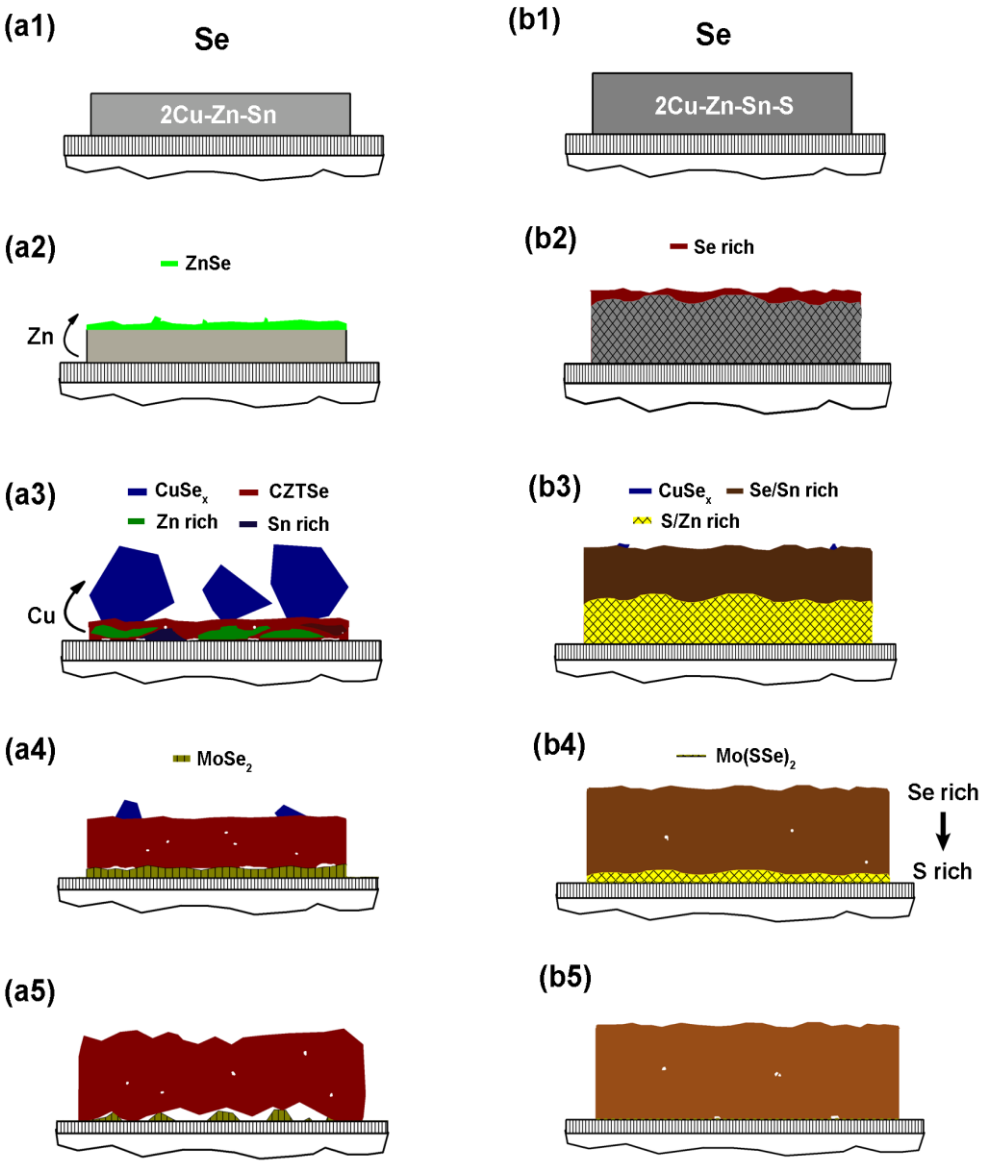

Figure 5.10 Diagrammatic sketches of the CZTSe and CZTSSe film formation mechanisms from the (a1-5) sulfur free and (b1-5) sulfur contained precursors.

When the temperature increases, intense Cu ion movements towards the film surface occur and big $CuSe_x$ grains are formed as shown in Figure 5.10(a3).

Phases consisting of Cu, Sn, Zn and Se with various composition ratios also start to grow in the layer under the big $CuSe_x$ grains. Drastic metal ion transport and exchange with Se across the entire film can result in some voids formation and generate easy access of Se to the Mo substrate, which will lead to a severe voids and $MoSe_2$ layer formation. However, for the sulfur contained sample in Figure 5.10(b3), Se penetrates deeper into the film to form a thicker Se rich layer, and at the same time due to the deficient S content in the original precursor film, small $CuSe_x$ grains can be detected on the surface and certain metal ion re-distribution also undergoes to make the upper Se rich layer also Sn rich and the beneath S rich layer with more Zn. Even though, the film growth generally develops through a layer propagation mode that allows gradual Se penetration to coalesce with the S rich layer. The Zn and S rich layer can act as a block in the path of Se moving towards Mo substrate, because the equivalent Se vapor pressure for the substitution of sulfur in Zn/S rich phase with selenium is relatively high as revealed in Chapter 4. In Figure 5.10(a4), when the annealing temperature enhances, the metal elements diffuse and different phases merge with each other that reduce the binary phases and generate a dominant CZTSe layer with more uniform elemental distribution for the sulfur free sample. Besides, significant substrate corrosion appears at the back contact interface, where a thick $MoSe_2$ layer formed together with a large amount of voids. Comparatively, in the sulfur contained sample, Se rich layer expands downward and mixes with the S rich

layer further to form a hybrid CZTSSe film. Although no obvious $Mo(SSe)_2$ layer was observed by SEM and EDX mapping, the XRD and TEM results indicated that a thin $Mo(SSe)_2$ layer is also formed at the back contact interface for the S contained sample. Finally, a bulk and uniform CZTSe or CZTSSe layer growth can be achieved at an elevated temperature (~500 ℃). Nevertheless, because of the unique formation procedure for each precursor discussed above, tremendously microstructural differences near the back contact interfaces are produced accordingly (see Figure 5.8a5 and b5).

5.3.6 Mechanical performances of the annealed samples from different precursors

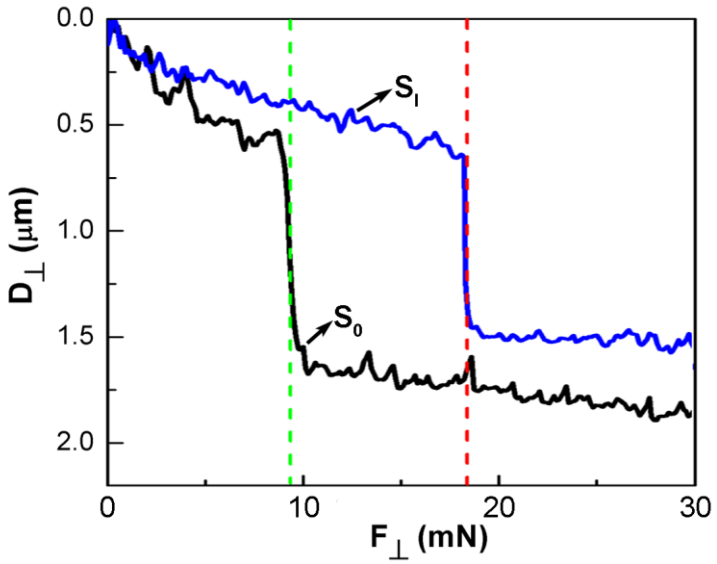

Figure 5.11 Profiles of displacement into surface ($D_\perp$) versus normal load ($F_\perp$) of S_0 and S_I.

By nano-scratch test, the profiles of displacement into surface ($D_\perp$) with

respect to normal load ($F_{\perp}$) for S_0 and S_I are plotted in Figure 5.11. The $D_{\perp}$ value after the dramatic drop is just around the film thickness for each sample, suggesting that a film failure occurs near the film and substrate interface. [102] The critical normal load (F_C) values for S_0 and S_I are recorded in Table 5.1, which can be used to evaluate the film adhesion performance. [104] The F_C value of 9.2mN for sample S_0 is much smaller than that of 17.2mN for sample S_I, indicating poorer film adhesion properties in sample S_0 than S_I. It is noted that poor adhesion also appeared in the CIGS films prepared from metallic precursors. [160, 161]

Table 5.1 Interface thickness (T_i), critical scratch load (F_C), maximum indentation load (P_m), residual depth (h_r), intercept depth (h_p), hardness and elastic modulus from loading (H_L and E_L) and unloading (H_U and E_U) curves for samples S_0 and S_I. The modulus values are calculated under plain strain condition. The simulated modulus (E_S) values in literature are also listed for comparison. [6, 81, 162]

Samples	T_i/nm	F_C/mN	P_m/mN	h_r/nm	h_p/nm	H_L/GPa	H_U/GPa	E_L/GPa	E_U/GPa	E_S/GPa
S_0 (CZTSe)	~200	9.2	20.8	875.7	927.4	0.8	1.0	41.5	48.6	82.1, 71.5, and 77.8
S_I (CZTSSe)	~25	17.2	69.3	682.5	838.7	3.4	4.0	76.2	86.4	85.6 and 79.2

To study the elastic modulus (E) and hardness (H) of samples S_0 and S_I, their nano-indentation loading and unloading curves are measured and shown in Figure 5.12(a1) and (b1). A typical elastic-plastic loading curve is observed in sample S_I. In contrast, a plastic-like behavior appears at the initial stage of the loading curve for S_0, and the larger residual depth (h_r) detected in the

unloading curve for S_0 than S_I also demonstrates that more plastic deformation occurred in S_0 than in S_I during the indentation measurement. [104]

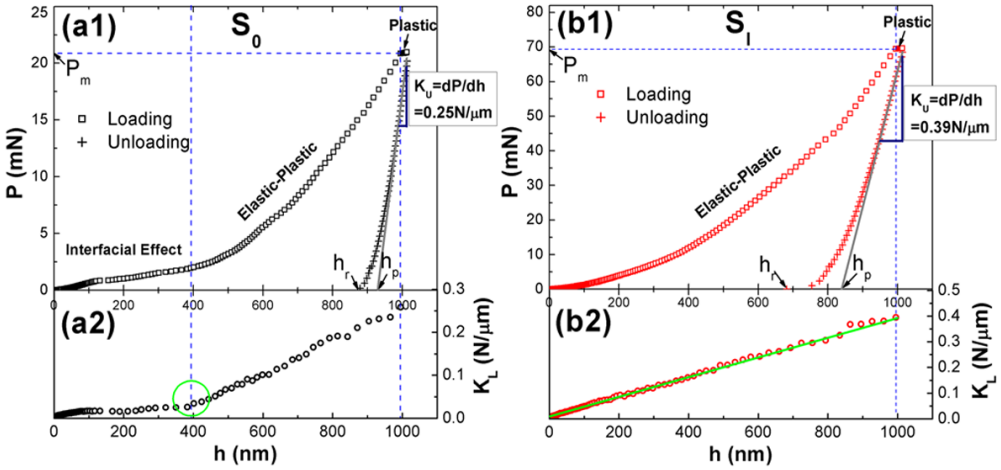

Figure 5.12 Load force (P) as a function of indentation depth (h) during loading and unloading tests for (a1) S_0 and (b1) S_I. Characteristic parameters, such as maximum load (P_m), residual depth (h_r), intercept depth (h_p) and stiffness determined from unloading curves (K_U) are indicated in (a1) and (b1). Contact stiffness determined from loading curves (K_L) with respect to indentation depth (h) for (a2) S_0 and (b2) S_I.

Considering the diamond Berkovich-type indenter and the plain strain condition applied in this work, H and E can be expressed as [104, 163]

$$H = \frac{P_m}{A} = \frac{P_m}{24.5h_p^{\,2}} \tag{5-1}$$

$$E = \frac{2K}{\beta}\sqrt{\frac{\pi}{A}} = \frac{2K}{1.034h_p}\sqrt{\frac{\pi}{24.5}} \tag{5-2}$$

where P_m and h_p are the maximum indentation load and the intercept depth as pointed out in Figure 5.12(a1) and (b1). A and β are the contact area and the geometry constant, equaling $24.5h_p^{\,2}$ and 1.034 in this case, respectively. K is the stiffness that describes the deformation resistance of an object in response

to an applied force. The values of stiffness for S_0 and S_I are determined either from the initial stage of their unloading curves (K_U) (see Figure 5.12a1 and b1) [106] or from the loading curve (K_L) through a continuous stiffness measurement technique [163]. The variations of K_L in response to indentation depth h for S_0 and S_I are shown in Figure 5.12(a2) and (b2). The larger K_L values measured along the whole indentation depth in S_I compared to S_0 reveal the better ability of S_I to resist deformation under an applied force than S_0. Additionally, the near linear relationship between K_L and h in Figure 5.12(b2) can confirm the uniformity of sample S_I. [163] In Figure 5.12(a2) however, a critical turning point is observed for S_0, suggesting the existence of different deformation behaviors. We believe that the loose interface in sample S_0 provides free space to allow easier irreversible deformation of the CZTSe layer, especially during the initial period of the indentation test. When the contact becomes tight, the elastic-plastic deformation behavior dominates and produces a different slope in the K_L~h curve. The elastic modulus and hardness values measured from the unloading (E_U and H_U) and loading (E_L and H_L) curves of S_0 and S_I are listed in Table 5.1. Compared with the theoretically calculated modulus values for the $Cu_2ZnSn(S_xSe_{1-x})_4$ (x=0~1) system in literature (see Table 5.1), [6, 81, 162] our measured values for S_I are in good agreement, while the values for S_0 are much smaller. According to equations (5-1) and (5-2), the smaller measured values of hardness and modulus values in S_0 are attributed to the smaller P_m, larger h_p and smaller K,

which are caused by its loose interface as discussed above. Therefore, the interface microstructures not only determine the film adhesion performances but also have crucial influence on the modulus and hardness measurements.

5.4 Conclusion

CZTSe and CZTSSe films were prepared through selenization of thermally co-evaporated metallic and partially sulfurized precursors. The influences of sulfur in precursor on the film growth were carefully studied by comparative temperature dependent selenization experiments. In addition, film formation models were proposed to demonstrate the detailed growth steps and the reasons for the different back contact interfaces. Intense metal atom migrations across the film were found to form binary grains prior to the effective CZTSe phase formation during selenization of the metallic precursor. Meanwhile, the Mo substrate was found severely corroded and a thick $MoSe_2$ layer was formed. On the other hand, the sulfur incorporation in the original precursor was found to suppress the metal ion migrations and result in a layered film growth procedure, which also reduced the formation of $Mo(SSe)_2$ layer. Although bulk CZTSe and CZTSSe films can be obtained from both sulfur free and sulfur contained precursors, a coherent and compact interface in the sulfur contained sample and a loose interface with a thick $MoSe_2$ and voids layer in the sulfur free sample were observed.

Due to their different interfacial structures, the CZTSe film prepared from a

sulfur free precursor was found to possess poor film adhesion and highly underestimated elastic modulus values. In contrast, the sulfur incorporated sample possessed a much better film adhesion and comparable elastic modulus values to the theoretical simulation. Due to their better mechanical properties, sulfur contained precursors are found more favorable to be used to fabricate solar cell devices.

Chapter 6 Fabrication of CZTSSe based photovoltaic device

6.1 Introduction

Based on the studies of previous chapters, understandings of the formation mechanisms of CZTS based films have been achieved. Bulk CZTSSe films have also been successfully deposited on Mo coated glass substrates. In this chapter, CZTSSe films based photovoltaic devices will be prepared and characterized. Due to a relative short developing history and complicated technologies and layers involved in this device system, interfacial engineering and parameter optimization have not been well established so far. In this chapter, results on the device performance are provided and a device with an efficiency of 5.2% is achieved. It should be mentioned that the device fabrication is preliminary, and further studies on device modifications and characterizations will be arranged in future work.

6.2 Experimental details

Commercially available Mo-coated glasses were applied as the substrate with a size of 2.5cm×3cm. CZTSSe films are prepared on the Mo-coated glass through a co-evaporation of precursors with post-selenization procedure as

discussed in Chapter 5.

A CdS layer is deposited on the CZTSSe layer by chemical bath deposition (CBD). An aqueous precursor solution was prepared using cadmium chloride ($CdCl_2$, >98%), thiourea ($SC(NH_2)_2$, >99%) and ammonia ($NH_3 \cdot H_2O$, 24%). According to literatures on the CBD-CdS growth for CIGS solar cells, [164-167] a 50mL precursor solution contained 2.5mL $CdCl_2$ (0.1mol/L), 5mL thiourea (0.5mol/L), 10mL ammonia (24%) and DI water was prepared with a pH value around 11. The CZTSSe/Mo sample was rinsed by DI water before CdS deposition. Then the sample was immerged into the precursor and moved to a water bath for CdS deposition at 80 ℃ for 12min. After CdS growth, the sample was dried by N_2 blowing and transferred into a vacuum chamber.

ZnO and ITO layers were deposited on the top of the prepared CdS/CZTSSe/Mo by rf-magnetron sputtering at room temperature. The background vacuum of the chamber was pumped to 7×10^{-7}Torr. The working pressure, power and time were 1.2×10^{-2}Torr, 60W and 50min to respectively achieve a ~50nm thick ZnO layer. For the ITO layer, a ~250nm thick film was obtained at the working pressure of 3.6×10^{-3}Torr, power of 110W and deposition time of 22min. Next, the device was heated up to 150 ℃ for 5min in air and then mechanically divided into small cells with a size of 0.3cm×0.4cm.

Finally, the indium metal contact was prepared on each cell as front electrode for device characterizations. The active area of each cell is around $0.1cm^2$.

6.3 Results and discussion

6.3.1 Mo Substrate and CZTSSe film

The XRD pattern of the Mo coated glass shown in Figure 6.1(a) reveals a metallic Mo phase with a (110) preferred orientation. Besides, a smooth and compact surface of the Mo substrate is observed in Figure 6.1(b) and its thickness is around 300nm as demonstrated in Figure 6.1(c).

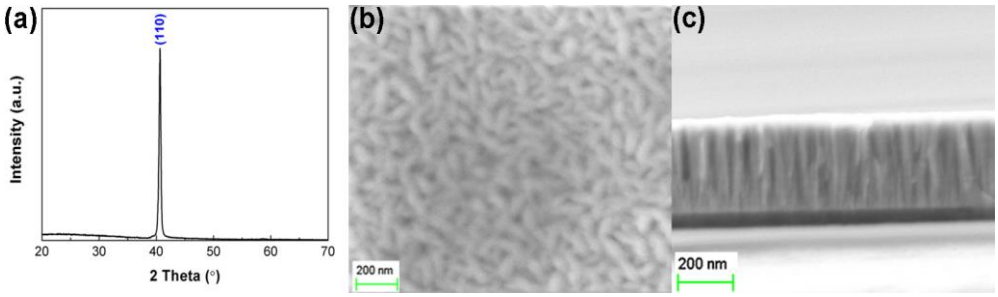

Figure 6.1 (a) XRD pattern, (b) top view and (c) cross-section view SEM images of the Mo substrate.

The CZTSSe layer is prepared on the Mo substrate from a sulfur contained precursor by selenization at 580 ℃. The top view and cross-section view SEM images of the deposited CZTSSe film are shown in Figure 6.2. The size of the surface grains is in micrometers range, and the cross-section reveals a dense and compact layer with good adhesion with the Mo substrate.

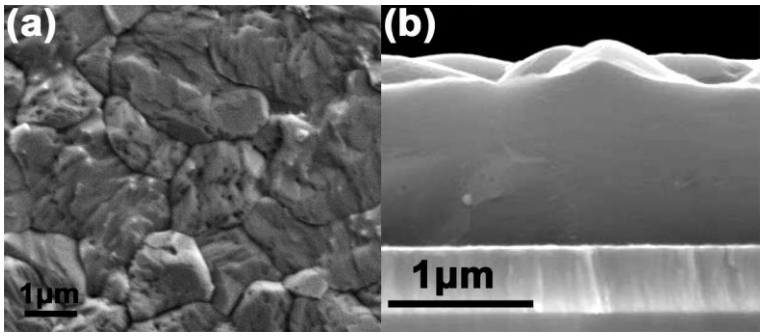

Figure 6.2 (a) Top view and (b) cross-section view SEM images of the prepared CZTSSe film on Mo substrate.

6.3.2 CdS layer

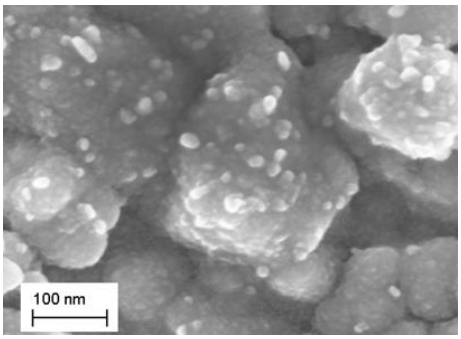

Figure 6.3 SEM image of the CdS layer deposited on the CZTSSe film.

In Figure 6.3, a CdS layer consisting of small grains with a size around 15nm is formed to cover the CZTSSe layer. Similar morphologies of such CdS layer can be found in literature for CIGS based solar cells. [168]

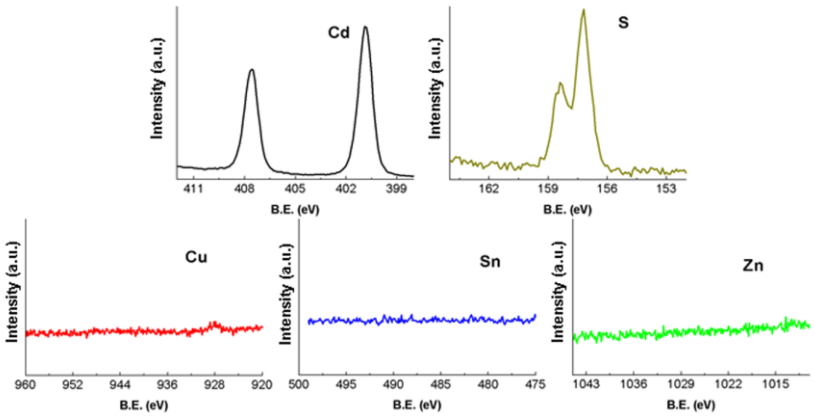

Figure 6.4 High-resolution XPS spectra of the CdS layer.

To examine whether the CdS layer forms a full coverage on the CZTSSe layer, XPS analysis is performed on this CdS layer as shown in Figure 6.4. The XPS peaks corresponding to Cd^{2+} and S^{2-} can be found in Figure 6.4. Otherwise, the signals at the binding energy positions for Cu^{1+}, Zn^{2+} and Sn^{4+} from beneath CZTSSe layer are not detected, which indicates an effective coverage of this CdS layer.

6.3.3 ZnO and ITO layers

Generally, a low sheet resistance and a high transmittance in the visible light region are required for a transparent conducting layer, allowing incident sunlight to pass through and carriers to conduct effectively. [22] An average transmittance of around 85% in the visible light region in Figure 6.5 and a sheet resistance of ~20Ω/□ are achieved for our ITO/ZnO layer, which are acceptable for a photovoltaic device.

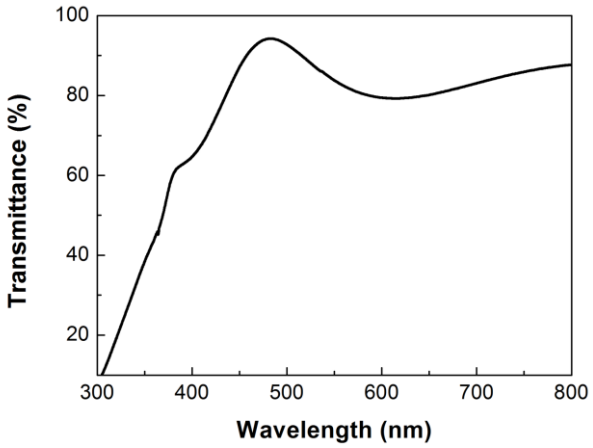

Figure 6.5 Transmittance spectrum of the prepared ITO/ZnO layer.

6.3.4 Characterization of the CZTSSe based solar cell

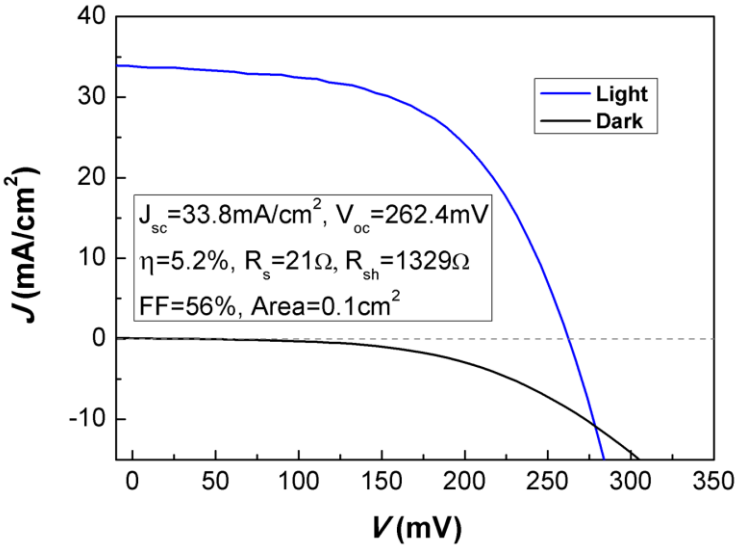

Figure 6.6 J-V curves of Mo/CZTSSe/CdS/ZnO/ITO thin film solar cell under dark and light illumination.

Light J–V and dark J–V measurements of our best CZTSSe based solar cell are shown in Figure 6.6. This device yields a power conversion efficiency (η) of 5.2% with an active area of 0.1cm^2. The detailed device parameters of this device together with the record CZTSSe and CIGSSe based solar cells are listed in Table 6.1 for comparison. [47, 169] The short-circuit current density (J_{sc}) of our device is 33.8 mA/cm^2, comparable with those record cells. However, the open-circuit voltage (V_{oc}) of 262.4mV is much smaller than the record CZTSSe (513.4mV) and CIGSSe (730mV) cells. The fill factor (FF) of our device (56%) is also smaller than those of champion cells (69.8% for CZTSSe cell and 77.7% for CIGSSe cell). The series resistance (R_s) of 21Ω in our cell is also larger than the record cells. But the shunt resistance (R_{sh}) value of our cell is bigger than those record cells, which is considered good for the

performance of a solar cell. Therefore, the major shortages of our cell compared with the record cells are the smaller V_{oc} and larger R_s. One possible reason for the low photovoltage is the recombination that provides pathways to eliminate photo-generated electrons and holes and reduce the amount of charges that can be built-up at the opposite sides of a p-n junction. The intrinsic defects, band gap tailing and secondary phases are considered as the origins to activate the recombination in the CZTS based solar cells. Although the CdS contact works well for the CIGS based solar cells, the bandgap mismatch and interfacial states between the CZTS based layer and CdS layer could also be the other possible reason for the low photovoltage.

Table 6.1 Device characteristics, power conversion efficiency (η), short-circuit current density (J_{sc}), open-circuit voltage (V_{oc}), fill factor (FF), series resistance (R_s) and shunt resistance (R_{sh}), of our best CZTSSe solar cell (B-CZTSSe) compared to a record CZTSSe cell from IBM (IBM-CZTSSe) [47] and a record CIGSSe cell reported by ZSW (ZSW-CIGSSe) [169].

Samples	η/%	J_{sc}/ mA/cm^2	V_{oc}/ mV	FF/%	R_s/Ω	R_{sh}/Ω
B-CZTSe	5.2	33.8	262.4	56	21	1329
IBM-CZTSSe	12.6	35.2	513.4	69.8	1	901
ZSW-CIGSSe	20.3	35.7	730	77.7	0.3	1211

6.4 Conclusion

CZTSSe based solar cell devices were fabricated by sequential deposition of CZTSSe, CdS, ZnO and ITO layers on Mo coated glass substrates.

Characterization of each layer was carried out to demonstrate suitable properties for a solar cell. A successful device was achieved with a power conversion efficiency of 5.2%. Its small open-circuit voltage and large series resistance were revealed as the major problems that limit its efficiency. Although the performances of this device are worse than the reported devices now, device improvements are expected by deeper analysis on the materials and interfaces and better adjustment of the fabrication conditions in the future.

Chapter 7 Conclusion and future work

7.1 Conclusion

In order to develop low cost photovoltaic materials, CZTS based films were attracted increasing attention due to their comparable properties with the successful CIGS system. However, severe phase stability issues arise in the CZTS system, which makes it a challenge to grow high quality CZTS based films and degrades their device performances. In this thesis, the phase formation mechanisms and film growth procedures were extensively explored by carefully designed experiments and theoretical analysis. The major conclusions are summarized in several aspects as following.

1. By studying the decomposition of CZTS, in addition to the expected phenomena of Sn losses, deeper understandings of the phase degradation mechanisms and indications on the formation conditions of a stable CZTS based material were achieved. For the Sn loss, an equimolar-isobaric mode transition was demonstrated in this study, suggesting the decomposition of CZTS initiated from a temperature and pressure dependent vaporization procedure. A relatively high annealing pressure was employed and the suppression of Sn loss was achieved, even when a higher temperature is needed to activate effective grain growth.

   Furthermore, an interesting Cu-Zn separation and valance state change of

copper ions from Cu^{1+} to Cu^{2+} were revealed, which provided another mechanism other than the change of S^{2-} to S^{0} that would compensate the valance alternation of Sn^{4+} to Sn^{2+} during Sn loss procedure.

2. A two-step film growth strategy, involving a low temperature precursor deposition and a high pressure post-annealing, was proposed. Following this strategy, CZTSSe films were successfully prepared by the selenization of co-evaporated Cu-Sn-Zn-S precursor in an Ar+Se atmosphere and the Sn loss problem was overcome. Different secondary phases were found at different locations in the CZTSSe films when the precursor films were with various metal contents. Through a temperature dependent annealing study on a near-stoichiometric precursor, the secondary phase segregation and CZTSSe phase formation procedures were revealed. Besides, convincing theoretical explanations on these phase formation mechanisms were obtained by thermodynamic analysis on the related sulfurization and selenization reactions.
3. The impacts of sulfur incorporation in precursors on the growth of CZTSSe films were explored by a comparative temperature dependent annealing study on thermally co-evaporated metallic and sulfur contained precursors. It was found that binary grains were formed with intense metal atom migrations across the film prior to the effective CZTSe phase formation during selenization of the metallic precursor. Meanwhile, the Mo substrate was also found severely corroded and a thick $MoSe_2$ layer

was formed. On the other hand, the sulfur incorporation in the original precursor was found to suppress the metal ion migrations and result in a layered film growth procedure, which also reduced the formation of $Mo(SSe)_2$ layer.

The CZTSe film prepared from the sulfur free precursor was found to possess poor film adhesion and highly underestimated elastic modulus values. In contrast, the sulfur incorporated sample possessed a much better film adhesion and comparable elastic modulus values to the theoretical simulation. These findings suggest that the partially sulfurized precursor was preferred for a CZTSSe based solar cell device fabrication.

4. A CZTSSe based solar cell device with a power conversion efficiency of 5.2% was achieved by sequential deposition of CZTSSe, CdS, ZnO and ITO layers on Mo coated glass substrates. The small open-circuit voltage and large series resistance were revealed as the major problems that limit the efficiency.

7.2 Future work

In this thesis, the major efforts were made to address the phase stability problems of CZTS based materials and explore the film formation mechanisms during post annealing treatment. Based on the understanding obtained in this work and literatures, there are several aspects regarding to the CZTS based films and device structures need to be discussed further.

1. Defects in CZTS based films

The defects formation in CZTS based films is important, especially for the photovoltaic applications, because the electrical properties of these absorber layers are mainly determined by their intrinsic defects and hence the characteristics of the p-n junction are significantly influenced. [109] In another way, the defects also provide recombination sites for the photo-generated carrier pairs, greatly degrading the solar cell performances. [170] Although some theoretical simulation works have been carried out to study the defects in CZTS based materials, the defects formation mechanisms in real film samples have not been well established. In addition, the voids can also be considered as structural defects, which are also claimed to be harmful to a solar cell device. [25] However, the effects of these defects on the optoelectronic properties of CZTS based films and the methods to increase the preferred defects and passivate the unwanted defects are still unclear. Therefore, careful studies on the defects formation during film preparation and its consequences on the device performances are needed.

2. Grain boundaries in CZTS based films

Compared with the CIGS solar cells, similar grain size can be obtained in the case of CZTS. However, due to the different chemical composition of these two materials, the grain boundaries may exhibit quite different properties and these have important impacts on the device. [71, 171] As

very limited works have been reported on this issue, [171] the influences of compositional variations and fabrication procedures on the properties of grain boundaries are worthy of further study.

3. Interfaces between CdS/CZTS/Mo layers

Because the Mo substrate and CdS n-type contact work well in the CIGS solar cells and the device structure of CZTS based solar cells just follows CIGS so far, the interface matching between CZTS and Mo or CdS may have different performances from the CIGS case. For example, the contact between Mo and CZTS was claimed to trigger phase decomposition and create secondary phases, which did not occur in the CIGS case. [123] The detailed band alignments between CZTS and CdS and any surface or composition modifications' influences on the band structures are not well studied. [172] In addition, environmental friendly layers are expected to substitute the toxic CdS layer. Furthermore, explorations on the interfacial performances generated by other different contact materials are also of great interests. A better understanding on the properties of the CZTSSe layer and its contacts with other layers is expected to improve the device performance in the future.

Bibliography

[1] Follath E., *Natural resources are fuelling a new cold war.* Spiegel Online, 2006.

[2] Wilson G. and K. Emery, *http://www.nrel.gov/ncpv/images/efficiency_chart.jpg.* 2014. **2014**.

[3] Wang H., *Progress in thin film solar cells based on Cu_2ZnSnS_4.* International Journal of Photoenergy, 2011. **2011**: p. 801292.

[4] Paier J., et al., Cu_2ZnSnS_4 as a potential photovoltaic material: A hybrid Hartree-Fock density functional theory study. Physical Review B, 2009. **79**: p. 115126.

[5] Hall S., et al., *Kesterite, $Cu_2(Zn,Fe)SnS_4$, and stannite, $Cu_2(Fe,Zn)SnS_4$, structurally similar but distinct minerals.* The Canadian Mineralogist, 1978. **16**: p. 131-137.

[6] Camps I., et al., *Elastic and optical properties of $Cu_2ZnSn(Se_xS_{1-x})_4$ alloys: density functional calculations.* Semiconductor Science and Technology, 2012. **27**: p. 115001.

[7] Tanaka T., et al., *Influence of composition ratio on properties of Cu_2ZnSnS_4 thin films fabricated by co-evaporation.* Thin Solid Films, 2010. **518**: p. S29.

[8] Suresh Babu G., et al., *Effect of Cu/(Zn+Sn) ratio on the properties of co-evaporated $Cu_2ZnSnSe_4$ thin films.* Solar Energy Materials and Solar Cells, 2010. **94**: p. 221.

[9] Katagiri H., et al., *Characterization of Cu_2ZnSnS_4 thin films prepared by vapor phase sulfurization.* Japanese Journal of Applied Physics, 2001. **40**: p. 500.

[10] Mendis B. G., et al., *Direct observation of Cu, Zn cation disorder in Cu2ZnSnS4 solar cell absorber material using aberration corrected scanning transmission electron microscopy.* Progress in Photovoltaics: Research and Applications, 2014. **22**(1): p. 24.

[11] Fernandes P., et al., *Admittance spectroscopy of Cu_2ZnSnS_4 based thin film solar cells.* Applied Physics Letters, 2012. **100**: p. 233504.

[12] Kask E., et al., *Defect studies in $Cu_2ZnSnSe_4$ and $Cu_2ZnSn(Se_{0.75}S_{0.25})_4$ by admittance and photoluminescence spectroscopy.* Materials Science in Semiconductor Processing, 2013. **16**: p. 992.

[13] Chen S., et al., *Intrinsic point defects and complexes in the quaternary kesterite semiconductor Cu_2ZnSnS_4.* Physical Review B, 2010. **81**: p. 245204.

[14] Chen S., et al., *Defect physics of the kesterite thin-film solar cell absorber Cu_2ZnSnS_4.* Applied Physics Letters, 2010. **96**: p. 021902.

[15] Guo Q., et al., *Fabrication of 7.2% efficient CZTSSe solar cells using CZTS nanocrystals.* Journal of the American Chemical Society, 2010. **132**: p. 17384.

[16] Wang K., et al., *Thermally evaporated Cu_2ZnSnS_4 solar cells.* Applied Physics Letters, 2010. **97**: p. 143508.

[17] Kosyak V., et al., *Temperature dependent conductivity of polycrystalline Cu_2ZnSnS_4 thin films.* Applied Physics Letters, 2012. **100**: p. 263903.

[18] Gonzalez J., et al., *Hopping conduction and persistent photoconductivity in Cu_2ZnSnS_4 thin films.* Journal of Physics D: Applied Physics, 2013. **46**: p. 155107.

[19] Leitão J. P., et al., *Photoluminescence and electrical study of fluctuating potentials in Cu_2ZnSnS_4-based thin films.* Physical Review B, 2011. **84**: p. 024120.

[20] Ito K. and T. Nakazawa, *Electrical and optical properties of stannite-type quaternary semiconductor thin films.* Japanese Journal of Applied Physics, 1988. **27**: p. 2094.

[21] Kishore Kumar Y., et al., *Preparation and characterization of spray-deposited Cu_2ZnSnS_4 thin films.* Solar Energy Materials and Solar Cells, 2009. **93**: p. 1230.

[22] Guo Q., et al., *Synthesis of Cu_2ZnSnS_4 nanocrystal ink and its use for solar cells.* Journal of the American Chemical Society, 2009. **131**: p. 11672.

[23] Wei H., et al., *Tunable band gap $Cu_2ZnSnS_{4x}Se_{4(1-x)}$ nanocrystals: experimental and first-principles calculations.* CrystEngComm, 2011. **13**: p. 2222.

[24] Chen S., et al., *Compositional dependence of structural and electronic*

properties of $Cu_2ZnSn(S,Se)_4$ alloys for thin film solar cells. Physical Review B, 2011. **83**: p. 125201.

[25] Todorov T. K., et al., *High-efficiency solar cell with Earth-abundant liquid-processed absorber.* Advanced Materials, 2010. **22**: p. E156.

[26] Timmo K., et al., *Sulfur-containing $Cu_2ZnSnSe_4$ monograin powders for solar cells.* Solar Energy Materials and Solar Cells, 2010. **94**: p. 1889.

[27] Grossberg M., et al., *Photoluminescence and Raman study of $Cu_2ZnSn(Se_xS_{1-x})_4$ monograins for photovoltaic applications.* Thin Solid Films, 2011. **519**: p. 7403.

[28] Ahmed S., et al., *A High Efficiency Electrodeposited Cu_2ZnSnS_4 Solar Cell.* Advanced Energy Materials, 2012. **2**: p. 253.

[29] Riha S. C., et al., *Solution-based synthesis and characterization of Cu_2ZnSnS_4 nanocrystals.* Journal of the American Chemical Society, 2009. **131**: p. 12054.

[30] Haas W., et al., *The stoichiometry of single nanoparticles of copper zinc tin selenide.* Chemical communications, 2011. **47**: p. 2050.

[31] Zhou Y.-L., et al., *Hierarchical Cu_2ZnSnS_4 particles for a low-cost solar cell: morphology control and growth mechanism.* The Journal of Physical Chemistry C, 2011. **115**: p. 19632.

[32] Zaberca O., et al., *Surfactant-free CZTS nanoparticles as building blocks for low-cost solar cell absorbers.* Nanotechnology, 2012. **23**: p. 185402.

[33] Xu J., et al., *Cu_2ZnSnS_4 hierarchical microspheres as an effective counter electrode material for quantum dot sensitized solar cells.* The Journal of Physical Chemistry C, 2012. **116**: p. 19718.

[34] Adhi Wibowo R., et al., *Synthesis of $Cu_2ZnSnSe_4$ compound powders by solid state reaction using elemental powders.* Journal of Physics and Chemistry of Solids, 2010. **71**: p. 1702.

[35] Wang Y. and H. Gong, *Cu_2ZnSnS_4 synthesized through a green and economic process.* Journal of Alloys and Compounds, 2011. **509**: p. 9627.

[36] Wibowo R. A., et al., *Crystallization of $Cu_2ZnSnSe_4$ compound by solid state reaction using elemental powders.* Materials Chemistry and Physics, 2010. **124**: p. 1006.

[37] Wang Y. and H. Gong, *Low temperature synthesized quaternary chalcogenide Cu_2ZnSnS_4 from nano-crystallite binary sulfides.* Journal of The Electrochemical Society, 2011. **158**: p. H800.

[38] Tanaka K., et al., *Preparation of Cu_2ZnSnS_4 thin films by sulfurizing sol–gel deposited precursors.* Solar Energy Materials and Solar Cells, 2007. **91**: p. 1199.

[39] Xin H., et al., *8% efficient $Cu_2ZnSn(S,Se)_4$ solar cells from redox equilibrated simple precursors in DMSO.* Advanced Energy Materials, 2014. 4: p. 1301823.

[40] Wang Y., et al., *Influence of sintering temperature on screen printed Cu_2ZnSnS_4 (CZTS) films.* Journal of Alloys and Compounds, 2012. **539**: p. 237.

[41] Steinhagen C., et al., *Synthesis of Cu_2ZnSnS_4 nanocrystals for use in low-cost photovoltaics.* Journal of the American Chemical Society, 2009. **131**: p. 12554.

[42] Pawar B., et al., *Effect of complexing agent on the properties of electrochemically deposited Cu_2ZnSnS_4 (CZTS) thin films.* Applied Surface Science, 2010. **257**: p. 1786.

[43] Sarswat P. K., et al., *CZTS thin films on transparent conducting electrodes by electrochemical technique.* Thin Solid Films, 2012. **520**: p. 1694.

[44] Wangperawong A., et al., *Aqueous bath process for deposition of Cu_2ZnSnS_4 photovoltaic absorbers.* Thin Solid Films, 2011. **519**: p. 2488.

[45] Kamoun N., et al., *Fabrication and characterization of Cu_2ZnSnS_4 thin films deposited by spray pyrolysis technique.* Thin Solid Films, 2007. **515**: p. 5949.

[46] Kumar Y., et al., *Effect of copper salt and thiourea concentrations on the formation of Cu_2ZnSnS_4 thin films by spray pyrolysis.* Physica Status Solidi (a), 2010. **207**: p. 149.

[47] Wang W., et al., *Device Characteristics of CZTSSe Thin-Film Solar Cells with 12.6% Efficiency.* Advanced Energy Materials, 2013. **4**: p. 1301465.

[48] Cao Y., et al., *High-efficiency solution-processed $Cu_2ZnSn(S,Se)_4$ thin-film solar cells prepared from binary and ternary nanoparticles.* Journal of the American Chemical Society, 2012. **134**: p. 15644.

[49] Miskin C. K., et al., *9.0% efficient $Cu_2ZnSn(S,Se)_4$ solar cells from selenized nanoparticle inks.* Progress in Photovoltaics: Research and Applications, 2014. DOI: 10.1002/pip.2472.

[50] Shin B., et al., *Thin film solar cell with 8.4% power conversion efficiency using an earth-abundant Cu_2ZnSnS_4 absorber.* Progress in Photovoltaics: Research and Applications, 2013. **21**: p. 72.

[51] Shin B., et al., *Control of an interfacial $MoSe_2$ layer in $Cu_2ZnSnSe_4$ thin film solar cells: 8.9% power conversion efficiency with a TiN diffusion barrier.* Applied Physics Letters, 2012. **101**: p. 053903.

[52] Guo L., et al., *Electrodeposited $Cu_2ZnSnSe_4$ thin film solar cell with 7% power conversion efficiency.* Progress in Photovoltaics: Research and Applications, 2014. **22**: p. 58.

[53] Redinger A. and S. Siebentritt, *Coevaporation of $Cu_2ZnSnSe_4$ thin films.* Applied Physics Letters, 2010. **97**: p. 092111.

[54] Weber A., et al., *On the Sn loss from thin films of the material system Cu–Zn–Sn–S in high vacuum.* Journal of Applied Physics, 2010. **107**: p. 013516.

[55] Redinger A., et al., *The consequences of kesterite equilibria for efficient solar cells.* Journal of the American Chemical Society, 2011. **133**: p. 3320.

[56] Scragg J. J., et al., *Chemical insights into the instability of Cu_2ZnSnS_4 films during annealing.* Chemistry of Materials, 2011. **23**: p. 4625.

[57] Fontané X., et al., *In-depth resolved Raman scattering analysis for the identification of secondary phases: Characterization of Cu_2ZnSnS_4 layers for solar cell applications.* Applied Physics Letters, 2011. **98**: p. 181905.

[58] Scragg J. J., et al., *A 3.2% efficient Kesterite device from electrodeposited stacked elemental layers.* Journal of Electroanalytical Chemistry, 2010. **646**: p. 52.

[59] Schubert B.-A., et al., *Cu_2ZnSnS_4 thin film solar cells by fast coevaporation.* Progress in Photovoltaics: Research and Applications, 2011. **19**: p. 93.

[60] Sevik C. and T. Çağın, *Ab initio study of thermoelectric transport properties of pure and doped quaternary compounds.* Physical Review B, 2010. **82**: p. 045202.

[61] Sevik C. and T. Çağın, *Assessment of thermoelectric performance of Cu_2ZnSnX_4, X=S, Se, and Te.* Applied Physics Letters, 2009. **95**: p. 112105.

[62] Liu M.-L., et al., *A wide-band-gap p-type thermoelectric material based on quaternary chalcogenides of Cu_2ZnSnQ_4 (Q=S,Se).* Applied Physics Letters, 2009. **94**: p. 202103.

[63] Nagoya A. and R. Asahi, *Defect formation and phase stability of Cu_2ZnSnS_4 photovoltaic material.* Physical Review B, 2010. **81**: p. 113202.

[64] Scragg J. J., *Studies of Cu_2ZnSnS_4 films prepared by sulfurisation of electrodeposited precursors.* 2010. Doctoral thesis: p. 122.

[65] Gartsman K., et al., *Direct evidence for diffusion and electromigration of Cu in $CuInSe_2$.* Journal of Applied Physics, 1997. **82**: p. 4282.

[66] Allen L. H. and E. Buhks, *Copper electromigration in polycrystalline copper sulfide.* Journal of Applied Physics, 1984. **56**: p. 327.

[67] Olekseyuk I., *Phase equilibria in the Cu_2S–ZnS–SnS_2 system.* Journal of Alloys and Compounds, 2004. **368**: p. 135.

[68] Just J., et al., *Determination of secondary phases in kesterite Cu_2ZnSnS_4 thin films by x-ray absorption near edge structure analysis.* Applied Physics Letters, 2011. **99**: p. 262105.

[69] Redinger A., et al., *Detection of a ZnSe secondary phase in coevaporated $Cu_2ZnSnSe_4$ thin films.* Applied Physics Letters, 2011. **98**: p. 101907.

[70] Wang K., et al., *Structural and elemental characterization of high efficiency Cu_2ZnSnS_4 solar cells.* Applied Physics Letters, 2011. **98**: p. 051912.

[71] Mendis B. G., et al., *The role of secondary phase precipitation on grain boundary electrical activity in Cu_2ZnSnS_4 (CZTS) photovoltaic absorber layer material.* Journal of Applied Physics, 2012. **112**: p. 124508.

[72] Vigil-Galán O., et al., *Secondary phases dependence on composition ratio in sprayed Cu_2ZnSnS_4 thin films and its impact on the high power conversion efficiency.* Solar Energy Materials and Solar Cells, 2013. **117**: p. 246.

[73] Fairbrother A., et al., *On the formation mechanisms of Zn-rich Cu_2ZnSnS_4 films prepared by sulfurization of metallic stacks.* Solar Energy Materials and Solar Cells, 2013. **112**: p. 97.

[74] Bär M., et al., *Impact of KCN etching on the chemical and electronic surface structure of Cu_2ZnSnS_4 thin-film solar cell absorbers.* Applied Physics Letters, 2011. **99**: p. 152111.

[75] Lee K. D., et al., *Preparation of Cu_2ZnSnS_4 thin films via electrochemical deposition and rapid thermal annealing.* Thin Solid Films, 2013. **546**: p. 294.

[76] Redinger A., et al., *$Cu_2ZnSnSe_4$ thin film solar cells produced via co-evaporation and annealing including a $SnSe_2$ capping layer.* Progress in Photovoltaics: Research and Applications, 2014. **22**: p. 51.

[77] Fairbrother A., et al., *Development of a selective chemical etch to improve the conversion efficiency of Zn-rich Cu_2ZnSnS_4 solar cells.* Journal of the American Chemical Society, 2012. **134**: p. 8018.

[78] Platzer-Björkman C., et al., *Influence of precursor sulfur content on film formation and compositional changes in Cu_2ZnSnS_4 films and solar cells.* Solar Energy Materials and Solar Cells, 2012. **98**: p. 110.

[79] Park D., et al., *Optical characterization of $Cu_2ZnSnSe_4$ grown by thermal co-evaporation.* Thin Solid Films, 2011. **519**: p. 7386.

[80] Yin X., et al., *Study on phase formation mechanism of non- and near-stoichiometric $Cu_2ZnSn(S,Se)_4$ film prepared by selenization of Cu–Sn–Zn–S precursors.* Chemistry of Materials, 2014. **26**: p. 2005.

[81] Gunaicha P. P., et al., *Structural, energetic and elastic properties of $Cu_2ZnSn(S_xSe_{1-x})_4$ (x=1, 0.75, 0.5, 0.25, 0) alloys from first-principles computations.* Solar Energy, 2014. **102**: p. 276.

[82] Shin B., et al., *On the kinetics of $MoSe_2$ interfacial layer formation in chalcogen-based thin film solar cells with a molybdenum back contact.* Applied Physics Letters, 2013. **102**: p. 091907.

[83] Scragg J. J., et al., *A detrimental reaction at the molybdenum back contact in $Cu_2ZnSn(S,Se)_4$ thin-film solar cells.* Journal of the American Chemical Society, 2012. **134**: p. 19330.

[84] Liu F., et al., *Enhancing the Cu_2ZnSnS_4 solar cell efficiency by back contact modification: Inserting a thin TiB_2 intermediate layer at Cu_2ZnSnS_4/Mo interface.* Applied Physics Letters, 2014. **104**: p. 051105.

[85] López-Marino S., et al., *Inhibiting the absorber/Mo-back contact decomposition reaction in $Cu_2ZnSnSe_4$ solar cells: the role of a ZnO*

intermediate nanolayer. Journal of Materials Chemistry A, 2013. **1**: p. 8338.

[86] Elidrissi B., et al., *Structure, composition and optical properties of ZnS thin films prepared by spray pyrolysis.* Materials Chemistry and Physics, 2001. **68**: p. 175.

[87] Koteswara Reddy N. and K. Ramakrishna Reddy, *Growth of polycrystalline SnS films by spray pyrolysis.* Thin Solid Films, 1998. **325**: p. 4.

[88] Naşcu C., et al., *Spray pyrolysis deposition of CuS thin films.* Materials Letters, 1997. **32**: p. 73.

[89] Adelifard M., et al., *Preparation and characterization of Cu_2SnS_3 ternary semiconductor nanostructures via the spray pyrolysis technique for photovoltaic applications.* Physica Scripta, 2012. **85**: p. 035603.

[90] Madarász J., et al., *Thermal decomposition of thiourea complexes of Cu(I), Zn(II), and Sn(II) chlorides as precursors for the spray pyrolysis deposition of sulfide thin films.* Solid State Ionics, 2001. **141**: p. 439.

[91] Yoo H. and J. Kim, *Comparative study of Cu_2ZnSnS_4 film growth.* Solar Energy Materials and Solar Cells, 2011. **95**: p. 239.

[92] Stull D. R., *Vapor pressure of pure substances. Organic and inorganic compounds.* Industrial & Engineering Chemistry, 1947. **39**: p. 517.

[93] Yaws C. L., *Handbook of Vapor Pressure Vol. 4: Inorganic Compounds and Elements.* 1995. Gulf Professional Publishing, (Houston) USA .

[94] Harsha K. S., *Principles of vapor deposition of thin films.* 2005. Elsevier, (Oxford) UK.

[95] Mattox D. M., *Handbook of physical vapor deposition (PVD) processing.* 2010. William Andrew, (Burlington) USA.

[96] Volinsky A., et al., *Nanoindentation methods in interfacial fracture testing.* Encyclopedia on Comprehensive Structural Integrity, 2003. **8**: p. 453.

[97] Maissel L. I. and R. Glang, *Handbook of thin film technology.* 1970. McGraw-Hill, (New York) USA.

[98] Ahn J., et al. I*n Adhesion measurement of thin films, thick films and bulk coatings.* ASTM, 1978. p 134.

[99] Heavens O., *Some factors influencing the adhesion of films produced by vacuum evaporation.* J. Phys. Radium, 1950. **11**: p. 355.

[100] Consiglio R., et al., *The nano-scratch tester (NST) as a new tool for assessing the strength of ultrathin hard coatings and the mar resistance of polymer films.* Thin Solid Films, 1998. **332**: p. 151.

[101] Huang L.-Y., et al., *Analysis of nano-scratch behavior of diamond-like carbon films.* Surface and Coatings Technology, 2002. **154**: p. 232.

[102] Bull S., *Failure mode maps in the thin film scratch adhesion test.* Tribology International, 1997. **30**: p. 491.

[103] Burnett P. and D. Rickerby, *The relationship between hardness and scratch adhesion.* Thin Solid Films, 1987. **154**: p. 403.

[104] Fischer-Cripps A. C., *Nanoindentation.* 2011. Springer, (New York) USA.

[105] Oliver W. C. and G. M. Pharr, *An improved technique for determining hardness and elastic modulus using load and displacement sensing indentation experiments.* Journal of materials research, 1992. **7**: p. 1564.

[106] Oliver W. C. and G. M. Pharr, *Measurement of hardness and elastic modulus by instrumented indentation: Advances in understanding and refinements to methodology.* Journal of Materials Research, 2004. 19: p. 3.

[107] Lucas B., et al. *In The dynamics of frequency-specific, depth-sensing indentation testing.* MRS Proceedings, Cambridge Univ Press: 1998; p 3.

[108] Markvarta T. and L. Castañerb, *Practical Handbook of Photovoltaics: Fundamentals and Applications.* 2011. Elsevier, (Oxford) UK.

[109] Nelson J., *The physics of solar cells.* 2003. Imperial Collage Press, (London) UK.

[110] Fonash S., *Solar cell device physics.* 2012. Elsevier, (Oxford) UK.

[111] Altosaar M., et al., *$Cu_2Zn_{1-x}Cd_xSn(Se_{1-y}S_y)_4$ solid solutions as absorber materials for solar cells.* Physica Status Solidi (a), 2008. **205**: p. 167.

[112] Zou C., et al., *Facile synthesis of Cu_2ZnSnS_4 nanocrystals.* CrystEngComm, 2011. **13**: p. 3310.

[113] Su Z., et al., *Fabrication of Cu_2ZnSnS_4 nanowires and nanotubes based on AAO templates.* CrystEngComm, 2012. **14**: p. 782.

[114] Khare A., et al., *Size control and quantum confinement in Cu_2ZnSnS_4 nanocrystals.* Chemical communications, 2011. **47**: p. 11721.

[115] Metiu H., *Physical Chemistry: Kinetics.* 2006. Taylor & Francis, (London) UK.

[116] Espenson J. H., *Chemical kinetics and reaction mechanisms.* 1981. McGraw-Hill, (New York) USA.

[117] Upadhyay S. K., *Chemical Kinetics and Reaction Dynamics.* 2006. Springer, (New York) USA.

[118] Langmuir I., *The vapor pressure of metallic tungsten.* Physical Review, 1913. **2**: p. 329.

[119] Dollimore D., et al., *Correlation between the shape of a TG/DTG curve and the form of the kinetic mechanism which is applying.* Thermochimica Acta, 1992. **198**: p. 249.

[120] Lvov B. V., *Thermal Decomposition of Solids and Melts, Part I.* 2007. Springer, (Berlin) Germany.

[121] Sturgeon R. E., et al., *Studies on the mechanism of atom formation in graphite furnace atomic absorption spectrometry.* Analytical Chemistry, 1976. **48**: p. 1792.

[122] Piacente V., et al., *Sublimation study of the tin sulphides SnS_2, Sn_2S_3 and SnS.* Journal of Alloys and Compounds, 1991. **177**: p. 17.

[123] Scragg J. J., et al., *A detrimental reaction at the molybdenum back contact in $Cu_2ZnSn(S,Se)_4$ thin-film solar cells.* Journal of the American Chemical Society, 2012. **134**: p. 19330.

[124] Nagoya A., et al., *Defect formation and phase stability of Cu_2ZnSnS_4 photovoltaic material.* Physical Review B, 2010. **81**: p. 113202.

[125] Maeda T., et al., *First principles calculations of defect formation in in-free photovoltaic semiconductors Cu_2ZnSnS_4 and $Cu_2ZnSnSe_4$.* Japanese Journal of Applied Physics, 2011. **50**: p. 04DP07.

[126] He X., et al., *Elastic and thermo-physical properties of stannite-type*

Cu_2ZnSnS_4 and $Cu_2ZnSnSe_4$ from first-principles calculations. Acta Metallurgica Sinica (English Letters), 2013. **26**: p. 285.

[127] Scragg J. J., et al., *Chemical insights into the instability of Cu_2ZnSnS_4 films during annealing.* Chemistry of Materials, 2011. **23**: p. 4625.

[128] Scragg J. J., et al., *Thermodynamic aspects of the synthesis of thin-film materials for solar cells.* ChemPhysChem, 2012. **13**: p. 3035.

[129] Barin I., *Thermochemical properties of inorganic substances: supplement.*1977. Springer, (Berlin) Germany.

[130] Vaughan D. J. and J. R. Craig, *Mineral Chemistry of Metal Sulfides.* 1978. Cambridge University Press, (Cambridge) UK.

[131] Babanly M. B., et al., *Phase diagrams and thermodynamic properties of the Cu-B^{IV}(B^{V})-Chalcogen systems.* Proceedings of VI International School-Conference "Phase Diagrams in Material Science", 2001. (Kiev) Ukraine.

[132] Barin I. and O. Knacke, *Thermochemical properties of inorganic substances.* 1973. Springer, (Berlin) Germany.

[133] Flandorfer H., et al., *Interfaces in lead-free solder alloys: Enthalpy of formation of binary Ag–Sn, Cu–Sn and Ni–Sn intermetallic compounds.* Thermochimica Acta, 2007. **459**: p. 34.

[134] Li D., et al., *The Cu–Sn phase diagram part II: New thermodynamic assessment.* Intermetallics, 2013. **34**: p. 148.

[135] Maeda T., et al., *First principles calculations of defect formation in In-free photovoltaic semiconductors Cu2ZnSnS4 and Cu2ZnSnSe4.* Japanese Journal of Applied Physics, 2011. **50**: p. 04DP07.

[136] Chandrasekhar H. R., et al., *Infrared and Raman spectra of the IV-VI compounds SnS and SnSe.* Physical Review B, 1977. **15**: p. 2177.

[137] Klavina I., et al., *Study of $Cu_2ZnSnSe_4$ monograin formation in molten KI starting from binary chalcogenides.* Thin Solid Films, 2011. **519**: p. 7399.

[138] Grossberg M., et al., *Photoluminescence and Raman study of $Cu_2ZnSn(Se_xS_{1-x})_4$ monograins for photovoltaic applications.* Thin Solid Films, 2011. **519**: p. 7403.

[139] He J., et al., *Composition dependence of structure and optical properties of $Cu_2ZnSn(S,Se)_4$ solid solutions: An experimental study.* Journal of Alloys and Compounds, 2012. **511**: p. 129.

[140] Marcano G., et al., *Raman spectrum of monoclinic semiconductor.* Solid State Communications, 2011. **151**: p. 84.

[141] Tanaka T., et al., *Existence and removal of Cu_2Se second phase in coevaporated $Cu_2ZnSnSe_4$ thin films.* Journal of Applied Physics, 2012. **111**: p. 053522.

[142] Fischereder A., et al., *Investigation of Cu_2ZnSnS_4 formation from metal salts and thioacetamide.* Chemistry of Materials, 2010. **22**: p. 3399.

[143] Bar M., et al., *Impact of KCN etching on the chemical and electronic surface structure of Cu_2ZnSnS_4 thin-film solar cell absorbers.* Applied Physics Letters, 2011. **99**: p. 152111.

[144] Fairbrother A., et al., *Development of a selective chemical etch to improve the conversion efficiency of Zn-Rich Cu_2ZnSnS_4 solar cells.* Journal of the American Chemical Society, 2012. **134**: p. 8018.

[145] Lee K. D., et al., *Preparation of Cu_2ZnSnS_4 thin films via electrochemical deposition and rapid thermal annealing.* Thin Solid Films, 2013. **546**: p. 294.

[146] Redinger A., et al., *$Cu_2ZnSnSe_4$ thin film solar cells produced via co-evaporation and annealing including a $SnSe_2$ capping layer.* Progress in Photovoltaics: Research and Applications, 2014. **22**: p. 51.

[147] Fairbrother A., et al., *On the formation mechanisms of Zn-rich Cu_2ZnSnS_4 films prepared by sulfurization of metallic stacks.* Solar Energy Materials and Solar Cells, 2013. **112**: p. 97.

[148] Guo Q., et al., *Enhancing the performance of CZTSSe solar cells with Ge alloying.* Solar Energy Materials and Solar Cells, 2012. **105**: p. 132.

[149] Kuo D.-H. and T.-R. Jan, *Large-grained $Cu_2ZnSnSe_4$ absorbers prepared with nano-sized Cu-Zn-SnSe cermet pastes and subsequent selenization at 600–700 ℃.* ECS Solid State Letters, 2012. **1**: p. Q54.

[150] Han J., et al., *Crystallization behaviour of co-sputtered Cu_2ZnSnS_4 precursor prepared by sequential sulfurization processes.* Nanotechnology, 2013. **24**: p. 095706.

[151] Shin B., et al., *Thin film solar cell with 8.4% power conversion efficiency using an earth-abundant Cu_2ZnSnS_4 absorber.* Progress in Photovoltaics: Research and Applications, 2013. **21**: p. 72.

[152] Todorov T. K., et al., *Beyond 11% Efficiency: Characteristics of State-of-the-Art $Cu_2ZnSn(S,Se)_4$ Solar Cells.* Advanced Energy Materials, 2013. **3**: p. 34.

[153] Scott J., et al., *Resonant Raman scattering in ZnS and ZnSe with the cadmium laser.* Optics Communications, 1970. **1**: p. 397.

[154] Park J., et al., *Micro-Raman spectroscopy in polycrystalline $CuInSe_2$ formation.* Applied Physics A, 1994. **58**: p. 125.

[155] Tanaka T., et al., *Existence and removal of Cu_2Se second phase in coevaporated $Cu_2ZnSnSe_4$ thin films.* Journal of Applied Physics, 2012. **111**: p. 053522.

[156] Khare A., et al., *Calculation of the lattice dynamics and Raman spectra of copper zinc tin chalcogenides and comparison to experiments.* Journal of Applied Physics, 2012. **111**(8): p. 083707.

[157] Minceva-Sukarova B., et al., *Raman spectra of thin solid films of some metal sulfides.* Journal of Molecular Structure, 1997. **410**: p. 267.

[158] Smith A., et al., *Raman scattering studies of SnS_2 and $SnSe_2$.* Journal of Physics C: Solid State Physics, 1977. **10**: p. 1321.

[159] Sekine T., et al., *Raman scattering and infrared reflectance in 2H-$MoSe_2$.* Journal of the Physical Society of Japan, 1980. **49**: p. 1069.

[160] Beck M. E., et al., *CuIn(Ga)Se_2-based devices via a novel absorber formation process.* Solar Energy Materials and Solar Cells, 2000. **64**: p. 135.

[161] Romeo A., et al., *Development of thin-film Cu(In,Ga)Se_2 and CdTe solar cells.* Progress in Photovoltaics: Research and Applications, 2004. **12**: p. 93.

[162] Gürel T., et al., *Characterization of vibrational and mechanical properties of quaternary compounds Cu_2ZnSnS_4 and $Cu_2ZnSnSe_4$ in kesterite and stannite structures.* Physical Review B, 2011. **84**: p. 205201.

[163] Li X. and B. Bhushan, *A review of nanoindentation continuous stiffness measurement technique and its applications.* Materials Characterization, 2002. **48**: p. 11.

[164] Hashimoto Y., et al., *Chemical bath deposition of CdS buffer layer for GIGS solar cells.* Solar Energy Materials and Solar Cells, 1998. **50**: p. 71.

[165] Nair P., et al., *Semiconductor thin films by chemical bath deposition for solar energy related applications.* Solar Energy Materials and Solar Cells, 1998. **52**: p. 313.

[166] O'Brien P. and T. Saeed, *Deposition and characterization of cadmium sulfide thin films by chemical bath deposition.* Journal of Crystal Growth, 1996. **158**: p. 497.

[167] Khallaf H., et al., *Characterization of CdS thin films grown by chemical bath deposition using four different cadmium sources.* Thin Solid Films, 2008. **516**: p. 7306.

[168] Abou-Ras D., et al., *Structural and chemical investigations of CBD-and PVD-CdS buffer layers and interfaces in Cu(In, Ga)Se_2-based thin film solar cells.* Thin Solid Films, 2005. **480**: p. 118.

[169] Jackson P., et al., *New world record efficiency for Cu(In,Ga)Se_2 thin-film solar cells beyond 20%.* Progress in Photovoltaics: Research and Applications, 2011. **19**: p. 894.

[170] Green M. A., *Solar cells: operating principles, technology, and system applications.* 1982. Prentice-Hall, Inc., (Englewood Cliffs) USA.

[171] Li J. B., et al., *Investigating the role of grain boundaries in CZTS and CZTSSe thin film solar cells with scanning probe microscopy.* Advanced Materials, 2012. **24**: p. 720.

[172] Haight R., et al., *Band alignment at the $Cu_2ZnSn(S_xSe_{1-x})_4$/CdS interface.* Applied Physics Letters, 2011. **98**: p. 253502.

Appendices

List of publication

1. X. Yin, C. Tang, L. Sun, Z. Shen and H. Gong "Study on phase formation mechanism of non- and near-stoichiometric $Cu_2ZnSn(S,Se)_4$ film prepared by selenization of Cu-Sn-Zn-S precursors" *Chemistry of Materials* **26**, 2005 (2014)

2. T. J. Huang, X. Yin, G. Qi and H. Gong "CZTS-based materials and interfaces and their effects on the performance of thin film solar cells" *Physica Status Solidi (RRL)-Rapid Research Letters* DOI: 10.1002/pssr.201409219

3. L. Zhang, C. Tang, X. Yin and H. Gong "Substrate-assisted self-organization of Ni-Cu spherical double hydroxide (SDH) and its excellent pseudo-capacitive performance" *Journal of Materials Chemistry A* **2**, 4660 (2013)

4. X. Yin, C. Tang, M. Chen, S. Adams, H. Wang and H. Gong "Hierarchical porous Cu_2ZnSnS_4 films for high-capacity reversible lithium storage applications" *Journal of Materials Chemistry A* **1**, 7927 (2013)

5. C. Tang, X. Yin, and H. Gong "Superior performance asymmetric supercapacitors based on a directly grown commercial mass 3D Co_3O_4@$Ni(OH)_2$ core−shell electrode" *ACS Applied Materials & Interfaces* **5**, 10574 (2013)

6. C. Tang, X. Yin, and H. Gong "A study on dramatically enhanced capacitance of graphene-decorated hierarchically porous nickelian heterogenite for energy storage application" *Electrochimica Acta* **114**, 543 (2013)

7. X. Yin and H. Gong “Heat-field-stimulated decomposition reaction in Cu_2ZnSnS_4” *Acta Materialia* **60**, 6732 (2012)

8. X. Yin, T. J. Huang, C. Tang, M. Du, L. Sun, Z. Shen and H. Gong “Study on the mechanical properties and interfacial structures of $Cu_2ZnSn(S,Se)_4$ films prepared from co-evaporated metallic and sulfur-contained precursors” *in process*

9. X. Yin, T. J. Huang, C. Tang, W. Yang and H. Gong “ Impacts of sulfur incorporation in precursors on the $Cu_2ZnSn(S,Se)_4$ films growth and voids formation” *in process*